

# **Influence of the Ion Energy on Generation and Properties of Thin Barrier Layers Deposited in a Microwave Plasma Process**

Von der Fakultät Mathematik und Physik der Universität Stuttgart  
zur Erlangung der Würde einer Doktorin der  
Naturwissenschaften (Dr. rer. nat) genehmigte Abhandlung

Vorgelegt von

Evelyn Christine Ramisch

aus Stuttgart

Hauptberichter: Prof. Dr. U. Stroth  
Mitberichter: Prof. Dr. T. Pfau

Tag der mündlichen Prüfung: 09.12.2011

Institut für Plasmaforschung der Universität Stuttgart

2012



Ich erkläre, dass ich die Arbeit selbständig und nur mit den angegebenen Hilfsmitteln angefertigt habe und dass alle Stellen, die dem Wortlaut oder dem Sinne nach anderen Werken entnommen sind, durch Angabe der Quellen als Entlehnung kenntlich gemacht worden sind.

Evelyn Christine Ramisch





# Kurzfassung

Nicht erst seit der von der Bundesregierung initiierten Energiewende besteht eine große Nachfrage nach umweltverträglichen Energiequellen. Dabei ist eines der Hauptaugenmerke die Entwicklung von Solarzellen mit wettbewerbsfähigen Herstellungskosten, da die Solarzellen heutzutage hauptsächlich aus kristallinem Silizium bestehen und folglich deren Produktion in Konkurrenz zur Halbleiterindustrie steht. Somit ist die Entwicklung von Solarzellen aus alternativen Materialien wie z.B. Kupfer-Indium-Gallium-Diselenid (CIGS) von großem Interesse. Da von diesem Material eine geringere Schichtdicke benötigt wird, können diese Solarzellen auf flexiblen Substraten wie auf einer Metallfolie hergestellt werden, was eine breitere Anwendung ermöglicht. In dieser Arbeit wird die Eignung von unpolierter Stahlfolie, die Kratzer im  $\mu\text{m}$ -Bereich aufweist, als Träger für die Solarzellen untersucht. Die Verwendung von Metallsubstraten erfordert eine Barriere zwischen dem Substrat und den Solarzellen, um Kurzschlüsse zwischen den einzelnen Zellen eines Solarmoduls zu vermeiden. Außerdem soll durch diese Barriere die Diffusion unerwünschter Substratbestandteile in die Solarzellen verhindert werden. Hierzu werden in dieser Arbeit Siliziumoxid- und Siliziumnitridschichten in einem Mikrowellen-Plasma-Prozess in einem Gasgemisch von HMDSO (Hexamethyldisiloxan) und Sauerstoff bzw. Monosilan und Ammoniak abgeschieden. Um das Schichtwachstum durch hochenergetische Ionen beeinflussen zu können, wird der Einfluss eines zusätzlichen Substratbias untersucht, was zu einer Überlagerung einer kapazitiven Entladung und der Mikrowellenentladung führt.

Die auf der Schichtoberfläche auftreffenden energiereichen Ionen führen zu einer Glättung und Verschmelzung der Oberfläche, besonders bei Unebenheiten auf der Substratoberfläche. Somit verbessern sich die Barriereigenschaften der Schicht deutlich, was mittels Isolationsmessungen ermittelt wurde. Die Veränderung des Schichtwachstums wird anhand von Substraten mit einer definiert rauen Oberfläche im  $\mu\text{m}$ -Bereich sowohl experimentell als auch durch Simulationen ermittelt. Die Simulationen wurden mit dem Monte-Carlo Code SDTrimSP-2D durchgeführt, der eine detaillierte Bestimmung der lokalen zum Schichtwachstum beitragenden Mechanismen analysiert. Durch die energiereichen Ionen wird zusätzlich die molekulare Zusammensetzung der Schichten beeinflusst. Diese ist für die Materialeigenschaften wie die Haftung, Härte oder das Diffusionsverhalten bedeutend. Die molekulare Zusammensetzung der abgeschiedenen Schichten wird mittels Fourier-Transformations-Infrarot-Spektren bestimmt. Aus der Schichtzusammensetzung und dem Bre-

chungsindex lassen sich Rückschlüsse auf das Diffusionsverhalten der abgeschiedenen Schichten bilden. Bei der Abscheidung mit Substratbias ergaben sich für das Siliziumoxid härtere Schichten, so dass diese im Vergleich zu ungebiasteten Siliziumoxidschichten diffusionshemmender sind. Demgegenüber verhalten sich die Siliziumnitridschichten entgegengesetzt: Diese werden mit angelegtem Substratbias poröser und somit diffusionsfördernd.

# Abstract

The demand for environment-friendly energy sources increases more and more, which is not only caused by the energy turnaround initialized by the Federal Government. In this context, the focus is set mainly on the development of wind power and solar energy with competitive production costs. Above all, this is a problem for solar cells, which, today, are mainly fabricated out of crystalline silicon and, therefore, are in competition with semiconductor industry. Hence, the development of solar cells based on alternative materials like e.g. copper-indium-gallium-diselenide (CIGS) is of great interest. Because of the lower layer thickness needed for this material, these solar cells can be fabricated on flexible substrates like metal foils. This possibility offers a broader spectrum of applications. For reaching low production costs, the applicability of unpolished steel foil, which exhibits scratches on the  $\mu\text{m}$  scale, is investigated as substrate for the solar cells in this work. The use of any metal as substrate requires a barrier layer between the substrate and the solar cells to prevent short-circuits between the separate cells of a solar module and to prevent the diffusion of undesired substrate elements into the solar cells. In this work, silicon-oxide and silicon-nitride coatings are deposited as barrier layers in a microwave-plasma process in a gas mixture of HMDSO (hexamethyldisiloxane) and oxygen or monosilane and ammonia. To have the opportunity of influencing the layer growth by high-energetic ions, an additional substrate bias is applied during the deposition, which leads to a capacitive discharge superimposing the microwave one.

The high-energetic ions impinging on the layer surface lead to a layer smoothing and melting, especially at positions of indentations in the substrate surface. Hence, the barrier properties of the coating are improved clearly, which was identified by insulation measurements of the deposited film. The layer growth modification is analyzed on the basis of substrates with a well-defined rough surface structure in the  $\mu\text{m}$  range experimentally as well as by simulations with the Monte-Carlo Code SDTrimSP-2D, which allows a detailed analysis of the local layer growth mechanisms contributing to the deposition. Additionally, the impinge of the energetic ions affects the molecular structure and composition of the coatings as well. These parameters are an important indicator for the layer material properties like adhesion, hardness and diffusion properties. The molecular composition of the deposited layers is analyzed in detail by Fourier-transform infrared (FTIR) spectroscopy. From the layer composition and their refractive index, conclusions on the diffusion behavior of the coatings are drawn. In case of applying the substrate bias, the spectra

indicate a denser and harder film in case of silicon oxide. Hence, these layers are more diffusion preventing compared to the unbiased ones. On the other hand, the silicon-nitride coatings show contrary properties: They offer more porous layers, when the substrate bias is applied, and, therefore, they assist diffusion.

# Contents

<b>1</b>	<b>Introduction</b>	<b>1</b>
<b>2</b>	<b>Theoretical background</b>	<b>5</b>
2.1	Plasma physics . . . . .	5
2.2	Surface modification . . . . .	7
2.2.1	Plasma enhanced chemical vapor deposition . . . . .	7
2.2.2	Plasma etching . . . . .	8
2.3	Plasma sheath . . . . .	9
2.3.1	Basics of the plasma sheath . . . . .	9
2.3.2	The Bohm sheath criterion and the presheath . . . . .	11
2.3.3	The high-voltage sheath . . . . .	12
2.4	Capacitive discharges . . . . .	13
2.4.1	Setup . . . . .	14
2.4.2	Dual-frequency discharges . . . . .	22
2.4.3	Low-frequency discharges . . . . .	23
2.5	Microwave discharges . . . . .	26
2.6	Various deposition processes . . . . .	28
<b>3</b>	<b>Experimental setup</b>	<b>33</b>
3.1	Coating systems . . . . .	33
3.1.1	The silicon-oxide coating . . . . .	34
3.1.2	The silicon-nitride coating . . . . .	35
3.1.3	The deposition of silicon layers . . . . .	35
3.2	Plasmodul . . . . .	37
3.2.1	The coating setup . . . . .	37
3.2.2	The Duo-Plasmaline . . . . .	41
3.2.3	The substrate bias . . . . .	42
3.3	Diagnostics . . . . .	45
3.3.1	The Fourier-transform infrared spectroscopy . . . . .	45

---

3.3.2	The photospectrometer . . . . .	47
3.3.3	Langmuir double-probe measurements . . . . .	48
3.4	Measurements of plasma parameters . . . . .	51
3.4.1	Electron density . . . . .	52
3.4.2	Electron temperature . . . . .	54
3.4.3	Conclusion . . . . .	55
<b>4</b>	<b>Barrier properties</b>	<b>57</b>
4.1	Layer-growth model . . . . .	59
4.2	Bias parameters . . . . .	61
4.3	Layer growth . . . . .	64
4.3.1	Layer growth on model substrates . . . . .	64
4.3.2	Layer growth on steel . . . . .	67
4.4	Insulation measurements . . . . .	68
4.4.1	SiO <sub>x</sub> coatings . . . . .	69
4.4.2	SiN <sub>y</sub> coatings . . . . .	70
4.5	Conclusion . . . . .	71
<b>5</b>	<b>Simulations</b>	<b>73</b>
5.1	The Monte-Carlo simulation code . . . . .	74
5.1.1	SDTrimSP . . . . .	74
5.1.2	SDTrimSP-2D . . . . .	76
5.2	Input parameters . . . . .	78
5.3	Comparison experiment – simulation . . . . .	80
5.4	Film-forming processes . . . . .	83
5.5	Conclusion . . . . .	87
<b>6</b>	<b>Molecular composition</b>	<b>89</b>
6.1	Fourier-transform infrared spectra . . . . .	89
6.1.1	Silicon oxide . . . . .	90
6.1.2	Silicon nitride . . . . .	97
6.2	Refractive index . . . . .	103
6.3	Conclusion . . . . .	105
<b>7</b>	<b>Summary and conclusions</b>	<b>107</b>
	<b>Literature</b>	<b>111</b>
	<b>Acknowledgment</b>	<b>125</b>

# Chapter 1

## Introduction

In the last decade, the public and world wide political discussion about energy has become as intense as never before, since the demand for energy in, especially the aspiring countries, increases strongly. The call for environmentally friendly energy sources is growing louder. The focus is set mainly on renewable energy sources without resource exhaustion like geothermal energy, wind power and solar energy. For a broad acceptance, the power generation with renewable energies has to offer competitive production costs. Above all, this is a problem for solar cells. Today, common solar cells are fabricated out of crystalline silicon, which offers an indirect band gap and, therefore, unefficient absorption characteristics. This manufacturing sector is in competition with the semiconductor industry, which needs high-purity silicon, too. Hence, the development of solar cells based on alternative materials is of great interest. One key issue is the minimization of material costs through a low consumption of raw material. Thus, research in this field concentrates on thin-film solar cells consisting of materials, which offer a direct band gap. Examples are amorphous silicon (a-Si), cadmium-tellurium (CdTe) or copper-indium-gallium-diselenide (CIGS). Moreover, these cells have the advantage to be producible on flexible substrates like metal or polymer foils in contrast to the well-established glass substrates. With a higher flexibility, lower weight and finally lower production costs, these cells offer a broader spectrum of applications. For these flexible substrates, however, a barrier-layer between the substrate and the solar cells is required. The present work focusses on the optimization of the barrier layer production for CIGS solar cells [1, 2], which offer an actual record efficiency of 20.3% [3]. In parts, this work is carried out in the framework of the publicly funded BMBF project "FlexNet" (functional coatings for flexible, low-cost CIGS thin-film solar cells) in collaboration with the ZSW – Center for Solar Energy and Hydrogen Research Baden-Württemberg – and the StEM – Stuttgart Center for Electron Microscopy, Max Planck Institute for Metals Research, Stuttgart.

The diffusion of undesired substrate elements into the CIGS material, which can reduce the efficiency of the solar cell, and a short-circuit between the separate cells of a solar module has to be avoided. Thus, the barrier layer has to fulfill the following

requirements: It has to be diffusion preventing, and – in case of metal substrates – it has to be insulating. Because of the high temperature needed during the CIGS process (up to 650 °C), metal foils have a great advantage compared to substrates consisting of polymers. Within this work, the properties of the barrier films and the possibilities of improving them is investigated on unpolished steel foil.

As barrier films, silicon oxide ( $\text{SiO}_x$ ) or silicon nitride ( $\text{SiN}_y$ ) is deposited in a microwave-PECVD (**p**lasma **e**nhanced **c**hemical **v**apor **d**eposition) process in a gas mixture of HMDSO (**h**examethyl**d**isiloxane) and oxygen or monosilane and ammonia. The PECVD process is widely-used and powerful to modify material surfaces or deposit thin films in industrial processes. The presented depositions are carried out in the modular plasma device called Plasmodul [4]. On the one hand, the advantage of microwave plasmas is their high density, which leads to a high deposition rate and therewith to a high productivity. On the other hand, the plasma sheath of such a plasma is too small to cause a directed ion acceleration for surface modifications. The impinge of high-energetic ions has an additional effect on the layer growth and plays an important role in the following context:

The surface of the used metal foils is not polished. Hence, it exhibits scratches, flakes, and isolated inclusions on the  $\mu\text{m}$  scale. It is well known, that such a substrate-surface structure is replicated on the surface of the deposited coating in a microwave-PECVD process [5, 6]. Hence, a homogeneous smooth coating cannot be obtained and voids are developed in the deposited film at positions of notches on the substrate surface [7, 8], whereby the barrier properties of the coating are lost. The impact of high-energetic ions can smooth out these irregularities. To have the opportunity of affecting the layer growth by an ion bombardment, an "artificial" plasma sheath is generated by applying a substrate bias. Because of the deposition of insulating layers, the bias voltage has to be alternating. Hence, the microwave plasma is superimposed by a capacitive discharge. This leads to an independent control of the particle flux on the substrate – determined by the microwave plasma – and the energy of impinging ions – determined by the plasma sheath.

The influence of the high-energetic ions on the layer growth at positions of notches in the substrate surface is analyzed on the basis of substrates with a well-defined rough surface structure. Due to the high application of energy, the replication of the substrate surface on the film surface is avoided. The resulting improved barrier properties are verified by insulation measurements of the coatings. To analyze the modification – induced by the ion bombardment – of the layer-growth mechanisms in detail, the layer growth is simulated with the Monte-Carlo code SDTrimSP-2D [9]. This code also includes the effect of the impacting energetic ions, in contrast to former works, which deal only with thermal impinging particles [10, 11, 12]. The modification of the layer growth influences not only the profile of the coatings, but also their molecular structure and composition, which determines mainly the material properties like adhesion, hardness or diffusion properties. Hence, the detailed knowledge of the influence of the ion bombardment on the chemical composition is essential for the understanding of the manipulation of



the layer growth. For the analyses of the molecular composition and structure of the films, Fourier-transform infrared (FTIR) spectroscopy is used.

The aim of this work is the optimization of barrier coatings, which are suitable for the production of CIGS solar cells on the steel substrate, and – going along with this – a comprehensive understanding of the effects of the impinge of high-energetic ions on the layer surface during the deposition. This thesis is organized as follows: The theoretical background of this work is given in the following chapter 2. The theory is mainly dedicated to the plasma sheath and their generation in different plasma discharges. Chapter 3 introduces the investigated coating systems silicon oxide and silicon nitride, the used experimental setup – the Plasmodul – and the utilized diagnostics, by which the plasma in the Plasmodul and the deposited coatings are characterized, respectively. The influence of the ion bombardment on the layer growth is investigated in chapter 4. Subsequently, the effect of the manipulated layer growth on the barrier properties of these coatings is determined by resistance measurements. Detailed analyses of the effect of impinging high-energetic ions on the growing layer are carried out in chapter 5 on the basis of Monte-Carlo simulations with the code SDTrimSP-2D [9]. The influence of the high application of energy on the molecular structure of the deposited films is analyzed in chapter 6 by FTIR spectroscopy. At the end, a summary concludes this work in chapter 7.



# Chapter 2

## Theoretical background

In this chapter, the basic principles of plasma physics are summarized in section 2.1, mainly in terms of the properties of deposition processes to control the layer growth, for which the plasma sheath plays an essential role. Subsequently, two methods of surface modification in a plasma process are introduced in section 2.2: the plasma enhanced chemical vapor deposition (PECVD) and the etching process. Section 2.3 is dedicated to the physics of the plasma sheath. Finally, two main processes, which are used to generate plasmas for technical use, are described with regard to their heating mechanism sustaining the discharge and their effect on the plasma parameters. Both, the advantages as well as the disadvantages of the capacitively coupled discharges (section 2.4) and microwave discharges (section 2.5) are discussed. In this work, both techniques are combined for a new deposition process, which is described in section 2.6.

### 2.1 Basic principles of plasma physics

In a plasma, the sum of free negative and positive charges must be zero. This is called the quasi neutrality. The electric field of a charged particle brought into a plasma is shielded by the surrounding particles. As a consequence, the potential drops exponentially, and not as  $1/r$  as for the Coulomb potential, on the Debye  $1/e$ -decay length [13]

$$\lambda_d = \sqrt{\frac{\epsilon_0 T_e}{e^2 n_e}}. \quad (2.1)$$

$\epsilon_0$  is the permittivity of vacuum,  $T_e$  the electron temperature,  $e$  the elementary charge and  $n_e$  the electron density. A plasma with a higher density and/or a lower temperature shields charged particles more effectively. The condition for a plasma is that the number of particles participates in the shielding, i.e. the number of particles  $N_D$  in the Debye sphere, must be

$$N_D = \frac{4}{3}\pi\lambda_D^3 n_e \gg 1, \quad (2.2)$$

and, of course, the plasma dimension must be  $L \gg \lambda_D$ . This means, that the relative change in density needed to shield an external charge  $q_0$

$$\frac{\delta n}{n} = \frac{q_0/e}{N_D} \quad (2.3)$$

is negligible and, hence,  $n_e \approx Z_i n_i$  with the ion charge number  $Z_i$ . Most plasmas are ideal, which means that the potential energy can be neglected against the kinetic energy of the particles.

The electrons and ions respond to alternating electric fields in the plasma with an oscillation. This is a collective phenomenon. The oscillation frequency is called plasma frequency. It results from the one-dimensional Poisson equation to

$$\omega_{\text{pe},i} = \sqrt{\frac{n_{e,i} e^2}{\epsilon_0 m_{e,i}}} \quad (2.4)$$

with the electron mass  $m_e$ , the ion mass  $m_i$  and the ion density  $n_i$ . Due to the mass difference of the electrons and ions, the ion-plasma frequency  $\omega_{\text{pi}}$  is smaller than the electron-plasma frequency  $\omega_{\text{pe}}$  by a factor of  $\sqrt{m_e/(Zm_i)}$ . Thus, the electrons determine the upper limit of electric field oscillation frequencies, which are effectively shielded, and therefore, the electron-plasma frequency is commonly called plasma frequency. Hence, electromagnetic waves with a frequency lower than the plasma frequency cannot penetrate the plasma, whereas the ones with a frequency higher than the plasma frequency can traverse the plasma volume. This subject plays an essential role in the different kinds of generating a plasma, which are illustrated in section 2.4, 2.5 and 2.6.

For defining the temperature of a plasma, it must be distinguished between electron, ion and gas temperature. In contrast to high-density plasmas, in the present applications the three temperatures cannot be considered as equal. Hence, we have a non-equilibrium plasma. The ion and gas temperature is considered as thermal and is roughly approximated to  $T_i = T_g \ll T_e$ , i.e. neglected compared to the electron temperature  $T_e$ . This is justifiable because of the excitation of charged particles in a plasma: The generation and heating of the plasma is realized by accelerating the electrons due to their lower inertia compared to the ions and neutrals. The electrons collide with the other particles in the plasma. If their kinetic energy is higher than the ionization energy of the collision particles, these can be ionized according to the ionization-cross section. The electron velocity distribution function in such a plasma is regarded as Maxwellian:

$$f_M = \left( \frac{m_e}{2\pi T_e} \right)^{3/2} \exp \left\{ -\frac{m_e v_e^2}{2T_e} \right\} \quad (2.5)$$

with the electron velocity  $v_e$ . The electron temperature and the mean electron

velocity  $\bar{v}_e$  are linked through:

$$\bar{v}_e = \sqrt{\frac{8T_e}{\pi m_e}}. \quad (2.6)$$

In an equilibrium plasma, the ion density and the density of the neutrals are linked by the Saha equation [13]:

$$\frac{n_i}{n_n} = 3 \times 10^{27} \frac{T^{3/2}}{n_i} \exp \left\{ -\frac{W_{\text{ion}}}{T} \right\}, \quad (2.7)$$

where  $n_n$  is the density of the neutrals,  $W_{\text{ion}}$  is the ionization energy of the atoms and  $T$  the gas temperature in eV. Equation (2.7) has the form of a law of mass action.

## 2.2 Surface modification in a plasma process

Plasma-assisted surface modification is a widely used method in industry. Many different types of processes are embraced by this method. Thin-film deposition is achieved by a PECVD process or a sputtering process [14]. A related task of a surface-modifying plasma is ion implantation on the substrate surface. Plasma etching is a key process for removing material from surfaces. By plasma functionalization, material surfaces are activated (free radicals are generated) to improve the adhesion properties of the material. This is mostly done in an oxygen plasma and in the case of polymer surfaces.

All processes describing the surface modification in a plasma process are plasma-wall interactions. The specific plasma processes describing each surface modification are taking place in the plasma-sheath region, which will be described in section 2.3. In the following, the PECVD process and the plasma etching will be introduced.

### 2.2.1 Plasma enhanced chemical vapor deposition

PECVD is a common method for depositing thin films in the nm up to the  $\mu\text{m}$  range. In contrast to a conventional CVD (chemical vapor deposition) process, where a solid component is deposited on a strongly heated substrate due to chemical reactions from the gas phase, PECVD processes have the advantage to work at low substrate temperatures. This is possible through the generation of the reactive components like ions, electrons and radicals within the plasma. The radicals, which are deposited on an inserted substrate, are created inside the plasma. Thus, temperature-sensitive materials, e.g. foils, can be coated in such a process because of the non-equilibrium properties of the plasma (i.e.  $T_i \ll T_e$ , section 2.1). The ions impinging on the substrate have low energy and, therefore, cannot damage the substrate despite their high mass. The only high-energetic particles are the electrons, which also cannot damage the substrate because of their low mass. Hence,

films for which high temperatures are needed in the CVD process, can be deposited at low substrate temperatures. As in the CVD process, the surface reactions in a plasma-enhanced process are mainly controlled by parameters like the gas composition, pressure (above all the partial pressure of the single gases, which controls the concentration of the reactive species) as well as the substrate temperature. They are determined empirically for each demand on the deposited film. In combination with an ion bombardment from the plasma (see section 2.6), these parameters determine the film properties like the molecular composition, stress and morphology.

In contrast to the conventional CVD process, however, PECVD processes cannot be utilized in every industrial application. Layers fabricated in a plasma device have an amorphous character, whereas the high substrate temperature and the clearly reduced deposition rate in a CVD application causes a rather crystalline layer growth. Thus, the CVD process can be a choice for the deposition on temperature-resistant materials like e.g. metals or glass.

PECVD processes are usually classified into two methods: The direct deposition process and the remote plasma process. In a remote device, the substrate has no direct contact to the plasma and therefore a damage of possible impinging ions is reduced, but the layer forming radicals, which usually have a longer lifetime than the reactive ions, can still reach the substrate. The disadvantage of such a setup is a reduced deposition rate and, thus, higher production costs in manufacturing devices.

In terms of the plasma generation, many different types of plasma deposition devices are existent. In the sections 2.4 and 2.5, the most common plasma discharges used for industrial application are introduced and compared in section 2.6. In this work, a remote PECVD process is used, which is described in detail in section 3.2. The specific coating-forming gas systems are introduced in section 3.1.

### 2.2.2 Plasma etching

In contrast to a plasma-deposition process, in an etching process, the plasma is used as a tool for removing material from a surface. There are two different main etching processes, which can be combined to yield a more distinct effect. A species selective but isotropic etching can be achieved by pure chemical etching, i.e. the plasma discharge supplies gas-phase caustic atoms or molecules. They react chemically with the surface components and form gaseous particles. This produces a volatile reaction product compound, which can leave the surface.

A method of removing nonvolatile products from a surface is sputtering. This is a well-directed process. Hence, a strong anisotropic etching can be achieved by this method. In a sputter process, atoms are ejected from a surface by strong ion bombardment. If the energy transfer of the impinging particles to the target atoms is greater than the surface-binding energy of the target material, the target particles can leave the solid. This process is called sputtering. Because of the approximate equality of the surface-binding energy of different materials, this represents a

non-selective method, but it can strongly depend on the angle of incidence of the impinging ions [15]. Compared to chemical etching, it offers a low etching rate, because the yield is of the order of one atom per incident ion. The combination of both etching processes leads to a mostly anisotropic etching with a yield, which is comparable to that of the pure chemical etching. This is called the ion-energy driven etching.

## 2.3 The plasma sheath

The plasma sheath plays an essential role for technologically used plasmas. Through the sheath the energy of the impinging ions can be controlled. This is discussed in section 2.5 and 2.6. In this section, the formation and the basic principles of the plasma sheath will be introduced.

### 2.3.1 Basics of the plasma sheath

The first time the plasma was subdivided into a bulk and a sheath region was 1928 by Langmuir [16]. In the following, the fluid approach of the stationary plasma sheath is given. This model is fully legitimated in the case of high-voltage sheaths [17]. The assumptions are independent of the specific plasma parameters in the bulk. The common theoretical description of stationary boundary plasma sheaths is based on Tonks, Langmuir and Bohm [18, 19].

By inserting an absorbing electrode into the plasma (Fig. 2.1a), it is charged negatively with respect to the surrounding plasma due to the higher mobility of the electrons compared to the ions. This is the usual situation in an electropositive plasma, which means only positive charged ions are existent and which is the assumption for all further considerations. The potential of the electrode is called the floating potential

$$\Phi_{fl} = -\frac{T_e}{2e} \ln \sqrt{\frac{m_i}{2\pi m_e}} + \Phi_p \quad (2.8)$$

with the plasma potential  $\Phi_p$ . The consequence of this potential is a repulsion of most of impinging electrons, namely those with an energy lower than  $e\Phi_{fl}$  (Fig. 2.1b). This leads to a strong decrease of the electron density in front of the electrode. Therefore, a positively charged region of a few Debye lengths is formed in front of the electrode (Fig. 2.1c). The position of zero potential is defined as the edge between the bulk and the sheath of the plasma. The ions are accelerated by the negative potential of the electrode. Hence, the ion density shows a slight decrease due to the flux continuity  $n_i(x)u_i(x) = \text{const}$ . The density and the potential characteristics in front of the electrode or the wall constituting the edge of a bounded plasma are depicted in Fig. 2.1.

The following considerations are valid under the assumption of a collisionless sheath, Maxwellian electrons with a temperature  $T_e$ , cold ions ( $T_i \approx 0$ ) and equal

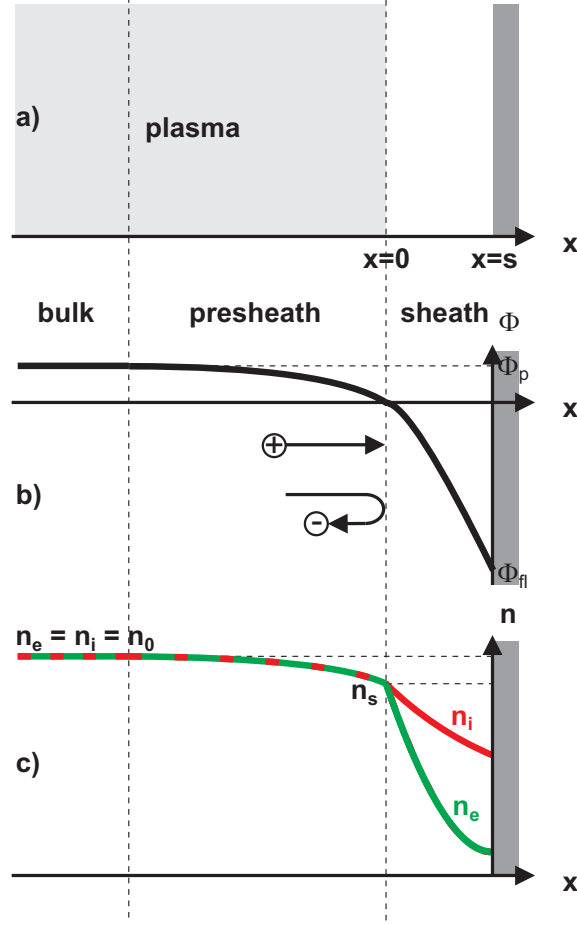


**Fig. 2.1:** a) Shielding of the negatively charged wall against the plasma. b) Potential characteristics in front of the boundary of a plasma. The ions are accelerated by the negative wall potential, the electrons are repelled. c) Electron- and ion-density characteristics in front of an electrode.

densities of electrons and ions at the interface between the plasma and the sheath,  $n_e(0) = n_i(0) = n_s$ , where  $x = 0$  is defined as the position of the plasma-sheath transition, and ideally conducting walls.

Defining  $u_s$  as the ion velocity at entry into the sheath, the sheath is described by the following four equations:

$$\frac{1}{2}m_i u^2(x) = \frac{1}{2}m_i u_s^2 - e\Phi(x) \quad \text{ion-energy conservation} \quad (2.9)$$

$$n_i(x)u_i(x) = n_s u_s \quad \text{ion-flux conservation} \quad (2.10)$$

$$n_e(x) = n_s \exp\left\{\frac{e\Phi(x)}{T_e}\right\} \quad \text{electron Boltzmann distribution} \quad (2.11)$$

$$\frac{d^2\Phi(x)}{dx^2} = \frac{e}{\epsilon_0} (n_e(x) - n_i(x)) \quad \text{Poisson equation} \quad (2.12)$$



The Poisson equation gives the sheath potential  $\Phi(x)$  in dependence of the position. To solve this equation, the ion density has to be determined from a combination of Eqs. (2.9) and (2.10):

$$n_i(x) = n_s \left( 1 - \frac{2e\Phi(x)}{m_i u_s^2} \right)^{1/2}. \quad (2.13)$$

Therewith, the Poisson equation is given by

$$\frac{d^2\Phi}{dx^2} = \frac{en_s}{\epsilon_0} \left[ \exp\left\{ \frac{e\Phi(x)}{T_e} \right\} - \left( 1 - \frac{e\Phi(x)}{\frac{1}{2}m_i u_i^2(x)} \right)^{-1/2} \right]. \quad (2.14)$$

### 2.3.2 The Bohm sheath criterion and the presheath

By solving Eq. (2.14) for the sheath potential, stable solutions can only be obtained for sufficiently large ion velocities  $u_s$  at the plasma-sheath edge. Because of its non-linearity, an accurate solution of this equation can only be determined numerically. But an approximation with the boundary conditions of a field-free plasma,  $\Phi(0) = 0$  and  $d\Phi/dx = 0$ , yields the condition:

$$u_s \geq u_B = \sqrt{\frac{T_e}{m_i}}. \quad (2.15)$$

Hence, the entrance velocity of the ions to the plasma sheath must not be lower than the so called Bohm velocity  $u_B$ . Otherwise, no shielding of the wall from the plasma is possible. This condition is known as the Bohm sheath criterion [20].

With the condition of cold ions ( $T_i = 0$ , consequently  $u_i \ll u_B$ ), the Bohm sheath criterion leads to the necessity of a directed acceleration of the ions right into the in principle field-free plasma region by an electric field. The region of this (very small) electric field is called presheath, which is located in front of the plasma sheath and much more extended than that region. In contrast to the sheath, the presheath is part of the plasma region by definition, because the quasi neutrality is guaranteed in it. Both, the electron as well as the ion density decrease in the same way over the expansion of the presheath, namely according to

$$n_s = n_0 \exp\left\{ \frac{-e\Phi_p}{T_e} \right\} \approx 0.61n_0. \quad (2.16)$$

At the Bohm velocity, the momentum balance shows a singularity. This indicates the transition between the plasma scaled presheath and the Debye scaled plasma sheath [21]. The behavior of the densities and the potential in the presheath is depicted in Figs. 2.1b,c.

If the plasma sheath is not collisionless, a unique Bohm velocity cannot be determined and as a consequence, the plasma region and the sheath cannot be exactly separated. A detailed essay of this subject can be found in Ref. [21].

### 2.3.3 The high-voltage sheath

It is possible to extend the plasma-sheath region in front of an electrode by applying a negative voltage to it. The consequence is an intense potential decay in the sheath region, and, hence, the ion bombardment of the electrode can be regulated by the applied voltage. For the case of high-voltage sheaths, two models are common: the matrix sheath and the Child law sheath.

#### The matrix sheath

The matrix sheath model [15] is the more simple one. The precondition is a uniform ion density in the complete sheath region ( $n_i(x) = n_s$ ). For the electrons,  $n_e = n_s \exp\{\Phi(x)/T_e\} \rightarrow 0$  is valid, because almost all electrons are repelled by the strong negative potential of the plasma sheath. Hence, only ions are present in the sheath region. This simplification leads to an easy calculation of the sheath thickness  $s$  by using the Poisson equation

$$\frac{d^2\Phi(x)}{dx^2} = \frac{en_s}{\epsilon_0}, \quad (2.17)$$

and taking the boundary condition  $\Phi(s) = -U_0$  into account. Thus, the sheath thickness can be calculated to

$$s = \sqrt{\frac{2\epsilon_0 U_0}{en_s}} = \lambda_{D,s} \sqrt{\frac{2eU_0}{T_e}} \quad (2.18)$$

with the Debye length  $\lambda_{D,s} = \sqrt{\epsilon_0 T_e / (e^2 n_s)}$  at the sheath edge. Hence, the thickness of the plasma sheath can be a multiple of the Debye length, depending on the applied voltage  $U_0$ .

#### The Child law sheath

The Child law sheath model [15] includes a smooth decay of the ion density from the plasma-sheath edge to the electrode taking the ion acceleration in the sheath region into account. Hence, it is the more realistic model. The ion density as a function of position is obtained from Eq. (2.13) using the simplification  $1/2m_i u_s^2 \ll e\Phi(x)$ :

$$n_i(x) = \frac{I_{i0}}{e} \left( -\frac{2e\Phi(x)}{m_i} \right)^{-1/2}. \quad (2.19)$$

The sheath thickness can be calculated in the same way as in the matrix sheath model by including the constant ion current  $I_{i0} = en_s u_B$ . This results in

$$s = \frac{\sqrt{2}}{3} \sqrt{\frac{\epsilon_0 T_e}{e^2 n_s}} \left( \frac{2eU_0}{T_e} \right)^{3/4} = \frac{\sqrt{2}}{3} \lambda_{D,s} \left( \frac{2eU_0}{T_e} \right)^{3/4}. \quad (2.20)$$

Hence, the sheath thickness derived from this model is by a factor  $(eU_0/T_e)^{1/4}$  larger than the one from the matrix sheath model.

The position-dependent potential inside the sheath region is obtained from the Poisson equation [15]:

$$\Phi(x) = -U_0 \left(\frac{x}{s}\right)^{4/3}. \quad (2.21)$$

By inserting Eq. (2.21) into the energy conservation (Eq. (2.9)), a condition for the ion-transit time through the sheath region is obtained:

$$\frac{dx}{dt} = \underbrace{\sqrt{\frac{2eU_0}{m_i}}}_{v_0} \left(\frac{x}{s}\right)^{2/3}. \quad (2.22)$$

By integrating Eq. (2.22) and setting  $x = s$ , the ion-transit time is obtained:

$$\tau_i = \frac{3s}{v_0}. \quad (2.23)$$

In summary, the model of the plasma sheath considered in this work is based on the fluid description. It is universal, because of the validity of the Bohm criterion: All ions enter the sheath region with nearly the same velocity, namely the Bohm velocity  $u_B$ . Hence, the description of the plasma sheath is only dependent on the electron temperature and the ion mass and, therefore, independent of the remaining properties of the corresponding presheath.

In a different approach like the kinetic analysis, the CX model or the Tonks-Langmuir model [17], the detailed processes in the presheath become important to determine the distribution function of the ions entering the sheath. But these models differ markedly only in the case of low-voltage sheaths, where the ion velocity at the sheath edge plays an essential role for their impinging velocity at the electrode. If the acceleration of the ions in the sheath region due to a high-potential drop is much higher than the initial velocity of the ions entering the sheath, the difference of the initial ion velocities can be neglected. A comparison of the different models can be found in Ref. [17].

## 2.4 Capacitive discharges

Capacitive discharges are widely used to generate technological plasmas for low-pressure and low-temperature deposition processes. These discharges offer a well-extended high-voltage capacitive plasma sheath of a few mm up to the range of 1 cm in front of an inserted electrode. Hence, the growth mechanisms of the deposited coatings are mainly influenced by ion bombardment. Therefore, these discharges are not suited for coating sensitive substrates like e.g. foils.

### 2.4.1 Setup

A capacitive discharge is driven by applying an alternating voltage or current on two electrodes immersed in the plasma. In industry, the typical excitation frequency of these discharges is  $\omega = 13.56$  MHz, thus they are high-frequency discharges. The most commonly used setup is a voltage applied to one electrode with the other electrode grounded. This leads to a modulated plasma potential  $\Phi_p$ . The rf current flows across the plasma sheath generated in front of the electrode and the plasma bulk, leading to stochastic and ohmic heating. These are the main heating mechanisms, which sustain a capacitive discharge.

The description of capacitive discharges is simplified mainly by separating the discharge into the sheath and the bulk region. Hence, the discharge can be described by the equivalent circuit diagram shown in Fig. 2.2. The two sheaths, indicated by the index a and b, can be represented as an ohmic resistance  $R$ , which is connected in series with a parallel circuit of a capacitance  $C$  and a diode  $D$ . The bulk plasma, described as a parallel circuit of a capacitance and a series of an ohmic resistance and an inductance  $L$  with the index p, is connected in series with the two sheaths [22].

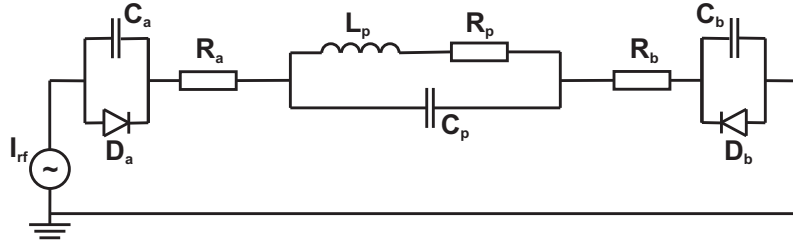


**Fig. 2.2:** Equivalent circuit diagram of a capacitive discharge with the two plasma sheaths a and b and the plasma bulk indicated by the index p.

A complete self-consistent model of capacitive discharges is complicated. However, with a few simplifications these discharges can be described analytically. This will be done in the following sections. First, the properties of high-frequency symmetric discharges are described. The condition for high-frequency discharges is that their excitation frequency is higher than the ion-plasma frequency,  $\omega > \omega_{pi}$ . Then the ions respond only to the time-averaged electric field. As a common application for coating processes in industry, dual-frequency discharges are presented in section 2.4.2, too. In contrast to high-frequency discharges, low-frequency discharges are introduced in section 2.4.3. Here, the physical properties of the discharge change and a different model has to be used.

### High-frequency symmetric discharges

A schematic view of a symmetric capacitive discharge is depicted in Fig. 2.3a. Both electrode areas are equal,  $A_a = A_b = A$ . The discharge-driving current is chosen to be sinusoidal,

$$I(t) = I_{rf} \sin(\omega t). \quad (2.24)$$

The amplitude, the angular frequency  $\omega$ , the neutral gas pressure  $n_g$  and the distance between the electrodes  $l$ , which is very small compared to the electrode areas, are the chosen control parameters. Certainly, a capacitive discharge can be driven with any kind of alternating voltage, the solution of the specific equations in each case is comparable to that presented here.

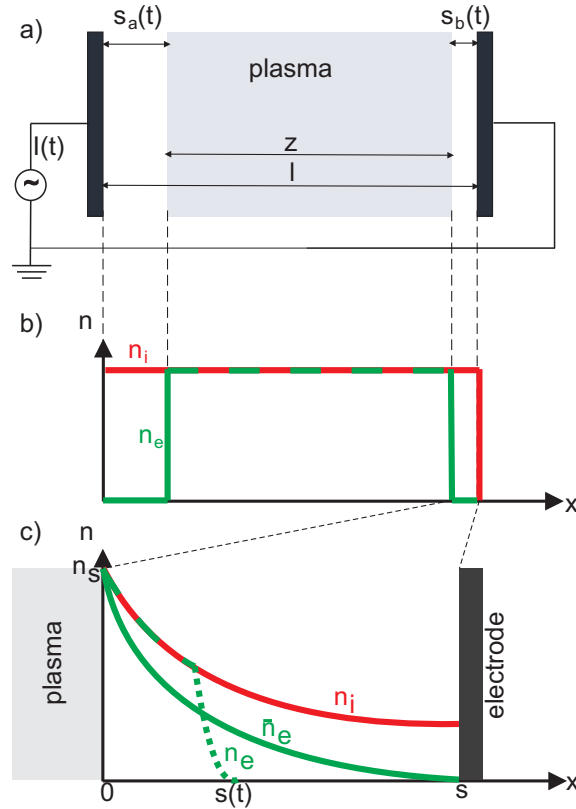


**Fig. 2.3:** a) Schematic of a typical symmetric capacitive discharge, driven by a sinusoidal current. b) Electron- and ion-density characteristics in the range of the whole discharge (bulk and sheaths) of the homogeneous capacitive discharge model. c) Electron- and ion-density characteristics in the plasma-sheath region of the inhomogeneous model.

With the given control parameters, the discharge parameters like the electron density  $n_e$ , the electron temperature  $T_e$ , the voltage drop  $U(t)$  over the discharge and the dissipated power  $S$  can be calculated by the homogeneous model. It bases on several simplifications:

- The applied frequency  $\omega$  is higher than the ion-plasma frequency. Hence, the ions can only respond to the time-averaged potential and can be regarded as an inflexible background gas.
- The electron-plasma frequency is clearly higher than the current-driving frequency. Therefore, the electrons respond to the instantaneously developing electric field and oscillate between the two electrodes against the ion background.
- No transverse electromagnetic propagation is allowed. This can be legitimated by  $l \ll \sqrt{A}$ . Consequently, the equations are reduced to one dimension.
- In the sheath region,  $n_e = 0$  is assumed.
- The ion density in the sheath region is assumed to be constant:  $n_i = n_s = \text{const}$  (see Fig. 2.3b).

Hence, the homogeneous model acts on the condition of a Matrix sheath (section 2.3.3). It is a very basic model, because it does not include a self-consistent solution of the nonlinear electron and ion dynamics. A more precise description of the plasma-sheath parameters are obtained by the inhomogeneous model, which takes the acceleration of the ions during the transition of the sheath region into account and is established in the Child law sheath theory (section 2.3.3). Therefore, the ion density decreases from the bulk to the electrode. As a consequence, the space charge of oscillating electrons is also modified by including the dynamics of the sheath edge (see Fig. 2.3c). Thus, it is the more realistic model.

The following analyses of the high-frequency discharges are based on the homogeneous model, because it gives considerable insight into the behavior of the capacitive discharges by comparatively simple descriptions.

### The voltage characteristics

The voltage across the plasma bulk is determined by the applied current  $I(t)$  and the resistance of the bulk, which is calculated under consideration of the equivalent circuit of the discharge,

$$Z_{\text{bulk}} = \left( \frac{1}{R_p + i\omega L_p + \frac{1}{i\omega C_p}} \right)^{-1} \quad (2.25)$$

with the ohmic resistance  $R_p$ , the inductance  $L_p$  and the capacitance  $C_p$  of the plasma bulk. Hence, the voltage can be written as

$$U_{\text{bulk}}(t) = Z_{\text{bulk}} \cdot I(t) = Z_{\text{bulk}} \cdot I_{\text{rf}} \sin(\omega t), \quad (2.26)$$

the response to the applied current is linear without any generation of a dc component (self bias).

The voltage, which drops from the plasma to the electrode in the sheath region, is equal at both sheaths except for a phase shift of  $\pi$ . Furthermore, a distinction between the voltage based on the displacement current and the one based on the (clearly lower) conduction current is needed for the calculation of the sheath voltage. The displacement current flowing through sheath "a" (Fig. 2.3a) is  $I_a(t) = \epsilon_0 A (\partial E / \partial t)$ . With the Poisson equation and the boundary condition of a continuous electric field at the bulk-sheath interface, this results in

$$I_a(t) = -en_s A \frac{ds_a}{dt}. \quad (2.27)$$

The solution of this equation is

$$s_a(t) = \bar{s} - s_{\text{rf}} \sin(\omega t). \quad (2.28)$$

The sheath boundary oscillates sinusoidally with an amplitude  $s_{\text{rf}} = I_{\text{rf}} / (en_s \omega A)$  around the dc value  $\bar{s}$ . Therefore, it is obvious that the sheath-boundary oscillation is a linear response to the applied current. From this, the voltage across sheath "a" is given by [15]

$$U_a(t) = \int_0^{s_a} E dx = -\frac{en_s}{2\epsilon_0} \left( \bar{s}^2 + \frac{1}{2} s_{\text{rf}}^2 - 2\bar{s} s_{\text{rf}} \sin(\omega t) - \frac{1}{2} s_{\text{rf}}^2 \cos(2\omega t) \right). \quad (2.29)$$

An equivalent calculation taking into account the continuity of current  $I_b(t) = -I_a(t)$  leads to the voltage across sheath "b". The result is a highly nonlinear voltage response across one plasma sheath [22] and, accordingly, hysteresis effects [23]. The combination of both nonlinear sheath voltages  $U_a(t)$  and  $U_b(t)$  and the voltage across the bulk  $U_{\text{bulk}}(t)$  results in a linear response of the total voltage drop over the whole discharge:

$$U(t) = \left( \underbrace{\frac{2en_s \bar{s} s_{\text{rf}}}{\epsilon_0}}_{U_{\text{ab}}} + \underbrace{I_{\text{rf}} \cdot Z_{\text{bulk}}}_{U_{\text{bulk}}} \right) \sin(\omega t). \quad (2.30)$$

In general, almost all of the voltage drops across the sheath regions. Hence, the assumption of  $|U_{\text{bulk}}| \ll |U_{\text{ab}}|$  is valid. This leads to the simplification, that the sheath is purely capacitive and the bulk purely ohmic.

The total capacitance of both sheaths can be obtained by differentiation and only taking the sheath voltage  $U_{\text{ab}}$  in Eq. (2.30) into account:

$$C_{\text{ab}} = \frac{\epsilon_0 A}{2\bar{s}}. \quad (2.31)$$

### Heating mechanisms

Capacitive discharges are sustained by two main heating mechanisms: the ohmic and the stochastic heating. The third one presented here is the nonlinear series resonance heating, which is a result of the nonlinearity of the plasma sheath edge motion resulting from the inhomogeneous model. Due to this oscillation, this heating mechanism is a result of a modified ohmic heating.

**Ohmic heating:** Generally, the main current in the bulk of the discharge is the electron-conduction current because of the nearly pure ohmic character of the plasma bulk. Consequently, the main heating mechanism in this region is ohmic heating. The electrons are accelerated by the externally applied electric field in one direction in space (thus they oscillate with the driving frequency), until they collide inelastically with particles of the immobile background gas (ions and neutrals). By colliding, the direction of their velocity is changed, but not the absolute value. This leads to a Maxwell distributed electron velocity, from which the thermal velocity and therefore the electron temperature

$$T_e = \frac{v_{\text{th}}^2 m_e^2}{4} \quad (2.32)$$

can be derived. An ionization process of the neutrals by the colliding electrons is unlikely, because of the comparatively low mean electron energy, which does not reach the ionization threshold. The time-averaged power deposited in the plasma bulk is given by [15]

$$\bar{S}_{\text{ohm}} = \frac{1}{2} \left( \frac{I_{\text{rf}}}{A} \right)^2 \frac{m_e \nu_m z}{e^2 n_s}, \quad (2.33)$$

with the electron-neutral collision frequency  $\nu_m$  and the extension  $z$  of the plasma bulk (see Fig. 2.3a).

**Stochastic heating:** Due to the non-existing or low electron density, the heating mechanism in the plasma sheaths is due to the reflection of the electrons at the plasma-sheath edge, which can be considered as an elastic collision with a wall. Moreover, the velocity of the plasma-sheath edge, resulting from its oscillation, has to be taken into account. Hence, the velocity of the reflected electrons  $u_r$  can be expressed by

$$u_r = -u + 2u_s. \quad (2.34)$$

$u$  is the velocity of the impinging electrons and  $u_s$  the one of the sheath edge. The resulting dissipated power – by taking the Maxwellian electron velocity distribution into account – is

$$\bar{S}_{\text{stoc}} = \frac{1}{2} \frac{m_e \bar{v}_e}{e^2 n_s} \left( \frac{I_{\text{rf}}}{A} \right)^2 \quad (2.35)$$



with the mean electron velocity  $\bar{v}_e$  introduced in section 2.1. This is valid for a single sheath.

Because of the low electron density in the sheath region, it has an almost capacitive character. Hence, it can be described by a capacitance  $C_a$  and  $C_b$  and a parallelly connected diode. The diode represents the time-dependent electron current, which reaches the electrode. Because of the introduction of the diode, the ohmic resistance  $R_a$  and  $R_b$  in Fig. 2.2 can be neglected.

As mentioned in section 2.4.1, the presented models are developed in the homogeneous model of a capacitive discharge. By developing them in the inhomogeneous one, they can be deduced in an analogue way, but a disturbed electron-distribution function has to be taken into account. This is not a fixed Maxwellian any more, but it is a time-dependent function resulting from the time-varying electron density at the electron-sheath edge  $s(t)$ , which is the assumption in the inhomogeneous model. As a consequence, the main difference of these two models is the behavior of the electrons at the plasma-sheath boundary: In the inhomogeneous model, many electrons can penetrate the sheath region wherein they are reflected in contrast to the homogeneous model, where all electrons are reflected right at the plasma-sheath boundary. This difference was also seen in Fig. 2.3.

**Nonlinear series resonance heating:** The two heating models in a capacitive discharge described above, the ohmic and the stochastic heating, describe the effective power dissipation in high-pressure discharges ( $p \gg 0.1$  mbar) very well. But experiments show a divergence of the predicted power dissipation and the measured one in very low-pressure discharges ( $p \ll 0.1$  mbar) [24]. According to theory, the proportion of the ohmic heating decreases with decreasing pressure, due to the diminution of the collisions between electrons and neutrals in the plasma bulk. But the dissipated power determined in experiments is much higher than the predicted one [25]. This leads to the assumption of a third heating mechanism, caused by the nonlinearity of the plasma sheath obtained by solving their equation of motion in the inhomogeneous model [26].

The ohmic and stochastic heating are explained with the assumption of a sinusoidal rf current, which is linear to the driving voltage. By including the influence of the nonlinearity of the plasma sheath, it becomes strongly anharmonic. Some of the generated higher frequency components can be in resonance with the plasma series resonance (PSR), which arises from a periodic exchange between the kinetic electron energy in the bulk, represented by the ohmic resistance  $R_p$  and the inductance  $L_p$ , and the electric field in the sheath, represented by the capacitor  $C_s$  (see Fig. 2.2). An approximation of this frequency is given by [27]

$$\omega_{\text{PSR}} \approx \sqrt{\frac{\bar{s}}{z}} \omega_{\text{pe}}. \quad (2.36)$$

It is lower than the electron-plasma frequency at typical rf discharge parameters.

This offers the possibility of electron oscillations with  $\omega_{\text{PSR}}$ , which superimposes the excitation frequency.

By reducing the pressure, these specific oscillations are less damped, since the collisions between the electrons and the neutrals are more infrequent. Hence, their amplitude can rise and the additional electron movement in the plasma bulk results in an intensified ohmic dissipation compared to the ohmic heating on the basis of the pure sinusoidal current. This is consistent with experimental results. A detailed overview of this heating mechanism can be found in Ref. [24] and [28], the analytical description is given in Ref. [27].

The total electron-power dissipation in the high-frequency capacitive plasma is calculated by the sum of the individual contributions of the different heating mechanisms. Which one gives the main contribution sustaining the discharge is mainly dependent on the pressure. The dominant heating mechanism in a low-pressure capacitive discharge is the stochastic heating [15], whereas the nonlinear series resonance heating gains in importance – compared to the ohmic heating – the lower the gas pressure is.

### Asymmetric discharges

The analytical models of high-frequency capacitive discharges introduced above are derived with the condition of equal electrode surfaces. But the most used technical setups are asymmetric, i.e. the electrodes have different surface areas ( $A_a \neq A_b$ ). Commonly, the area of the driven electrode  $A_a$  is smaller compared to the grounded one  $A_b$ , which often represents the vessel wall of the device. This difference of the surface areas leads to a dissimilar voltage drop in the two plasma-sheath regions. The voltage drop on the driven electrode is much higher than on the grounded one due to its smaller surface area. Because of the inverse correlation of the voltage drop across the sheath and its capacitance, the capacitance of the sheath in front of the driven electrode is smaller. Provided the usual case that a blocking capacitor  $C_B$  is used for separating the biased electrode (see Fig. 2.4), the impinging charge carriers cannot flow off the electrode. Hence, a dc self bias  $U_{\text{bias}}$  is established on the driven electrode. The driving frequency and the self bias are superimposed:  $U(t) = U_{\text{bias}} + U_{\text{rf}} \sin(\omega t)$ . The self bias depends on the ratio of the electrode-surface areas  $A_b/A_a$ , as well as on the ratio of the electron densities at the plasma-sheath transition  $n_{s,b}/n_{s,a}$ . From the current continuity

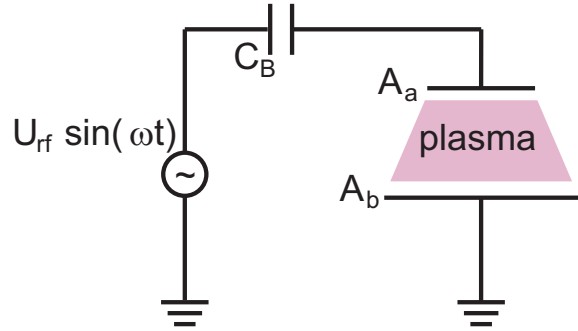


**Fig. 2.4:** Scheme of an asymmetric capacitive discharge, where the driven electrode "a" is the smaller one compared to the grounded one "b", separated from the voltage source by a blocking capacitor  $C_B$ .

$|I_a| = |I_b|$ , the following expression can be derived [15]:

$$\frac{\bar{U}_a}{\bar{U}_b} = \left( \frac{\int_{A_b} n_b(x)^{1/2} d^2x}{\int_{A_a} n_a(x)^{1/2} d^2x} \right)^4. \quad (2.37)$$

$\bar{U}_a$  and  $\bar{U}_b$  are the mean voltages, which drop over the plasma-sheath region. The dc self bias results from  $U_{\text{bias}} = -(\bar{U}_a - \bar{U}_b)$ . In the simplest case, the densities in front of both electrodes are equal,  $n_a = n_b = \text{const}$ . This leads to the basic scaling of

$$\frac{\bar{U}_a}{\bar{U}_b} = \left( \frac{A_b}{A_a} \right)^4. \quad (2.38)$$

In the case of a strong difference between the electrode areas  $A_a \ll A_b$ , the approximation  $U_{\text{bias}} \approx -U_a$  is valid [15]. This will be verified for low-frequency discharges in the next section.

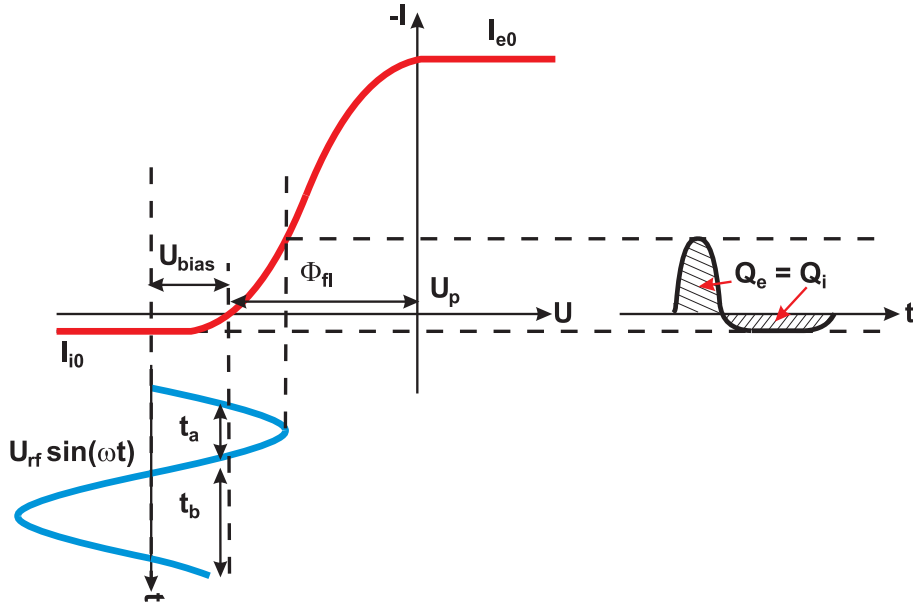


**Fig. 2.5:** Generation of a dc self bias on the driven electrode. It ensures the charge neutralization during one period cycle of the applied driving voltage [29].

The requirement for the generation of such a dc self bias is not necessarily a blocking capacitor on the driven side. An insulating effect of the electrode from ground can be obtained by an insulating layer on the electrode surface as well, as produced in plasmas which are used for depositing insulating films, e.g. silicon-oxide or silicon-nitride layers. The capacitance leads to a modified phase shift and nonlinearity of the sheath voltage as determined in the previous paragraphs of this section. To ease the consideration of the physical properties of such discharges, the insulating layer is approximated by a blocking capacitor with a high capacitance.

Thus, its impedance is low and the original voltage is barely influenced, so that the voltage on the electrode surface is approximately equal to the applied one. In the case of a blocking capacitor and an insulating layer on the electrode surface with  $C_L$  as capacitance, these two capacitances can be considered as one capacitor  $C^{-1} = C_B^{-1} + C_L^{-1}$  like in serial connection [30].

Figure 2.5 shows the adjustment of the self bias  $U_{\text{bias}}$  to the actual flowing electron and ion current on the electrode, such that the accumulated net charge on the electrode surface during one period cycle is zero. The current characteristics is similar to the one found in the probe theory of Langmuir probes [31]. The externally applied voltage  $U_{\text{rf}} \sin(\omega t)$  is oscillating around the adjusted bias voltage. In this process, electrons flow on the electrode only in the time interval, in which the current characteristics reaches the negative region, precisely " $t_a$ " in the showed example. Consequently, the ions reach the electrode during  $t_b$ . To guarantee net charge after one period cycle on the electrode, the areas under the characteristics of the electron and ion current shown on the right side of this figure must be equal. This is achieved by the shift of  $U_{\text{bias}}$  along the voltage axis. It can be seen, that not only different electrode areas or different plasma parameters in front of the electrodes lead to a generation of a self bias, but also the choice of an asymmetric driving voltage. This is discussed in detail in section 2.4.3.

## 2.4.2 Dual-frequency discharges

One main problem of capacitive discharges in terms of technological applications is the correlation of the ion and the radical flux, which amongst others determines the deposition rate on the substrate, and the energy of the impinging ions. For materials processing it is of great interest to control these two values independently. This is achieved by applying two different frequencies at the driven electrode of a capacitive discharge. These capacitive plasmas are called dual-frequency discharges. Typical frequency pairs are 27.1/2 MHz, 60/13.6 MHz and 160/13.6 MHz. Commonly, the amplitude of the higher frequency ( $U_{\text{hf}}$ ) is much lower than the one of the lower frequency ( $U_{\text{lf}}$ ). To a good approximation, this results in a separate control of the impinging ion energy on the electrode by the lower frequency ( $\omega_{\text{lf}}$ ) and the total ion density by the higher frequency ( $\omega_{\text{hf}}$ ) [32].

The analytical model of a dual-frequency discharge is based on the same assumptions as those of the model for single-frequency discharges. An additional condition is  $\omega_{pe} \gg \omega_{\text{hf}} \gg \omega_{\text{lf}} \gg \omega_{pi}$ . Hence, the electrons respond to the instantaneous electric field caused by both applied frequencies, whereas the ions only respond to the time-averaged electric field.

The modified driving current of this type of discharge is given by

$$I(t) = I_{\text{lf}} \sin\{\omega_{\text{lf}}t\} + I_{\text{hf}} \sin\{\omega_{\text{hf}}t\}. \quad (2.39)$$

Hence, the discharge parameters are determined similarly as in single-frequency

discharges, with the disregard of the electric field component generated by the higher frequency, because of  $U_{\text{hf}} \ll U_{\text{lf}}$  [33].

### 2.4.3 Low-frequency discharges

The assumption for all analyses given above was a discharge-driving frequency lower than the ion transit rate  $1/\tau_i$  across the sheath  $\omega < \omega_i = 2\pi/\tau_i$ , or simply lower than the ion-plasma frequency:  $\omega < \omega_{pi}$ . Consequently, the ions respond to the time-averaged electric field by transiting the plasma sheath. In low-frequency discharges, however, the change of the external voltage is negligible while the ions remain in the sheath region. The discharge behaves like a continuous discharge at each half period of the applied voltage. Hence, the ions respond to the instantaneous applied electric field and the analyses presented in section 2.4.1 are not valid anymore. In this case the sheath can be considered as a dc Child law sheath (section 2.3.3) with a pure resistive character due to the predominance of the conduction current compared to the displacement current. In this case, the conduction current is dominated by the ions in contrast to the discharges discussed in section 2.4.1. The bulk-plasma resistance is neglected in the following.

Low-frequency discharges sustained by a driving frequency in the kHz range are discussed in many publications [15, 29, 34, 35, 36]. They all utilize the equivalent circuit model of an asymmetric capacitive discharge (see Fig. 2.2) to describe the physical properties of these discharges. The main subject of these characterizations is the calculation of the dc self bias developed at the driven electrode. This is of special interest, because the bias voltage is often used in industrial applications to influence the ion bombardment on the substrate.

For analyzing these discharges, the electrodes are considered as perfect, plane probes. Hence, the classical probe theory [18] is taken into account with the fundamental equation of the current flowing through the plasma sheath on the electrode [37]:

$$I(t) = I_0 \left[ 1 - \exp\left(\frac{e(\Phi(t) - \Phi_{\text{fl}})}{T_e}\right) \right]. \quad (2.40)$$

$I_0 = n_s e A \sqrt{T_e/m_i}$  is the ion-saturation current and  $\Phi(t)$  the time-dependent electrode potential, which implies the externally applied voltage and the developed self bias. In the equilibrium state, the currents flowing on both electrodes during one period cancel out. This is expressed by

$$\int_0^T I(t) dt = 0. \quad (2.41)$$

In Ref. [38], the self bias is calculated as a function of different parameters and for different input voltage wave forms. Here, the derivation for the case of a symmetric rectangular pulse with an amplitude of  $U_0$  applied to electrode "a" is outlined. The voltage form is defined as

$$\begin{aligned} U_{\text{ext}} &= U_0 & \text{for } 0 \leq t < T/2 \\ U_{\text{ext}} &= -U_0 & \text{for } T/2 \leq t < T. \end{aligned} \quad (2.42)$$

In the phase interval  $0 \leq t < T/2$ , electrode "a" can be considered as the anode and electrode "b" as the cathode, due to the fact, that the current at the anode is electron dominated and at the cathode ion dominated. In the second time interval, the anode and cathode are exchanged. From these conditions, the time-dependent potential at the two electrodes is

$$\begin{aligned} \Phi_a &= \Phi_{\text{fl}} & \text{and } \Phi_b &= \Phi_{\text{fl}} - U_0 + |U_{\text{bias}}| & \text{for } 0 \leq t < T/2 \\ \Phi_a &= \Phi_{\text{fl}} - U_0 - |U_{\text{bias}}| & \text{and } \Phi_b &= \Phi_{\text{fl}} & \text{for } T/2 \leq t < T. \end{aligned} \quad (2.43)$$

Equation (2.43) describes the voltage of both electrodes during the whole period. But only two of these equations are independent, because the resulting current at both electrodes must be equal. In the following, only the actual cathode, and therefore the ion current, is considered. Hence, by inserting Eqs. (2.40) and (2.43) into (2.41), the result is

$$\begin{aligned} I_{b0} \int_0^{T/2} \left[ 1 - \exp \left( -\frac{e(U_0 - |U_{\text{bias}}|)}{T_e} \right) \right] dt \\ - I_{a0} \int_{T/2}^T \left[ 1 - \exp \left( -\frac{e(U_0 + |U_{\text{bias}}|)}{T_e} \right) \right] dt = 0. \end{aligned} \quad (2.44)$$

By solving Eq. (2.44) for the self bias, the following expression is obtained:

$$|U_{\text{bias}}| = U_0 \left\{ 1 + \frac{T_e}{eU_0} \ln \left[ \frac{\eta - 1}{2\eta} + \sqrt{\left( \frac{\eta - 1}{2\eta} \right)^2 + \frac{1}{\eta} \exp \left\{ -2\frac{eU_0}{T_e} \right\}} \right] \right\}, \quad (2.45)$$

with the substitution  $\eta = I_{b0}/I_{a0}$ . Assuming  $T_{e,a} = T_{e,b} = T_e$ , the parameter  $\eta$  gives the ratio of the products of the electrode areas and the electron densities,  $\eta = n_{s,b}A_b/(n_{s,a}A_a)$ . For the usual case  $eU_0 \gg T_e$ , thus Eq. (2.45) can be reduced to the simplified form

$$|U_{\text{bias}}| = U_0 \left\{ 1 + \frac{T_e}{eU_0} \ln \left[ \frac{\eta - 1}{\eta} \right] \right\}. \quad (2.46)$$

For different electron temperatures and voltage amplitudes, Fig. 2.6 shows  $|U_{\text{bias}}|$  in dependence of the electrode area ratio  $\eta$  under the assumption of equal electron

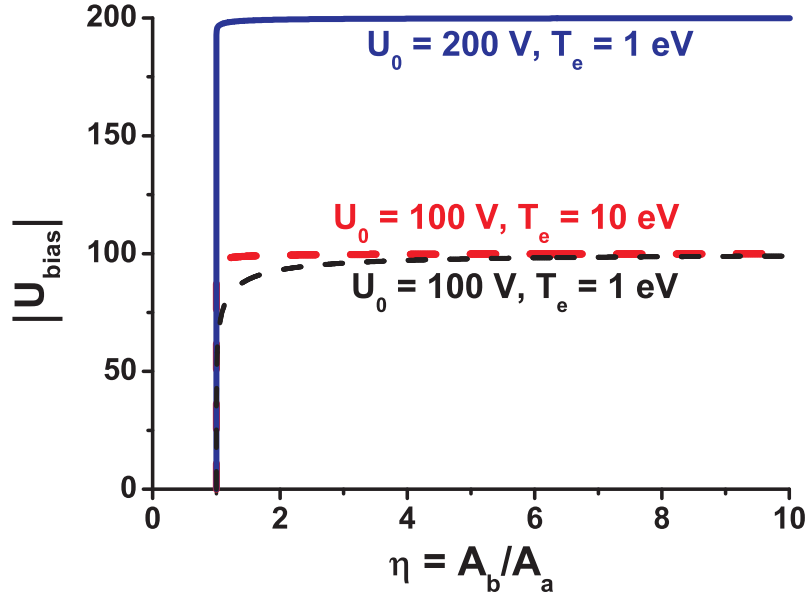


**Fig. 2.6:** Dependence of the dc self bias voltage  $U_{\text{bias}}$  on the electrode-area ratio  $\eta$  in the case of a symmetric rectangular driving voltage.

densities  $n_{s,a} = n_{s,b}$ . For  $\eta \leq 1$  ( $A_b \leq A_a$ ),  $U_{\text{bias}}$  is not defined. For  $A_b \gg A_a$ , the value of the self bias converges to the amplitude  $U_0$  of the applied voltage. Hence, the ions at the smaller electrode are accelerated by approximately the entire amplitude of the applied voltage, namely  $U_0$ . Furthermore, the electron temperature influences the dependence on the electrode-area ratio. If  $T_e$  is low, the convergence of  $U_{\text{bias}}$  to  $U_0$  is smoother than in the case of higher electron temperatures.

Most discharges are driven by a sinusoidal voltage. The solution of the specific equations is analogue to the one described for the rectangular pulse. The result is the self bias [15]

$$U_{\text{bias}} = U_0 \sin \left( \frac{\pi n_{s,b} A_b - n_{s,a} A_a}{2 n_{s,b} A_b + n_{s,a} A_a} \right). \quad (2.47)$$

In conclusion, the dc self bias developed at the driven electrode is strongly influenced by the shape and the amplitude of the externally applied voltage. In comparison, the self bias for the rectangular voltage wave form is larger than the one caused by the sinusoidal driving voltage [38]. Therefore, a rectangular pulse leads to a stronger influence on the energy of the ions impinging the electrode.

All these results are obtained under the assumption, that the electrode surface is conducting. In the case of an insulating layer on the electrode surface, a potential difference through the insulating film is developed. Hence, the voltage at the layer surface (the voltage, which drops across the plasma sheath) is not the same as the externally applied one. The limit of the applied frequency, above which the effect

of an insulating electrode surface can be neglected, is given by Ref. [35]

$$f = \frac{2dI_{i0}}{\epsilon\epsilon_0U_0} \sqrt{\frac{2 \ln(\pi eU_0/(2T_e))}{\pi}} \quad (2.48)$$

for sinusoidal voltage forms, with the layer thickness  $d$  and  $\epsilon$  the permittivity of the insulating material.

## 2.5 Microwave discharges

Microwave discharges exhibit another possibility of generating industrially used plasmas. They form, compared to capacitively coupled plasmas, a low potential, and thus a very small plasma sheath in front of the substrate. Hence, the ions are accelerated to the substrate by a lower voltage drop. For some applications, this is a great advantage compared to capacitively coupled discharges, because a damage of the substrate itself caused by impinging ions can be avoided. This is important for the treatment of sensitive substrates like, e.g. foils. But consequently, there is no possibility to influence the layer growth by a well-directed ion bombardment. The various deposition processes are discussed in more detail in section 2.6.

Another advantage of microwave plasmas concerning deposition processes is their relatively high density compared to capacitively coupled rf plasmas. A typical microwave discharge offers an electron density of a few  $10^{17} \text{ m}^{-3}$ , whereas in rf plasmas, the density is about  $10^{15} - 10^{16} \text{ m}^{-3}$ . The higher plasma density leads to an increased deposition rate, which results in a higher cost effectiveness of the industrial production.

The most commonly used frequency in industrial applications is 2.45 GHz. Mainly magnetrons are utilized as microwave sources. In a low-pressure regime, the plasma-production process is irradiated through the few stochastic electrons, which are always existent due to the cosmic radiation and then accelerated in the field of the incoming high-frequency electromagnetic wave. Because of their inertia, the ions are regarded as a stationary background gas.

The time-dependent velocity of the oscillating electrons is given by [39]

$$\mathbf{v}(t) = -\frac{e}{m_e} \text{Re} \left\{ \frac{\mathbf{E}}{\nu_m + i\omega} \exp(i\omega t) \right\} \quad (2.49)$$

with the applied electric field  $\mathbf{E}$  and the collision frequency  $\nu_m$  of electrons and neutrals. By these collisions, the kinetic energy of the electrons is thermalized and thus used to heat the electrons. The mean power transferred to one electron from the oscillating field is [39]

$$P = - \int_0^T \mathbf{E}(t) \cdot \mathbf{v}(t) dt = 2\nu_m \bar{u} \quad (2.50)$$



with the mean kinetic energy

$$\bar{E} = \frac{1}{2} m_e \bar{u}^2(t) = \frac{e^2 E_p^2}{4m_e (\nu_m^2 + \omega^2)}, \quad (2.51)$$

and the sum of the squared field intensities in the three dimensions  $E_p^2 = E_x^2 + E_y^2 + E_z^2$ . Here, two cases have to be distinguished:

- The electrons do not collide,  $\nu_m = 0$ : Then  $P = 0$ , i.e. the electrons oscillate without interacting with other particles, due to the fact that the electron velocity is  $\pi/2$  out of phase with the electromagnetic field. Hence, the electrons do not gain energy from the externally applied electric field.
- The electrons do collide,  $\nu_m \neq 0$ : By colliding almost elastically with the particles of the background gas (ions and neutrals), the electrons change the direction of their velocity, but their kinetic energy remains roughly constant. Hence, they are thermalized, this means they gain energy from the electric field.

In general, the mean kinetic energy of the electrons over one period is far away from the energy required for excitation or ionization of the neutrals. But due to the steady elastic collisions of the electrons with the background gas, they absorb energy from the applied field continuously, until they can carry out an inelastic collision to ionize a neutral particle. After this, the electrons only have a small amount of energy, and the complete energy buildup starts again.

The most important loss of charge carriers in the plasma is their recombination at the wall (wall losses). Consequently, the ionization rate in the plasma must be higher than the recombination rate to sustain the plasma.

The relative permittivity gives insight into the high-frequency properties of a plasma (from electron motion):

$$\epsilon = 1 - \frac{\left(\frac{\omega_p}{\omega}\right)^2}{1 + \left(\frac{\nu_m}{\omega}\right)^2} - i \frac{\nu_m}{\omega} \frac{\left(\frac{\omega_p}{\omega}\right)^2}{1 + \left(\frac{\nu_m}{\omega}\right)^2}. \quad (2.52)$$

In the limiting case of  $\nu_m = 0$  and for  $\omega_p \leq \omega$ , the relative permittivity is real and, hence, the refractive index, which is defined as  $N = \sqrt{\epsilon}$ , is a real value as well. This permits penetration of the irradiated wave into the plasma. For  $\nu_m \ll \omega$ , which is the case in low-pressure depositing plasmas, the approximation of a real relative permittivity is valid:

$$\epsilon = N^2 = 1 - \left(\frac{\omega_p}{\omega}\right)^2 \quad (2.53)$$

The second limiting case is  $\omega = \omega_p$ , which results in a refractive index of zero. At the so-called cutoff, the irradiated wave is reflected and cannot penetrate further

into the plasma. The cutoff density can be determined to

$$n_c = \frac{\epsilon_0 m_e}{e^2} \omega^2 \quad (2.54)$$

from the definition of the plasma frequency in Eq. (2.4). In many cases, microwave discharges offer a clearly higher electron density than their cutoff density. This is a result of the collisions between electrons and neutrals: Thus, the boundary at the cutoff is blurred and the electromagnetic wave can penetrate even at higher plasma densities to sustain the plasma. The cutoff density for microwaves at 2.45 GHz is  $n_c = 7.45 \cdot 10^{16} \text{ m}^{-3}$ .

To generate microwave plasmas, different concepts are established, as there are, e.g., atmospheric-pressure microwave discharges, resonator plasmas or magnetically confined plasmas. They are applied on the specific demand of the deposition process. The plasma source used in this work – the so called Duo-Plasmaline [40] – is another method to generate a low-pressure microwave plasma and is presented in section 3.2.2.

## 2.6 Various deposition processes

The energy of the ions impinging on the substrate surface and, hence, the potential drop in the sheath region, plays an essential role in deposition processes. In this section, the properties of the plasma sheath in capacitive and microwave discharges are opposed. Therefore, the different methods of injecting the power into the plasma for sustaining the discharge have to be considered.

To sustain microwave discharges, an electromagnetic wave is irradiated into the plasma (section 2.5). Thus, parts of the periphery like the enclosure of the device, probes or stages, form passive electrodes. The properties of the dc plasma sheath generated in front of these electrodes were introduced in section 2.3. The dimensions of the sheath are dependent on the floating potential (Eq. (2.8)) and the plasma density of the particular discharge. For instance, the thickness estimated for a high-voltage sheath (Eq. 2.20) in an oxygen plasma with typical discharge parameters for a microwave plasma  $T_e = 1 \text{ eV}$ ,  $n_s = 1 \cdot 10^{17} \text{ m}^{-3}$  is  $s = 32.5 \mu\text{m}$ , and the floating potential is  $\Phi_{fl} = 2.1 \text{ V}$ . This value gives an order of magnitude estimation. The potential decay in the sheath region, in this case the floating potential, is responsible for the acceleration of the ions. From the low value of the floating potential it follows that in microwave generated plasmas the effect of the plasma sheath can be neglected and the ions impinge with about 1 eV on the substrate.

The power for sustaining capacitive discharges is injected in a different way, namely by applying an alternating voltage to the electrode of the setup (section 2.4). Thus, this is an active electrode, and the value of the applied voltage determines the potential drop in the adjacent plasma sheath, and therewith the energy of the impinging ions. To calculate the ion energy, the relation between the driving frequency

$\omega$  and the ion- and electron-plasma frequency has to be considered. For a typical discharge with a rf driving frequency of 13.56 MHz, the electron density is about  $1 \cdot 10^{16} \text{ m}^{-3}$ . The electron temperature is assumed to be 1 eV like in the microwave discharge described above, as well as oxygen as source gas. Hence, the ion-plasma frequency is  $\omega_{pi} = 32.9 \text{ MHz}$  and the electron-plasma frequency  $\omega_{pe} = 5.6 \text{ GHz}$ . For three cases of driving frequencies, the differences in the ion and electron current as well as in the ion energy are depicted in Fig. 2.7:

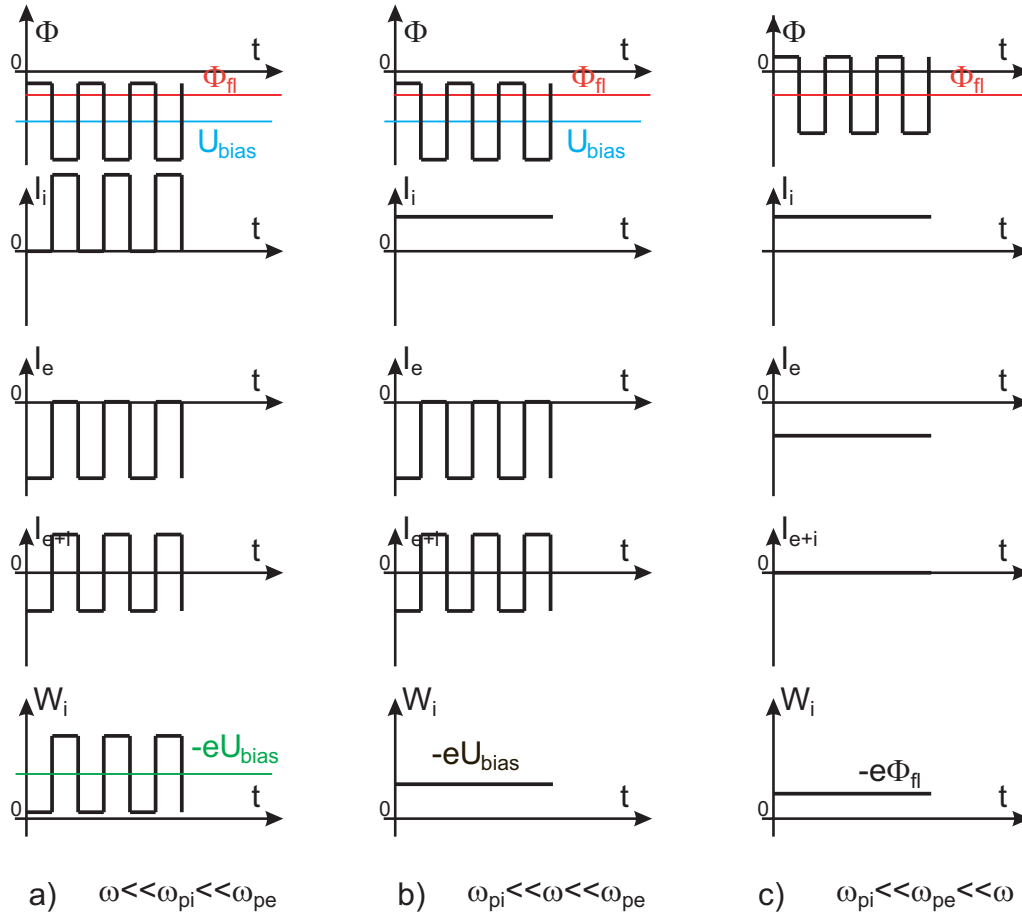


**Fig. 2.7:** Time dependence of ion, electron and total current and ion energy hitting the biased electrode as a function of the applied rectangular substrate bias in the case of a) the bias frequency being lower than the electron- and ion-plasma frequency, b) the bias frequency being higher than the ion-, but lower than the electron-plasma frequency, c) the bias frequency being higher than the ion- and electron-plasma frequency, from Ref. [39].

- a) The rf excitation frequency is lower than the ion- and the electron-plasma frequency,  $\omega \ll \omega_{pi} \ll \omega_{pe}$ :  
 The ion as well as the electron current to the driven electrode is time-dependent and oscillating according to the applied voltage. These characteristics are

shown in Fig. 2.7a. The energy of the impinging ions also varies in time around the value of  $W_i = -eU_{\text{bias}}$  with the frequency of the rf driving frequency. The maximum of the energy is given by [39]

$$W_{\text{max}} = e \left( 2U_0 - \Phi_{\text{fl}} - \frac{T_e}{e} \ln 2 \right). \quad (2.55)$$

Due to the fact that the sheath corresponds to a dc biased sheath in each half period of the applied alternating voltage (see section 2.3.3), the sheath thickness can be calculated to  $s = 1.86 \cdot 10 \text{ m}^{-3}$  (Eq. (2.20)) with the plasma parameters defined above and the applied voltage assumed to be  $U_0 = 100 \text{ V}$ . Apparently, the sheath thickness is much larger than in the case of the microwave discharge.

- b) The rf excitation frequency is in the range between the ion- and the electron-plasma frequency,  $\omega_{pi} \ll \omega \ll \omega_{pe}$ : The total current characteristics is the same as for low-frequency discharges, but the characteristics of the energy of the ions reaching the electrode is different. The ion energy is time-independent, due to the fact that the ions cannot respond to the instantaneous electric field in the sheath region. The ions impinge with a constant energy of  $W_i = -eU_{\text{bias}}$  on the electrode surface. This behavior is illustrated in Fig. 2.7b. In this case, the energy is given by [39]

$$W_i = e \left( U_0 - \Phi_{\text{fl}} - \frac{T_e}{e} \ln 2 \right). \quad (2.56)$$

Compared to the low-frequency discharges, the ion energy is clearly lower [41]. Hence, the effect of an ion bombardment in case of a low-frequency discharge is larger.

The ion-sheath thickness can be calculated by the equation of an oscillating sheath, Eq. (2.27). For the same parameters as above, it is  $s = 2.53 \cdot 10 \text{ m}^{-3}$ . Hence, it is of the same order of magnitude as in the low-frequency discharge, i.e. higher than in the case of microwave discharges.

- c) The rf driving frequency is higher than the ion- as well as the electron-plasma frequency,  $\omega_{pi} \ll \omega_{pe} \ll \omega$ : In this case, neither the ions nor the electrons respond to the temporal variation of the applied electric field. Hence, both the electron and the ion current is constant in time and, therefore, the total current on the electrode as well. This leads to the situation comparable with a passive electrode, i.e. the potential decay in the sheath region only depends on the appearing floating potential. Hence, the ion energy hitting the electrode is  $W_i = -e\Phi_{\text{fl}}$ , which is depicted in Fig. 2.7c. This means, the applied voltage has no influence on the ion bombardment of the electrode.

In conclusion, the effect of the plasma sheath with respect to the energy of the ions impinging on the electrode surface can be neglected because of the low potential decay in the sheath region in microwave discharges. Hence, these discharges are suitable for depositing heat-sensitive or damageable substrates like plastic foils. Moreover, coatings which should be grown without any influence of energetic ions can be deposited perfectly in such discharges.

If the growth process needs to be modified by an ion bombardment and with it by an additional application of energy, a capacitive discharge is preferable. In this process, the driving frequency must be lower than the electron-plasma frequency to guarantee a sufficient voltage drop in the sheath region, such that the ion energy can be regulated. The application of increased energy leads to an increased surface mobility of the particles on the surface of the deposited film, whereby a smoothing of the surface of the growing layer can be achieved as well as an increase of the film density or a modification in the molecular composition of the layer due to the possibility of building higher energetic chemical bonds.

To provide the opportunity of an ion bombardment of the substrate surface in a microwave discharge, a bias voltage has to be applied to the substrate holder. If conducting layers are deposited, a negative dc bias is sufficient to increase the energy of the positive ions in the sheath region and the result is a dc high-voltage plasma sheath as described in section 2.3.3. But in the case of an insulating film on the electrode, the accumulated charge repels these ions. To guarantee a continuous flow of ions to the substrate surface, the charge carriers have to be neutralized. This is realized by an alternating substrate voltage. The result is a combination of a capacitive discharge and the microwave plasma. Mostly, the substrate holder is the driven electrode and the enclosure of the device is the grounded one. To describe the properties of the sheath in front of the driven electrode, the theory of a plasma sheath in a pure capacitive plasma can be used. The microwave discharge is only responsible for the plasma density, and therefore for the absolute particle flux. Hence, the ion and the radical flux, which is responsible for e.g. the deposition rate, can be regulated by the parameters of the microwave plasma, whereas the ion energy to the substrate, and therefore the surface mobility of the film-forming particles, is determined independently by the applied bias voltage. This situation corresponds to the one in a dual-frequency discharge (section 2.4.2). But a great advantage is the exploitation of the higher density of the microwave plasma, which offers a higher deposition rate compared to the pure capacitive dual-frequency discharges. In this work, such a combined setup is investigated under the detailed aspects of surface modifications in plasma processing.



# Chapter 3

## Experimental setup

For the insulating and diffusion-preventing thin films deposited in this work, two different coating systems are taken into consideration, namely silicon-oxide ( $\text{SiO}_x$ ) and silicon-nitride ( $\text{SiN}_y$ ) layers. These coating systems, as well as the gas systems from which they are deposited, are introduced in section 3.1. In addition, the deposition of hydrogenated amorphous silicon (a-Si:H) is examined as a simple model system for the comparison of experimental and simulation results, which are important for the understanding of the mechanisms leading to the observed shape of the growing layer at positions of indentations in the substrate surface. By analyzing these mechanisms, the development of pinholes in the barrier layer on substrates with a rough surface can be understood.

All these coatings are produced in a low-pressure microwave-plasma device, called Plasmodul [4]. In order to manipulate the layer growth by an increased ion bombardment, especially at positions of cavities on the substrate surface, an alternating substrate bias is applied. The complete experimental setup and its properties is presented in section 3.2. In section 3.3, the diagnostics, which are used for determining the coating characteristics, are introduced. Details on the Fourier-transform infrared (FTIR) spectroscopy and the photospectrometer are given in section 3.3.1 and 3.3.2, respectively. The plasma parameters in the Plasmodul are measured by Langmuir double probes, which are explained in section 3.3.3. The corresponding measurements of the plasma parameters are described in section 3.4.

### 3.1 Coating systems

The  $\text{SiO}_x$  coatings are deposited in a gas mixture of **hexamethyldisiloxane** (HMDSO) and oxygen ( $\text{O}_2$ ), the  $\text{SiN}_y$  layers in a mixture of monosilane ( $\text{SiH}_4$ ) and ammonia ( $\text{NH}_3$ ). The amorphous silicon films are deposited in a pure monosilane plasma. The motivation of the choice of these gases as well as their chemical reactions in the plasma and the particles, which contribute to the layer growth in these systems, will be introduced in the following.

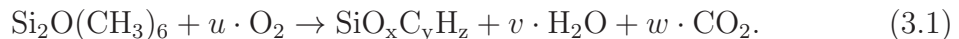
### 3.1.1 The silicon-oxide coating

To produce thin  $\text{SiO}_x$  coatings with barrier properties like for insulation and diffusion prevention in a low-pressure PECVD process, siliceous gases with a surplus of oxygen were presented as suitable precursors in previous works [42, 43, 44]. One of the common precursors used for depositing these layers is HMDSO, which is mainly utilized for scratch resistant or diffusion barriers in industry [45, 46, 42]. The most common precursor for insulating barrier layers, on the other hand, is tetraethoxysilane (TEOS). The origin of its application can be found in the semiconductor industry in the 1980's [41, 47, 48], where an insulating layer is deposited on electrical components. For this purpose, the coating has to provide good step coverage. This is achieved with TEOS [49] because of its high surface mobility in contrast to HMDSO [48].

The objective of this work is to create barrier layers, which fulfill all demands simultaneously, i.e. insulating and diffusion-preventing layers with a good step coverage at the same time. The used precursor is HMDSO, which was shown to give good results for insulating and diffusion preventing coatings [50, 51]. In order to improve the step coverage additionally, a separate substrate bias is implemented (section 3.2.3).

HMDSO is a transparent, water-insoluble silicon oil and is available as a liquid at room temperature. Its melting and boiling points are  $-59$  and  $101$  °C, respectively. Due to the fact that the vapor pressure of HMDSO is  $3.7$  kPa, a gas flux up to  $20$  sccm into the vacuum chamber with a typical pressure of  $0.1$  to  $0.3$  mbar is guaranteed.

The HMDSO molecule consists of six methyl ( $\text{CH}_3$ ) groups, which surround a silicon-oxygen-silicon group. Its molecular formula is given by  $\text{Si}_2\text{O}(\text{CH}_3)_6$ . In the plasma, the precursor is dissociated and the following particles can be generated by an addition of oxygen to the plasma: By oxidizing the methyl groups of the HMDSO with elementary oxygen, the byproducts carbon dioxide ( $\text{CO}_2$ ) and water ( $\text{H}_2\text{O}$ ) are produced, which are pumped out. An additional dissociation product is  $\text{H}_2$ . In addition to these volatile compounds, an amorphous  $\text{SiO}_x$  structure is developed on the substrate, which can contain parts of OH and methyl ( $\text{CH}_x$ ) groups. The ratio of these groups can be regulated by the ratio of the gases [51, 52]. A simplified equation for the chemical reactions in the HMDSO- $\text{O}_2$  plasma is described by:





The coating with best barrier properties was found in a gas-mixture ratio of HMDSO : O<sub>2</sub> = 1 : 20 [50]. Such SiO<sub>x</sub> coatings with a high oxygen compound are often referred to as quartz like films in literature because of their quartz like structure (SiO<sub>2</sub>). A simple theoretical calculation shows [51], that a gas-mixture ratio HMDSO : O<sub>2</sub> of at least 1 : 12 is needed to deposit this layer. At a lower mixture ratio, organic compounds like CH<sub>x</sub>, SiH and also OH groups can be inserted in the coating, since the methyl groups of the HMDSO are not completely oxidized. The different proportions of the molecular groups in the coatings will be described in detail in chapter 6.

### 3.1.2 The silicon-nitride coating

The second coating system used in this work for depositing barrier layers are the silicon-nitride (SiN<sub>y</sub>) films. They are deposited in a gas mixture of monosilane and ammonia. In the semiconductor industry, nitrogen is often used instead of ammonia [53, 54]. In contrast to nitrogen, the ammonia molecule can be dissociated more easily into atomic nitrogen and hydrogen than breaking the triple bond of the nitrogen molecule. This leads to a higher rate of yield of atomic nitrogen in an ammonia plasma and, therefore, is of special interest for this work. Because of the classification of the two utilized gases as dangerous substances, their handling is tenuous. Monosilane is a colorless, extremely flammable gas, which ignites spontaneously at any contact with oxygen. Thus, any possible contact with the ambient air must be prevented. The employment of ammonia is not that critical. Indeed it is a caustic gas, but it smells intensely even if it has not reached the maximum workplace concentration value.

In the plasma, the two gases split into their particular components, namely silicon, nitrogen and hydrogen. Hence, the deposited layer has the structure of Si<sub>x</sub>N<sub>y</sub>H<sub>z</sub>, and the surplus nitrogen and hydrogen are exhausted. The corresponding reaction equation is



Similar to the deposition of the SiO<sub>x</sub> coatings, the final composition of the SiN<sub>y</sub> layers can be regulated by the ratio of the two gases. In former work [50], it was shown that coatings deposited in a gas mixture of SiH<sub>4</sub> : NH<sub>3</sub> = 3 : 22, which corresponds to a monosilane portion of 12 %, can achieve the best barrier properties. Detailed investigations of the influence of the gas-mixture ratio on the molecular composition of the silicon-nitride layers were done in [55].

### 3.1.3 The deposition of silicon layers

For detailed analyses of the film-forming processes by simulating the layer growth (chapter 5), a simple coating system is needed, in which chemical reactions are

as irrelevant as possible for the deposition process. Using the deposition of the silicon-nitride films as starting point, such a system is easily accessible by omitting the carrier gas ammonia. The resulting coating in a pure monosilane plasma is – depending on the process parameters – hydrogenated amorphous silicon (a-Si:H) or microcrystalline silicon ( $\mu$ -Si). Thin-film silicon applications are often used as technological applications like photoreceptors, thin-film transistor arrays for liquid-crystal displays or especially in the photovoltaics [56]. Hence, the growth processes of these layers are of great research interest (see, e.g., [57, 58, 59, 60]).

In the  $\text{SiH}_4$  plasma, the molecules are dissociated by collisions with high-energetic electrons into different ions, radicals and molecules in an electronic excited state. An overview of the dissociation pathway of the silane molecule is given in [57, 61]. Most of these particles are highly reactive, and have a very short lifetime in contrast to the  $\text{SiH}_3$  radicals and the atomic hydrogen, which shows low reactivity in the silane plasma. Consequently, the density of the  $\text{SiH}_3$  radicals and atomic hydrogen is much higher than the density of the other species. Thus, it is reasonable to assume that these radicals in combination with the hydrogen are the dominant chemical species for the growth process in this deposition process.

Which kind of silicon film grows depends on the deposition conditions: With the substrate temperature and optionally with an additional hydrogen content in the  $\text{SiH}_4$  plasma, the microcrystallite volume fraction of the otherwise growing undiluted a-Si:H layer can be regulated. For these two types of silicon layers, different growth models exist.

A schematic of the formation of the amorphous silicon film is shown in Fig. 3.1. The bonds on the surface of the coating are saturated with adsorbed hydrogen. By reaching the surface, the  $\text{SiH}_3$  radicals start to diffuse on the surface area. In doing so, they can be reflected at the surface as  $\text{SiH}_3$ , form  $\text{Si}_2\text{H}_6$  with another radical and leave the surface, detract a bonded hydrogen and leave the surface as a  $\text{SiH}_4$  molecule, leaving a dangling bond on the layer surface behind. Or it can assume a Si-Si bond with an already existent dangling bond. This is the only effective contribution to the layer growth. The Si-Si bond is formed with the sticking probability  $s$ . Consequently, the loss probability of an  $\text{SiH}_3$  radical can be expressed by  $1 - s$ .

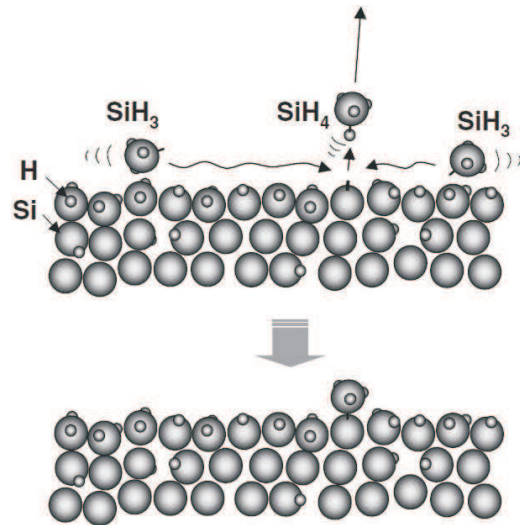


**Fig. 3.1:** Scheme of the layer-growth process in a  $\text{SiH}_4$  plasma, from Ref. [57].

The processes, which lead to the formation of a  $\mu$ -Si layer, are not as well understood as the formation of an amorphous network structure. In general, a substrate temperature between 300 and 400 °C and a defined hydrogen content in the plasma is needed. To describe the possible influence of these two conditions on the film growth, three different growth models for the  $\mu$ -Si layer exist. In the *diffusion model*, a complete coverage of the coating surface with bonded hydrogen caused by the high H flux is assumed. Additionally, local heating by hydrogen-exchange reactions is produced. These two processes lead to an increased surface diffusion of the impinging  $\text{SiH}_3$  radicals. Hence, the accumulated  $\text{SiH}_3$  radicals on the growing layer surface build high-energetic chemical bonds, which lead to a microcrystalline configuration. The *etching model* describes the breakage of existing weak Si-Si bonds by impinging atomic hydrogen. This leads to the survival of the strongest Si-Si bonds, which causes the microcrystallinity of the layer. The third explanation delineates the insertion of hydrogen into the subsurface of the growing film by alternating treatment of the layer surface in a  $\text{SiH}_4$  and H plasma. This is the *chemical-annealing model*.

## 3.2 The Plasmodul

The Plasmodul [4] is a low-pressure microwave plasma device. It has a modular design and can be adapted to different demands like etching, activation (modification of the surface structure), sterilization or deposition, for which it is used in this work. The modular construction allows to employ various diagnostics without a complex reconstruction of the device. The dimensions of this laboratory device are handy, but its principle can be copied to plasma devices on industrial scales.

### 3.2.1 The coating setup

To guarantee the modular handling of the Plasmodul, each task is integrated in its own module and, hence, the different parts can be substituted easily. This ensures a quick adaption of the setup to the particular demand of the plasma process. In the present setup, the whole device has a cylindrical basic form with an outer diameter of 35 cm and a height of 52 cm. The separate modules are aluminum rings with a wall thickness of 2.5 cm. The separate modules sealed with O-rings are placed on each other and fixed by a fastening. Besides the O-ring, a microwave sealing consisting of a wire mesh, is fixed in an own cavity.

The configuration used in this work consists of eight modules. The main parts are the two separate gas inlets, the plasma source and the reaction chamber. With the top-arranged exhaustion, they build an upstream plasma device. The advantage of such a configuration is the possibility of an overhead deposition, which prevents a contamination of the substrate with down-falling tinsels. A schematic view of the device with the particular modular parts is illustrated in Fig. 3.2. A picture of the setup and the applied diagnostics is shown in Fig. 3.3.

The reactor is completed at the bottom and at the top with a plane cover plate. The plasma source, which consists of an array of four Duo-Plasmalines [40] (details see section 3.2.2), is embedded into the two gas inlets. With the frequency of 2.45 GHz fed in the Duo-Plasmalines, this leads to a remote microwave plasma deposition process. The supplied microwave power can be regulated up to  $2 \times 1.2$  kW, the standard setting for the presented coatings is  $2 \times 600$  W. In this configuration the carrier gases, oxygen or ammonia, are injected by an electronic mass-flow controller from MKS Instruments GmbH with up to 100 sccm through the lower gas inlet, which is subdivided into four upwardly oriented tubes in order to ensure a uniform gas flow through the whole setup area. The precursor gases, HMDSO or monosilane, are fed remotely in the upper gas inlet, which is split symmetrically into 16 gas outlets leading to a homogeneous deposition on the substrate. The configuration of the gas inlets was optimized for this deposition device in a former work [50]. The monosilane is injected by an electronic mass-flow controller with up to 30 sccm, whereas the HMDSO is fed in by a leak valve and an electronic mass-flow meter since HMDSO is liquid at room temperature. This remote plasma configuration was chosen to prevent a rapid deposition on the quartz tubes of the plasmalines and the quartz windows of the source module, which are installed at three sides to permit spectroscopic investigations of the plasma.

Above the upper gas inlet, the reaction chamber is installed with a separating ring acting as a distance piece between the reaction chamber and the module of the upper gas inlet. The main component of the reaction chamber is the substrate holder, at which the samples are fixed overhead. It has a round shape with a diameter of 16.5 cm. Hence, it is possible to deposit substrates up to  $10 \times 10$  cm<sup>2</sup>, which are fastened with retaining clips. The stage is installed at a drawer, which can be opened at the front of the device. Hence, the samples can be replaced easily, and the time, during which the vacuum chamber is

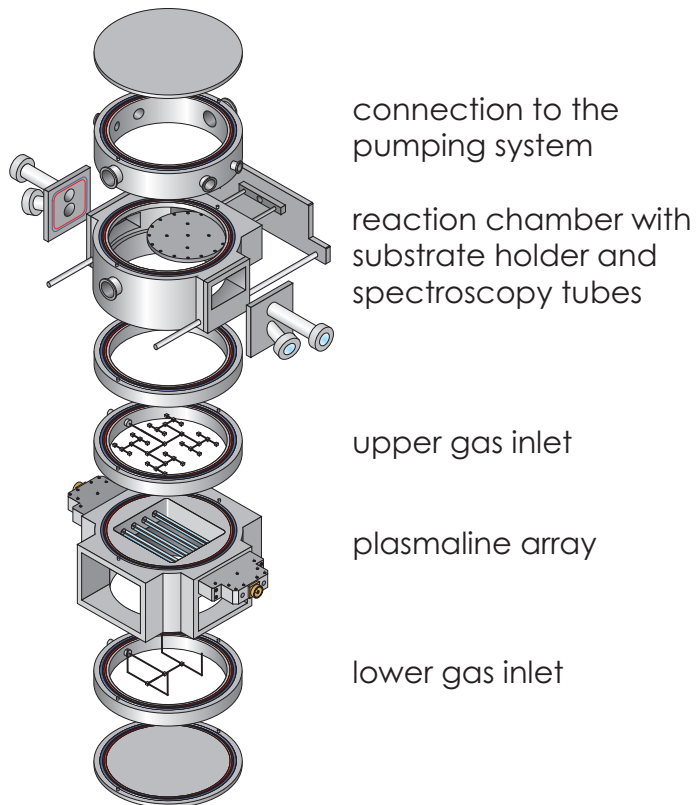


**Fig. 3.2:** Schematic view of the used configuration of the Plasmodul, from [51].

vented, is kept short. The distance between the substrate holder and the plasmaline array is 20 cm.

A new feature in this work is the possibility of applying a bias voltage at the substrate holder. For this purpose a new substrate holder was designed and installed. It can be biased by a bipolarly pulsed power supply RPG-50 from MKS Instruments, Inc. [62]. The power supply is connected via a high-voltage BNC vacuum feedthrough embedded in a DN 40 ISO-K blank flange at the front of the drawer and the cable is connected centrally to the top of the stage. To guarantee the insulation of the sample stage against the other components of the setup, it is fixed via ceramic slats at the drawer. This prevents a sparking of the bias voltage on the enclosure of the device. Detailed information about the characteristics of the substrate bias will be given in section 3.2.3.

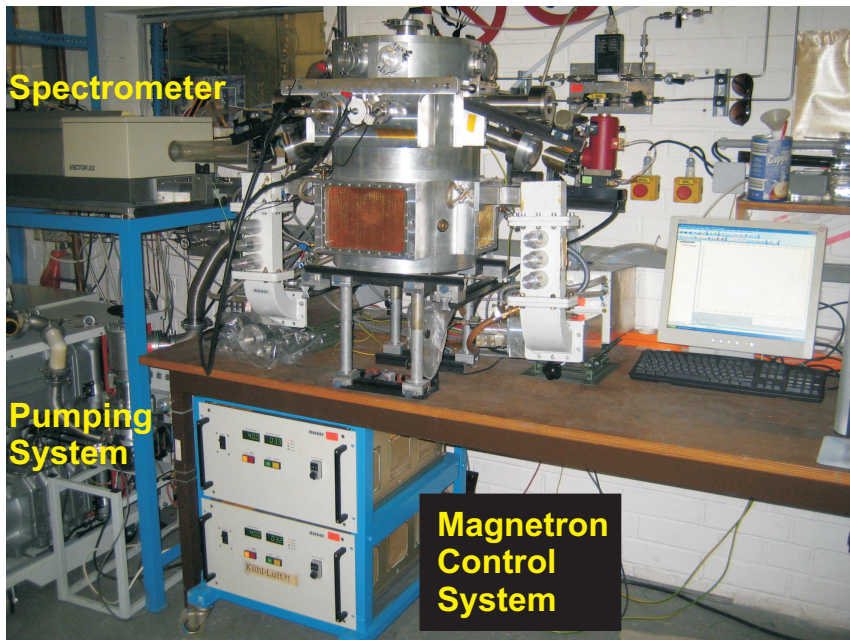


**Fig. 3.3:** Plasmodul with adapted FTIR spectroscopy, magnetrons and pumping system.

Additionally, the substrate holder contains a mica heating plate from Telemeter Electronic and, hence, its temperature can be regulated up to 600 °C to guarantee a constant, but variable substrate temperature during the deposition process. For most of the coatings within this work, it was kept constant at  $T = 250\text{ °C}$ <sup>1</sup> [50]. Its power supply is connected via a feedthrough, which is embedded in a DN 20 ISO-K blank flange besides the feedthrough of the bias voltage. The temperature is controlled by a NiCr temperature sensor from Thermocoax, which is inserted by a squeezing lead-through. The whole device of the sensor has to be insulated against other components of the deposition chamber, mainly to prevent a conduction of

<sup>1</sup>When applying the bias on the substrate holder, however it cannot be kept constant. The temperature can increase up to 350 °C likely due to the impinge of high-energetic ions.



the bias signal. This is realized by embedding the sensor in a ceramic tube, which insulates it against the substrate holder. The lead-through is fixed in a teflon blank flange to prevent a contact with the enclosure of the Plasmodul.

The second part of the reaction chamber are the spectroscopy components, which are attached to both sides of the module. Each of them consists of two tubes. One of the tubes is installed in an angle of  $90^\circ$ , i.e. perpendicular to the substrate holder and contains a quartz window to enable spectroscopic investigations on the plasma in front of the substrate holder. The other one is installed in an angle of incidence of  $72^\circ$ . It is used for measuring in-situ FTIR spectra of the coating during the deposition process. Therefore, an IR-transparent KBr (potassium bromide) window is placed at the end of the tube. By placing the spectroscopy windows at the end of the tubes with a great distance to the plasma, a deposition on the windows is prevented.

These spectroscopic components were designed and built up in a previous work [51]. The optical path of the beam from the spectrometer through the Plasmodul to the detector is illustrated in Fig. 3.4. After leaving the spectrometer, the beam passes two mirrors and enters the Plasmodul through the spectroscopy tube. The second mirror is a parabolic one, which focusses the beam on the sample. After the beam reflection on the substrate, it exits the setup via the opposed tube, and the beam is directed to the detector by another two parabolic mirrors. Basic information on the FTIR spectroscopy will be given in section 3.3.1.

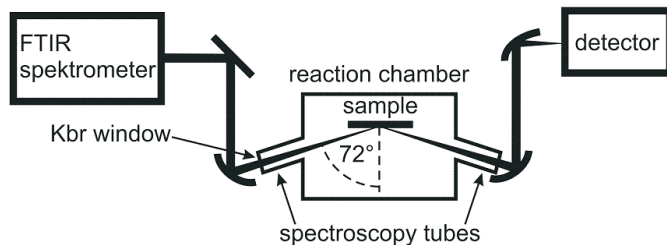


**Fig. 3.4:** Schematic pathway of the ir beam of the in-situ FTIR diagnostic in the Plasmodul, from [51].

pressure	frequency	power	temperature	gas flux
0.2 mbar	2.45 GHz	$2 \times 600$ W	$250^\circ\text{C}$	20 – 105 sccm

**Tab. 3.1:** Typical parameters of a depositing discharge in the Plasmodul.

The last module ring below the cover plate of the device contains the pumping connection, which is split into two inlets. They are installed symmetrically above the substrate holder to guarantee a homogeneous gas flow through the whole device. The pumping system consists of a rotary and a turbo molecular pump with an end pressure of about  $10^{-3}$  mbar. The pressure is controlled by a leak valve and a capacitance gauge, which are installed at this module as well. In previous works, the best pressure in the Plasmodul during the deposition process was identified to be 0.2 mbar for depositing barrier coatings [50]. An overview of the standard discharge parameters in this setup is given in Tab. 3.1 and 3.2, where the main plasma parameters in an oxygen plasma ( $m_i = 16 \cdot 10^{-27}$  kg) are specified.

position	$n_e$ [ $10^{16} \text{ m}^{-3}$ ]	$T_e$ [eV]	$\omega_{pe}$ [ $10^9 \text{ 1/s}$ ]	$\omega_{pi}$ [ $10^6 \text{ 1/s}$ ]
Plasmalines	30	3.6	30.9	193
substrate holder	0.6	0.6	3.57	22.3

**Tab. 3.2:** Typical plasma parameters of a depositing discharge in the Plasmodul.

### 3.2.2 The Duo-Plasmaline

The Duo-Plasmaline [40], which was developed at the Institut für Plasmaforschung, Universität Stuttgart, is a linearly extended low-temperature microwave plasma source, which is fed by a frequency of 2.45 GHz. The mechanisms, which lead to the maintenance of a microwave discharge, are explained in section 2.5.

A scheme of this plasma source is shown in Fig. 3.5. It consists of a quartz tube in a vacuum chamber. It is filled with atmospheric pressure. The microwave is injected from one magnetron on each side by coaxial conductors. The outer conductor ends inside the vacuum chamber such that the electric field can enter the low-pressure volume outside the quartz tube. In contrast to the atmospheric-pressure regime inside the lines, the mean-free path for the electrons in the low-pressure area outside is high enough to absorb sufficient energy from the microwave to ionize the gas particles. Consequently, a plasma ignites around the endings of the outer conductor. The plasma with density above the cutoff can be considered as an outer conductor for the electromagnetic wave, such that the microwave can propagate further in the glass tube from both sides until the plasma is closed at the middle of the tube. This is only possible, if the injected microwave power is high enough. Hence, the length of the cylindrical plasma column around the tube depends on the injected power and the pressure in the vacuum chamber.

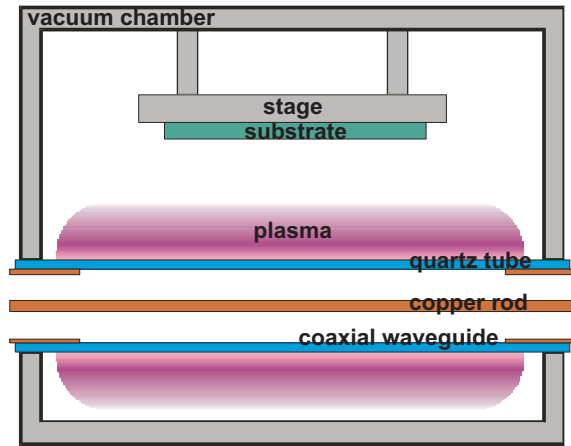


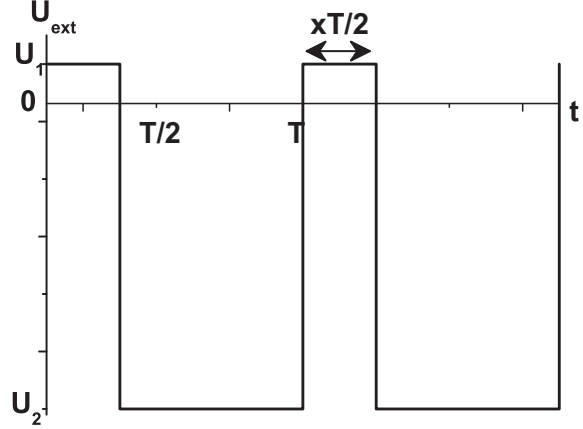
**Fig. 3.5:** Schematic illustration of the Duo-Plasmaline.

In this work, an array consisting of four parallelly arranged Duo-Plasmalines with a length of 45 cm each is used as plasma source to guarantee homogeneous plasma conditions over the whole cross section of the device. To get a uniform plasma distribution around the four lines, the power of the installed magnetrons is split up symmetrically on each side. With regard to industrial applications, the length of the Plasmaline can be enlarged up to several meters. The number of lines in an array can be adapted to the particular demand as well.

### 3.2.3 The substrate bias

The different possibilities of obtaining a bombardment of the growing film surface with high-energetic ions are discussed in detail in section 2.4 and 2.6. For the deposition of insulating  $\text{SiO}_x$  and  $\text{SiN}_y$  coatings in the context of this work, the chosen pulse form of the substrate bias is an alternating one. Hence, the charge carriers remaining on the substrate surface are neutralized during one period. To reach an optimized efficiency of the bias process, an asymmetric bipolar rectangular pulse is chosen as substrate bias. During an ideal rectangular pulse, there is no start-up and run-out phase like for a sinusoidal pulse, because the maximum value is reached instantaneously after switching the polarization. Hence, the start-up time after each change of polarization can be omitted. The asymmetry and bipolarity of the pulse both take the different ion and electron mobility in the plasma into account. The bias frequency is chosen in such a manner that it is less than the ion-plasma frequency. Thus, the ions react instantaneously to a change of the substrate bias and, therefore, the positive ions can be accelerated up to energies determined by the negative amplitude of the applied voltage. If any negative ions are available like in electronegative plasmas as oxygen plasmas, they are attracted during the positive pulse. Hence, the effect of the ion bombardment on a growing layer could be more intense in electronegative than in electropositive plasmas.

The substrate bias is generated by a rectangular pulser from MKS Instruments, Inc. [62]. It has a constant output of +37 V. The negative pulse is superimposed. Negative ions would only be accelerated by the low value of 37 V. Hence, their effect by impacting the growing layer can be neglected. The pulse can be regulated by three parameters: the voltage  $U$  (absolute averaged value of the signal), the pulse width  $p_w$  (duration of the positive pulse) and the frequency  $f$ . The amplitude of the negative pulse can be adjusted up to 500 V in steps of 0.1 V. The asymmetry of the positive and negative pulse is adjusted by the pulse width between 400 ns and 40 % of the period length of



the pulse in 1 ns steps. Hence, it is dependent on the adjusted frequency, which can be varied between 50 and 250 kHz in steps of 1 kHz. An ideal rectangular bipolar pulse is shown in Fig. 3.6. In Tab. 3.2, the electron- and ion-plasma frequency in front of the substrate holder is calculated to  $\omega_{pe} = 3.57 \text{ GHz}$  ( $f_e = 0.57 \text{ GHz}$ ) and  $\omega_{pi} = 22.3 \text{ MHz}$ , ( $f_i = 3.55 \text{ MHz}$ ), respectively. The driving bias frequency is lower

**Fig. 3.6:** Ideal asymmetric bipolar rectangular pulse with the positive voltage value  $U_1$  and the negative one  $U_2$ , as well as the pulse width of  $p_w = xT/2$ .



than the ion-plasma frequency. This case is consistent with Fig. 2.7a.

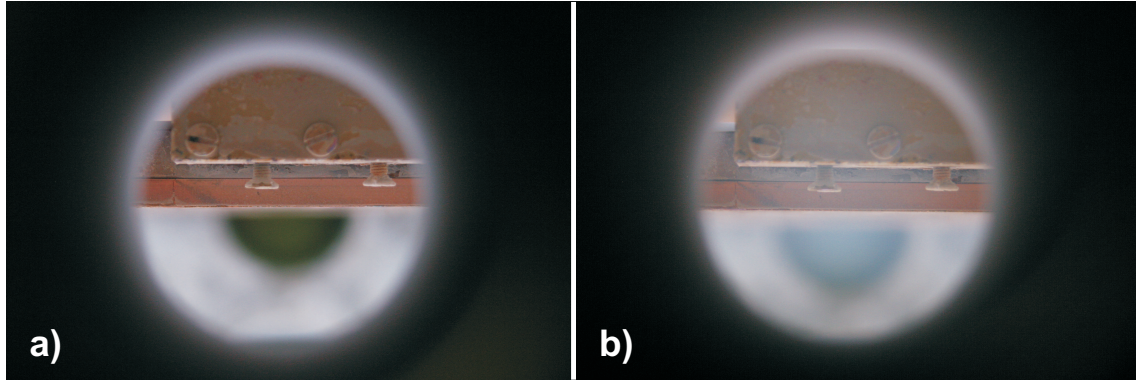


**Fig. 3.7:** Perpendicular view on the front of the substrate holder a) in the case of the microwave discharge only, b) with the additional capacitive discharge. The difference can be seen in the additional glow in front of the stage in the case of the applied bias signal.

The bias voltage is applied to the substrate holder, which represents an additional passive electrode in the microwave plasma (in the unbiased case), with respect to the grounded enclosure of the device. This leads to a generation of a capacitive plasma by the applied bias voltage, which superimposes the microwave generated plasma. This additionally ignited plasma can be observed directly in front of the substrate holder. An illustration of this process is given in Fig. 3.7. Hence, the ion flux can be regulated by the parameters of the microwave discharge, whereas the ion energy is manipulated independently by the bias parameters and therefore by the capacitive discharge. The corresponding theory is given in section 2.6.

Because of the different electrode areas and the driving frequency in the kHz range, this discharge can be described by the theory of a low-frequency asymmetric capacitive plasma of section 2.4.3 and 2.6. Consulting the calculation of the self bias carried out in section 2.4.3 for the case of a symmetric rectangular pulse, the applied asymmetric bipolar pulse can be described by

$$\begin{aligned} U_{\text{ext}} &= U_1 & \text{for} & 0 \leq t < xT/2 \\ U_{\text{ext}} &= -U_2 & \text{for} & xT/2 \leq t < T \end{aligned} \quad (3.3)$$

as analog to Eq. (2.41) with the positive value  $U_1$  and the negative one  $U_2$  (Fig. 3.6).  $x$  must be  $x \leq 0.8$  by definition because of the parameter range of the power source. The ratio of the two electrode areas  $\eta$  is about 12 (inner vacuum vessel to substrate holder). Then the dc self bias can be calculated in the same way as in Eqs. (2.43)-(2.45) to the simplified form

$$|U_{\text{bias}}| = U_1 \left\{ 1 + \frac{T_e}{eU_1} \ln \left[ 1 + \frac{x-2}{\eta x} \right] \right\}. \quad (3.4)$$

The used standard bias parameters are  $f = 250 \text{ kHz}$ ,  $U = 500 \text{ V}$  (this leads to a

negative peak value of about  $U_2 = 1500$  V) and  $p_w = 1376$  ns (which gives  $x = 0.7$ ). By inserting these values into Eq. (3.4), a dc self bias of  $|U_{\text{bias}}| = 36.8$  V is obtained. Hence, the applied bias pulse is shifted by this negative dc bias. Approximately, this is the value of the applied positive pulse.

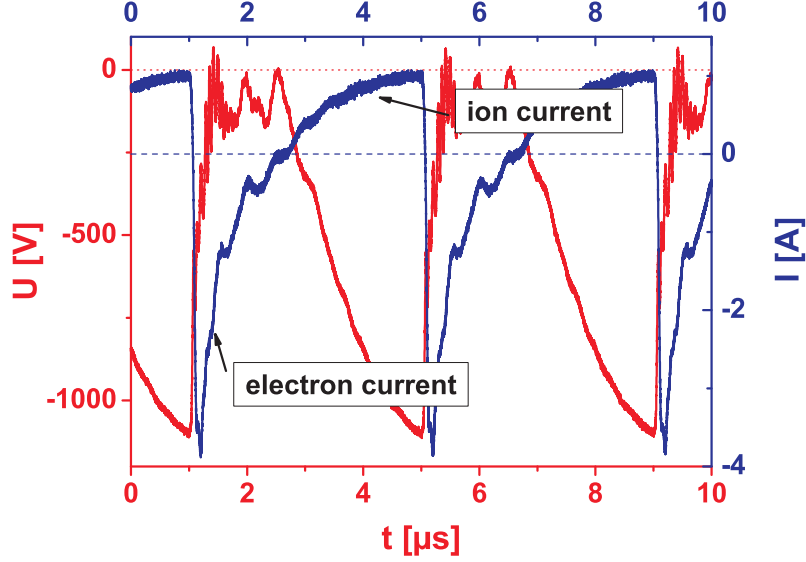


**Fig. 3.8:** Time-dependent characteristics of the current and voltage signal applied to the substrate holder.

The time dependence of the current and voltage applied to the substrate holder was measured in the supply line in front of the feedthrough outside the vacuum chamber. For measuring the voltage characteristics, a voltage divider with a ratio of 100:1 was used. The downscaled signal was transmitted to an oscilloscope. The current was measured by a clamp-on ammeter, which divides the signal by the ratio of 10:1, and transmitted to the oscilloscope as well. The characteristics for the bias parameters  $f = 250$  kHz,  $U = 300$  V and  $p_w = 1376$  ns is shown in Fig. 3.8.

The real voltage signal does not show a perfect rectangular profile. The negative pulse is of triangular shape. The whole signal is shifted by the negative dc self bias. This can be clearly seen for the positive pulse, which – without self bias – should reach +37 V as limited by the pulser. In the current characteristics, a definite difference between the electron and ion current can be observed. The electron current is characterized by a sharp peak due to the insignificant inertia of the electrons. Hence, they respond instantaneously to the applied positive voltage until the electrode surface is charged negatively. During the applied negative voltage, the substrate holder attracts the ions. The characteristics of the ion current is smoother than that of the electron current. Another peculiarity are the oscillations, which superimpose both the voltage and the current signal. According to section 2.4.1, these oscillations are related to the nonlinear resonance effect, which represents a nonlinear oscillation of the electron-sheath edge [24, 27, 28].

An estimation of the limit frequency, above which the influence of the deposited insulating film can be neglected, is given by Eq. (2.48). With the assumptions  $d = 50 \mu\text{m}$  (layer thickness on the electrode),  $T_e = 0.6 \text{ eV}$  (Tab. 3.2),  $\epsilon = 3.9$  ( $\text{SiO}_x$  coating),  $I_{i0} = 1 \text{ A}$  (Fig. 3.8) and  $U_0 = 1000 \text{ V}$ , the limit frequency is determined to  $f \approx 7 \text{ MHz}$ . This is only a very rough approximation, because Eq. (2.48) is given for a sinusoidal driving voltage. But it shows, that – in the range of the used frequencies – the deposited insulating coating on the substrate holder can influence the voltage characteristics of the applied bias. This is a possible explanation for the deformation of the rectangular pulse.

### 3.3 Diagnostics and analysis methods

In this section, three different analytical methods used in this work are introduced. The Fourier-transform infrared (FTIR) spectroscopy is a noninvasive method for analyzing the chemical composition of gases, liquids or solids. In the presented context, the chemical structure of the deposited layers is investigated by FTIR spectroscopy. Because of its noninvasive character, it is suitable for an in-situ investigation of the growing coating during the deposition. With the photospectrometer the refractive index of the coating is determined by measuring their reflectance. The plasma parameters like the electron temperature and density are measured with a double probe.

#### 3.3.1 The Fourier-transform infrared spectroscopy

The molecular composition of the deposited layers can be determined by irradiating the probe with polychromatic infrared light, typically in the range of  $\tilde{\nu} = 400 - 8000 \text{ cm}^{-1}$ , where  $\tilde{\nu}$  is the wavenumber, the inverse of the wavelength  $\lambda$ . Most of the molecule specific oscillation frequencies are in the energy range of the infrared light and their oscillations can be excited by absorbing the corresponding frequency, which is mainly determined by the two atoms of the bonding and their very next neighbors. The condition is the existence of a molecular bond with a dipole moment. By irradiating the probe with polychromatic light, the frequencies specific for the existing molecular bonds are absorbed and diluted after penetrating the investigated coating. The reduction of the intensity of the light by irradiating the probe can be described by the Lambert-Beer law:

$$I = I_0 \exp\{-\mu d\}, \quad (3.5)$$

where  $I$  is the intensity of the transmitted light,  $I_0$  the intensity of the incident light,  $\mu$  the absorption coefficient and  $d$  the layer thickness. The molecular composition of the sample can be determined by relating the absorbed frequencies to the corresponding molecular bonds.

In general, FTIR spectra can be measured in reflectance as well as in transmission. For the reflectance measurements, two methods are available: the single reflection as well as the **attenuated total reflection (ATR)** method. In this work, the presented spectra are measured in single reflection, exclusively. For using this method, the coating is deposited on a reflective substrate, e.g. a metal sheet with a plane surface or a molybdenum mirror. The IR beam penetrates the coating, is reflected at the substrate surface dependent on the variable angle of incidence and penetrates the coating a second time before it reaches the detector.

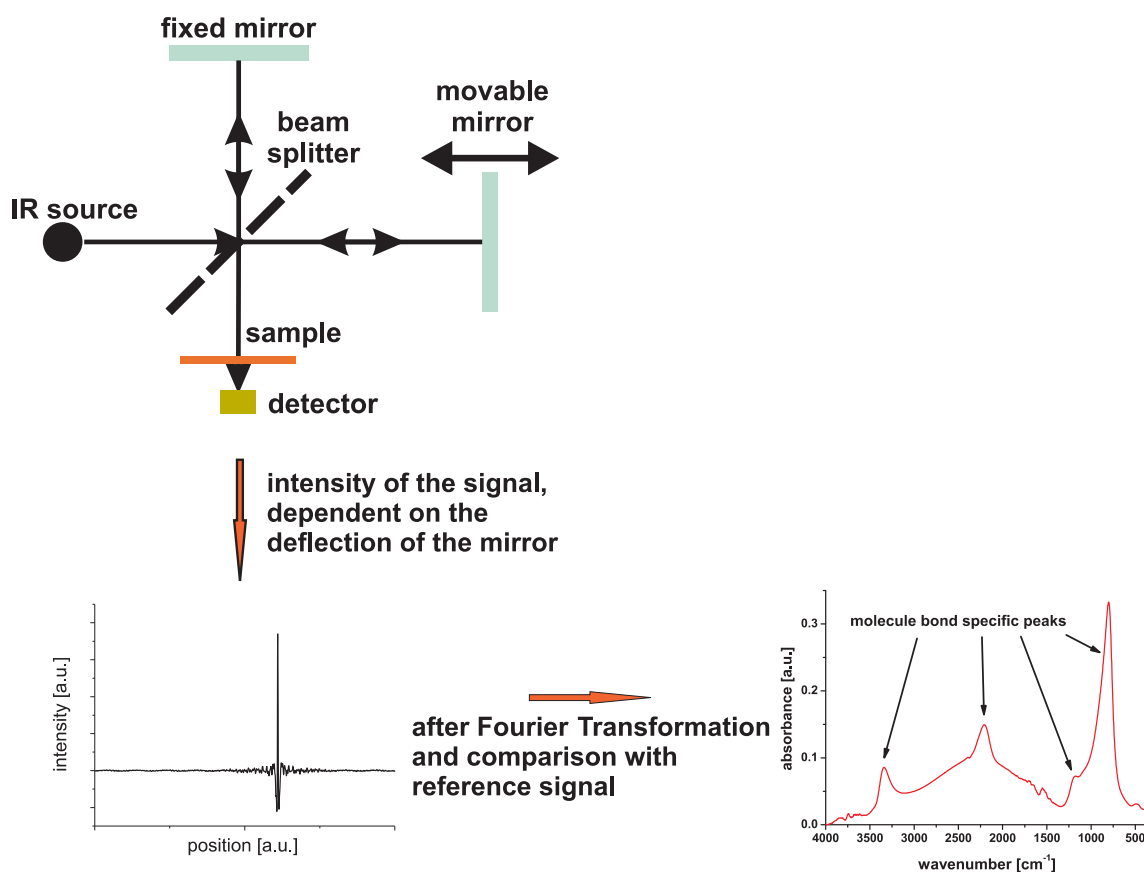


**Fig. 3.9:** Schematic of the processing of an absorption FTIR spectrum. By varying the mirror position of the Michelson interferometer in the spectrometer, an interferogram is obtained. To obtain the absorption spectrum of the investigated coating, this interferogram must be Fourier transformed and compared with the reference spectrum.

The FTIR spectrometer "Vector 22" is from Bruker Optics GmbH. The IR light is generated by a globar, which emits a spectrum nearly similar to the one of a full radiator. The advantage of a FTIR spectrometer is its high resolution as well as the good signal to noise ratio, resulting from using a Michelson interferometer instead of a dispersive element. By varying the position of one mirror of the interferometer, the detector measures an interferogram, which is recorded. Its signal strength is dependent on the displacement of the movable mirror and therefore of the optical

path difference between the two compared beams. By Fourier transforming this interferogram, the spectrum of the investigated probe is obtained. The absorption spectrum results from estimating the difference of the reference spectrum (measured without irradiating the probe) with the one of the sample. Hence, the maxima in the obtained absorption spectrum are in fact minima in the spectra of the coating. The measuring procedure is depicted in Fig. 3.9.

In the framework of Ref. [51], an in-situ FTIR spectroscopy was installed on the Plasmodul, which is illustrated in section 3.2. This method allows monitoring the chemical composition of the layer right during the deposition process by an externally installed detector, in contrast to the ex-situ measurement, which gives information about the total layer after the deposition and is measured with the detector installed inside the spectrometer. To get the opportunity of switching between the external and the internal detector, a pivoted mirror was implemented in the optical path of the spectrometer. The internal detector is a DTSG (deuterium-terminated triglycinsulfide) detector. To overcome higher intensity losses during the in-situ measurements resulting from the deflection mirrors and the KBr windows installed on the Plasmodul, the used MCT (mercury cadmium telluride) detector has a higher sensitivity. The adaption of this in-situ diagnostic at the Plasmodul is described in detail in section 3.2.1.

### 3.3.2 The photospectrometer

To determine the refractive index of the deposited layers, the photospectrometer Hyper UV-3101PC from Shimadzu is used, which is a specular reflectance attachment. This is done by analyzing the interferogram of the coatings and identify the refractive index out of the wavelengths of the maxima and minima of the interferences.

The light beam for measuring the reflectance of a probe is generated by a deuterium lamp, which covers a range of 190 – 300 nm, or by a halogen bulb, which supplies wavelengths up to 3200 nm. The light beam passes through two grading monochromators, whereof each consists of three separate concave grids, each one covering a distinct wavelength range. After this, the beam is split into two similar parts by a semi-permeable mirror. One is directed to the sample through a 5 mm or alternatively through a 15 mm mask, the other one is the reference beam and is reflected at an aluminum mirror. Both beams have an angle of incidence of  $5^\circ$ . After striking the reflective sample, both beams are superimposed and detected by a photomultiplier or a PbS cell in the infrared range. The result is an interferogram like that one shown in Fig. 3.10a, which results from the optical path difference of the two beams.

In order to determine the refractive index of the investigated layer, the order of the discrete maxima and minima have to be calculated by the condition for constructive and destructive interferences:

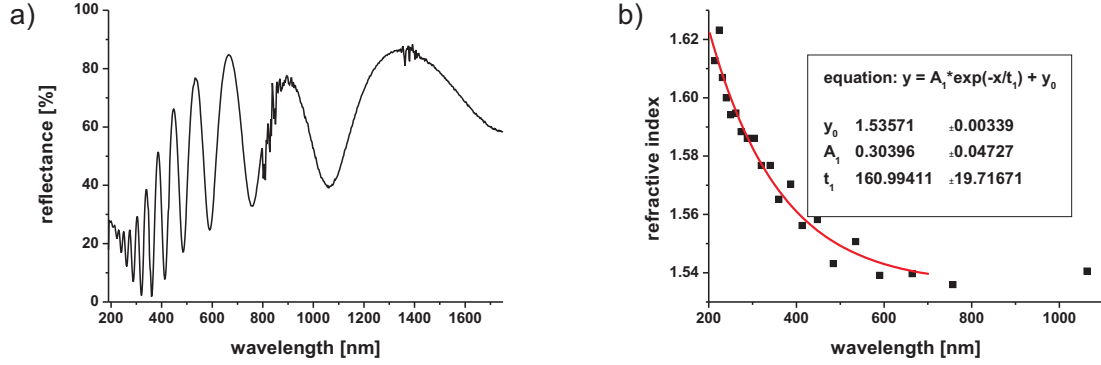


**Fig. 3.10:** Determination of the refractive index of the deposited layers: a) interferogram obtained from the photospectrometer, b) refractive index depending on the wavelength, obtained from the interference maxima and minima of the interferogram.

$$\begin{aligned}
 2d\sqrt{N^2 - \sin^2 \alpha} &= j\lambda_j && \text{constructive interference} \\
 2d\sqrt{N^2 - \sin^2 \alpha} &= \frac{2j+1}{2}\lambda_j && \text{destructive interference,} \quad (3.6)
 \end{aligned}$$

where  $d$  is the layer thickness,  $N$  the refractive index,  $\alpha$  the angle of incidence,  $j$  the order and  $\lambda_j$  the wavelength of the corresponding maximum or minimum. For the present case with  $\alpha = 5^\circ$ , the equations can be simplified by the assumption of  $\sin \alpha \approx 0$ . The following considerations are carried out for constructive interferences, the calculation for the destructive interferences are similar. The associated order of the constructive interference can be obtained by two adjacent maxima. The refractive index corresponding to the wavelength of this maximum is

$$N = \frac{j \cdot \lambda_j}{2d}. \quad (3.7)$$

The layer thickness is measured separately with a Perthometer C5D (details on this method can be found in Ref. [63]). The refractive index shows an exponential decay with increasing wavelength, which is shown exemplarily in Fig. 3.10b. In literature, the refractive index is given with respect to a wavelength of 589 nm. This can be determined by fitting  $N = A \exp\{-\lambda/(t_1)\} + y_0$  to the data.

### 3.3.3 Langmuir double-probe measurements

Probe measurements are a common diagnostic method in low-temperature plasmas ( $T_e < 100$  eV). In contrast to single Langmuir probes [13], which are utilized in plasmas with a good contact to a grounded electrode being the reference point for

the probe measurements, double probes [64] can be used in the case of plasmas without any reference point of the potential or in plasmas with time-dependent conditions, since they constitute a floating setup.

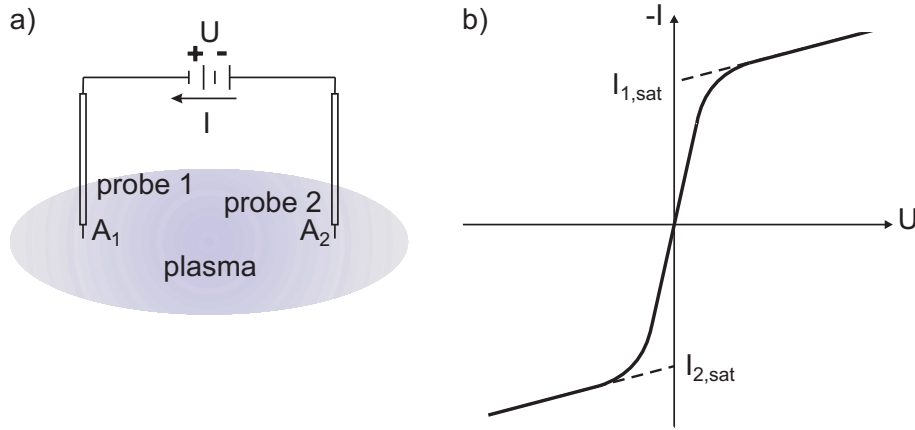


**Fig. 3.11:** a) Schematic of a floating double-probe system showing the electrical circuit of the two probes and the plasma, b) current-voltage characteristics of an ideal Langmuir double probe ( $I_{1,sat} = I_{2,sat}$ ).

Ideally, a double probe consists of two identical probes, in the simplest case composed of a tungsten wire insulated by a ceramic tube, such that only the tip of the wire is in electrical contact with the plasma. The two probes are located in the plasma in such a way that they are not disturbing each other (the spacing between them has to be greater than several Debye lengths), but the distance between them must be small enough to guarantee identical plasma conditions at each probe. By applying a voltage between the probes, a current flows through the electrical circuit consisting of the two probes and the plasma. This process is depicted in Fig. 3.11a. The current is positive in the case of a positive voltage by definition. By sweeping the applied voltage, a current-voltage characteristics is obtained, which is shown schematically in Fig. 3.11b. Here, the saturation currents of both probes are equal,  $I_{1,sat} = I_{2,sat}$ , and the characteristics is totally symmetric. This is the case of an ideal double probe. For  $U = 0$ , both electrodes are at the same potential (floating potential), consequently the net current is zero. By lowering the applied voltage, a net current flows from probe 2 to probe 1. This is a symmetric process for both probes. The flowing net current is given by [65]:

$$I_j = I_{j,sat} \cdot \tanh \left\{ \frac{eU}{2T_e} \right\}, \quad (3.8)$$

with the indicators  $j = 1, 2$  of the two probes and the applied voltage  $U$ .

In practice, the two probe tips never have completely the same surface area and, consequently, the ion-saturation currents  $I_{1,sat}$  and  $I_{2,sat}$  are not equal. With



different probe-surface areas ( $A_1 \neq A_2$ ), Eq. (3.8) can be transformed into [65]

$$\left| \frac{dI}{dU} \right|_{U=0} = \frac{e}{T_e} \frac{I_{1,\text{sat}} \cdot I_{2,\text{sat}}}{I_{1,\text{sat}} + I_{2,\text{sat}}}. \quad (3.9)$$

Thus, the electron temperature can be obtained by determining the derivative of the I-U characteristics at  $U = 0$ .

The electron density  $n_e$  is calculated by

$$I_{j,\text{sat}} = 0.61en_eA\sqrt{\frac{T_e}{m_i}} \quad (3.10)$$

with the ion mass  $m_i$  and the probe-surface area  $A$  similarly to the determination from single Langmuir probes [13]. In the case of different probe-surface areas the density is obtained by averaging the two densities determined from the two ion-saturation currents  $I_{1,\text{sat}}$  and  $I_{2,\text{sat}}$ .

The double probe was installed vertically on the top plate of the Plasmodul. The probe carrier was attached to a DIN ISO KF-40 flange, the probe itself was inserted in the vacuum chamber through a squeeze feedthrough, such that the position of the probe could be varied via a guiding rod. A picture of the installed probe is shown in Fig. 3.12.

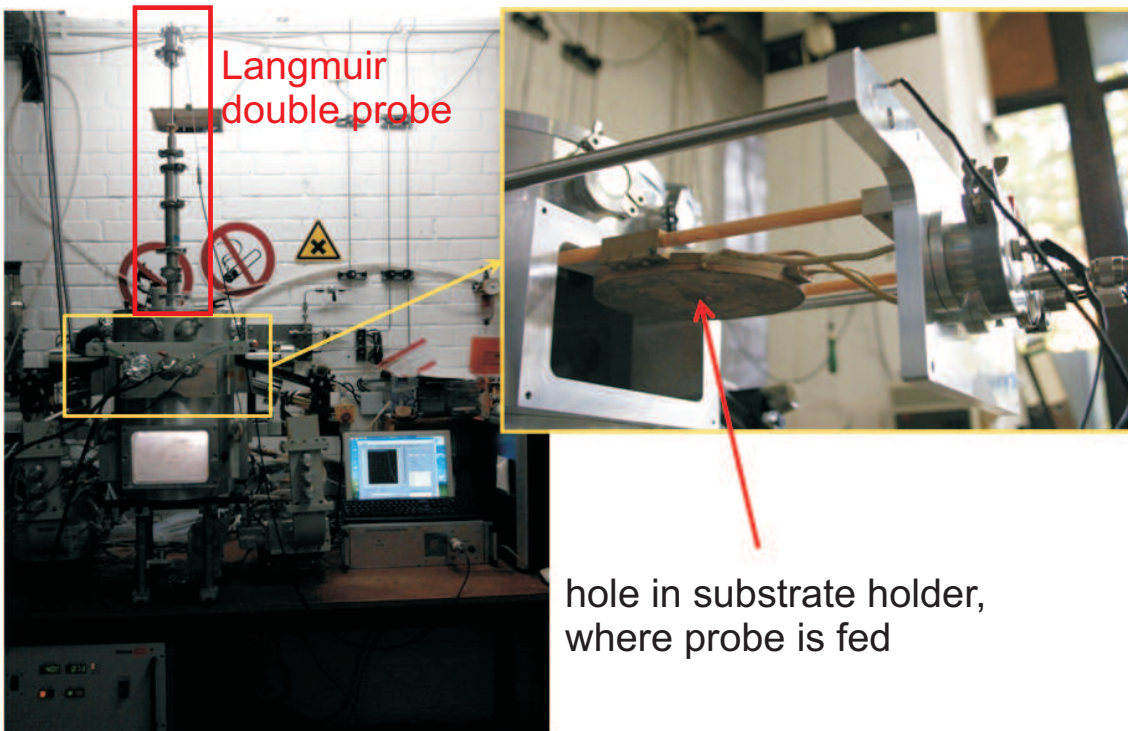


**Fig. 3.12:** Picture of the Langmuir-probe attachment on the Plasmodul (left) and feedthrough in the substrate holder (right).



In order to carry out measurements in the region between the plasmaline array and the substrate holder, the double probe was fed through a hole in the middle of the substrate holder. This way, radial measurements of the plasma parameters perpendicular to the plasmaline array were accomplished.

### 3.4 Measurements of plasma parameters

To identify the input parameters of the simulation code, that will be used in chapter 5 for the determination of the particular layer-growth processes induced by the ion bombardment on the substrate, an exact information of the plasma parameters – especially the electron density and the electron temperature – is needed. For this purpose, double-probe measurements were carried out inside the Plasmodul in the region between the plasmaline array and the substrate holder. Thus, position-dependent characteristics of the electron density and temperature can be obtained. Special attention is paid to the influence of the additional capacitive discharge, which superimposes the microwave plasma, on the plasma parameters. These measurements were done with a double probe instead of a single Langmuir probe, because the plasma in the Plasmodul has only poor contact to the vessel wall due to the insulating layer deposited in the whole device. Hence, probe measurements, which are independent of a defined ground point, were needed. The theory of Langmuir double probes and the installation of the probe at the Plasmodul was introduced in section 3.3.3. Because of the vertical orientation of the probe, the position-dependent characteristics of the measured plasma parameters are in radial direction relative to the plasmalines and vertically to the plasmaline array.

To avoid a deposition of the probe tip, the measurements had to be done in a non-reactive plasma. For this reason, the results presented here were obtained in a pure nitrogen plasma. The discharge parameters were chosen to be the same as in the deposition process used in this work: a pressure of  $p = 0.2$  mbar, nitrogen-gas flux of  $\phi = 105$  sccm and a microwave power of  $2 \times 600$  W. The bias voltage was varied up to 500 V at constant parameters of  $f = 250$  kHz and  $p_w = 35\%$ .

The distance between the substrate holder and the plasmalines is 20 cm (see section 3.2.1). To obtain a position-dependent characteristics of the electron density and temperature in this plasma region, the measurements were carried out in 2 cm steps. An overview of the I-U characteristics at each position with a substrate-bias voltage of 100 V is given in Fig. 3.13. In these measurements, the probe was biased in the range of  $-70$  to  $70$  V. All of the characteristics are smooth and symmetric. Hence, they seem to be unaffected by the alternating driving frequency of the superimposed capacitive discharge. Consequently, these measurements are qualified to determine the plasma parameters.

Quantitative analyses of the electron density will be given in section 3.4.1, followed by the determination of the electron temperature profile. At the end, a short conclusion will be given in section 3.4.3.

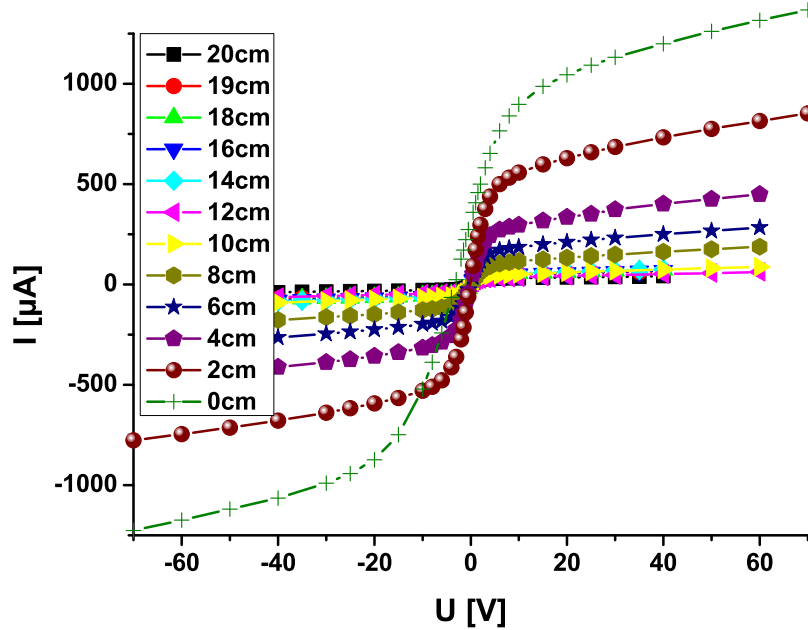


**Fig. 3.13:** Overview of the position-dependent I-U characteristics of the double probe. No influence of the applied time-varying substrate bias voltage can be observed.

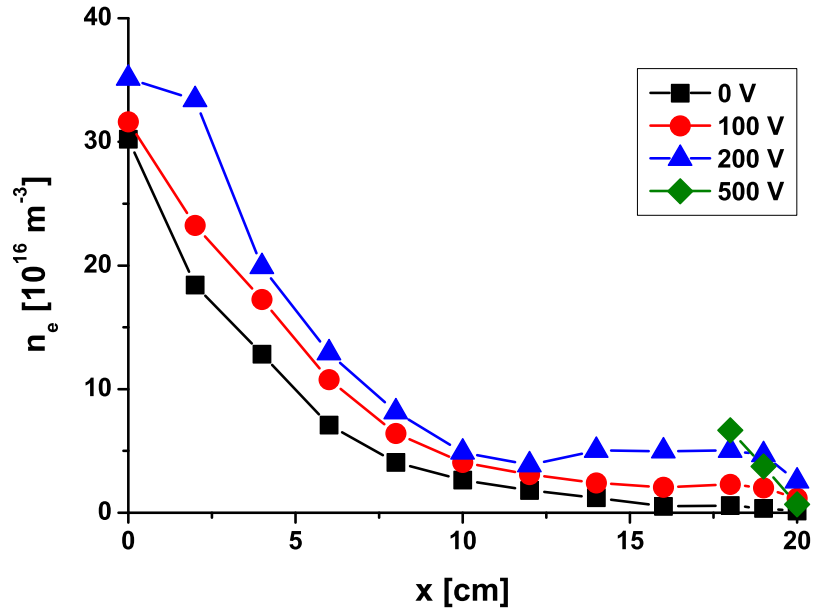
### 3.4.1 Electron-density characteristics

Figure 3.14 shows the electron density in the region between the microwave plasma source and the substrate holder of the Plasmod. For all three profiles with a capacitive driving voltage of 0 V, 100 V and 200 V, a similar decrease from the plasmalines at the position  $x = 0$  cm to the substrate holder at  $x = 20$  cm is observed. Additionally, a slight increase of the density with increasing bias voltage is obtained.

Without substrate bias, the electron density at  $x = 0$  cm is  $n_e = 3 \cdot 10^{17} \text{ m}^{-3}$ . It decreases to approximately  $6 \cdot 10^{15} \text{ m}^{-3}$  in front of the substrate holder at  $x = 18$  cm. Hence, the density drops by about two orders of magnitude. This reduction is due to the higher recombination rate of the electrons and ions at increasing distance to the plasma, i.e. the energy source. By superimposing the capacitive discharge, a slight increase of the whole density profile is observed. An overview of the electron

driving voltage [V]	$n_e [10^{16} \text{ m}^{-3}]$ at $x = 0$ cm	$n_e [10^{16} \text{ m}^{-3}]$ at $x = 18$ cm
0	30	0.6
100	32	2.3
200	35	5.0

**Tab. 3.3:** Overview of the electron densities at the position of the plasma source ( $x = 0$  cm) and in front of the substrate holder ( $x = 18$  cm) at different bias voltages.



**Fig. 3.14:** Position-dependent electron-density characteristics in the region between the microwave plasma source at  $x = 0$  cm and the substrate holder at  $x = 20$  cm. The probe measurements were done without any additional capacitive discharge (0 V) and with a voltage of 100 V, 200 V and 500 V.

density  $n_e$  at  $x = 0$  cm – the position of the microwave plasma source – and at a position 2 cm in front of the substrate holder at  $x = 18$  cm is given in Tab. 3.3 for all three analyzed capacitive driving voltages. The increase of the electron density with increasing bias is due to the higher power fed into the plasma, which results in a higher dissociation rate and thus in a higher charge carrier density. The higher power input seems to affect the plasma in the whole volume.

An additional effect is the abrupt decrease of the density in front of the substrate holder (from  $x = 18$  cm to  $x = 20$  cm). It may be possible that the plasma sheath, which is developed at each negative pulse of the applied alternating bias voltage, with its strong decrease of the electron density towards the point of the electrode influences the measurements. The extension of the plasma sheath is in the range of 0.5 cm, obtained by inserting  $n_e = 5 \cdot 10^{16} \text{ m}^{-3}$ ,  $T_e = 0.7 \text{ eV}$  and  $U = 200 \text{ V}$  into Eq. (2.20). The presheath is extended in the range of 1 – 3 cm. Hence, a detection of the slight density decay in the presheath would be possible. To confirm this hypothesis, the density was measured with an applied bias voltage of 500 V in front of the substrate holder. It clearly shows a sharp decay. Because of the influence of the presheath, the valid plasma parameters in front of the substrate holder are taken to be those at  $x = 18$  cm, which are similar for the bias of 200 and 500 V.

### 3.4.2 Electron-temperature characteristics

The position-dependent electron-temperature characteristics, which corresponds to the electron density of section 3.4.1, is depicted in Fig. 3.15. In the pure microwave discharge, the electron temperature decreases from  $T_e = 3.6$  eV at the position of the plasmalines to 0.6 eV at  $x = 18$  cm. The profiles of the electron temperature with the capacitive discharge superimposed are similar to the one measured without a voltage applied. An overview of the temperature values at  $x = 0$  and  $x = 18$  cm is given in Tab. 3.4.

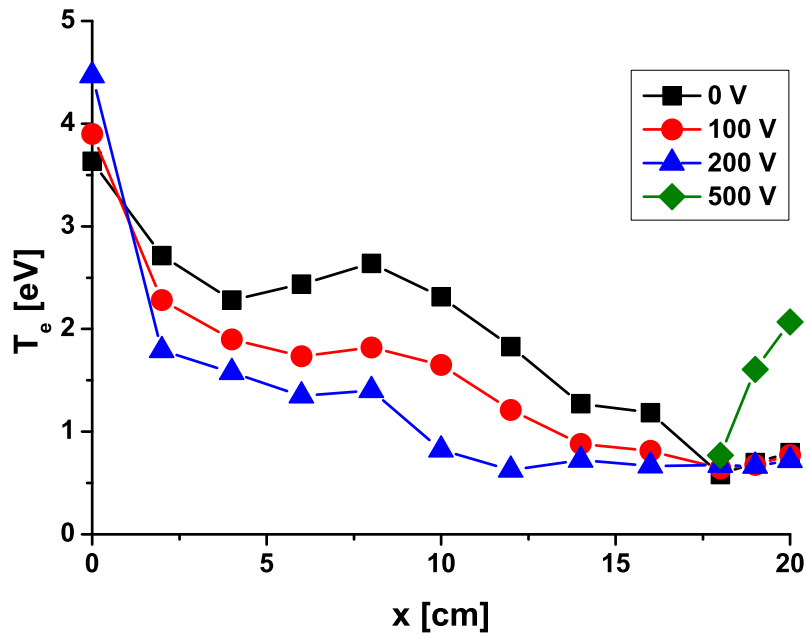


**Fig. 3.15:** Electron-temperature profiles in the region between the microwave plasma source and the substrate holder. They were measured for different driving voltages (0, 100, 200 and 500 V) of the superimposed capacitive discharge.

driving voltage [V]	$T_e$ [eV] at $x = 0$ cm	$T_e$ [eV] at $x = 18$ cm
0	3.6	0.6
100	3.9	0.6
200	4.5	0.7

**Tab. 3.4:** Overview of the electron temperatures at the position of the plasma source ( $x = 0$  cm) and in front of the substrate holder ( $x = 18$  cm) at different bias voltages.

A clear decrease of the whole characteristics with increasing bias is observed. With increasing density at higher driving voltages (section 3.4.1), the electron-

collision frequency increases and therewith the ionization rate. Thus, the electrons give off their absorbed energy faster. This process leads to a lower electron temperature.

Similar to the electron density in Fig. 3.14, a possible influence of the plasma presheath is observed in the temperature profiles. This is indicated by the slight increase of the temperature in front of the substrate holder at about  $x = 18$  cm, when a bias voltage of 100 and 200 V is applied. The electron temperature measured at 500 V confirms this trend. It increases from  $T_e = 0.95$  eV at  $x = 18$  cm to 2.1 eV at the substrate holder. Due to the alternating voltage applied at this electrode, the electrons are strongly attracted at each positive cycle. On average, this could lead to an increase in  $T_e$ .

### 3.4.3 Conclusion

Electron-density and temperature profiles were measured with a Langmuir double probe in a nitrogen plasma. As expected, they decay strongly from the microwave plasma source to the substrate holder. By superimposing a capacitive discharge, the density in the whole observation volume increases with increasing driving voltage. The decrease in the temperature in this region is consistent with the density increase. The measured electron density values are about  $n_e = 3 \cdot 10^{17} \text{ m}^{-3}$  at the position of the plasmaline array and  $n_e = 6 \cdot 10^{15} \text{ m}^{-3}$  in front of the substrate holder. The corresponding electron temperatures are  $T_e \approx 3.6$  eV and  $T_e \approx 0.6$  eV, respectively.

A very interesting point is the region close to the substrate holder: Here, the influence of the presheath could possibly be reflected in a reduced density and an increased temperature due to the slight potential drop in the presheath. This is observed in the region of 2 cm in front of the substrate holder.



## Chapter 4

# Influence of high-energetic ions on the growth of barrier coatings

This chapter is dedicated to tests of the applicability of thin metal foils (RPG steel [66]) as an alternative flexible substrate material for the fabrication of thin-film CIGS solar cells [1, 2]. If any metal is used as substrate material, an additional layer has to be applied to guarantee a diffusion preventing and insulating barrier between the substrate and the solar cells. It prohibits the diffusion of undesired substrate elements into the CIGS material, which can reduce the efficiency of the solar cells, and a short-circuit between the separate cells of a solar module [67]. In this work, these barrier layers, consisting of silicon oxide ( $\text{SiO}_x$ ) or silicon nitride ( $\text{SiN}_y$ ), are deposited in a microwave-PECVD process. The layer requirements are obvious: They must prevent diffusion, have to be insulating and they have to offer a homogeneous smooth surface.

The non-polished surface of the substrate has scratches and flakes in the  $\mu\text{m}$  scale. This is shown in Fig. 4.1a. It is well known from literature that such a substrate surface structure is replicated on the surface of the deposited coating fabricated in a PECVD process with a thickness of a few  $\mu\text{m}$  [5, 6]. Hence, a homogeneous smooth surface cannot be obtained, which is seen in Fig. 4.1b. As well, voids can develop in the deposited film at positions of notches on the substrate surface [7, 8], so that the barrier property of the coating is lost. To counteract the development of pinholes in the barrier layer, the layer growth is affected by a substrate bias, which induces an impinge of high-energetic ions. The analyses of the influence of the ion bombardment on the layer profile on rough surfaces is the topic of this chapter.

The formation of such pinholes have to be analyzed on the basis of substrates with a well-defined rough surface structure to guarantee comparable conditions. For this purpose, silicon wafers with a trench structure in the  $\mu\text{m}$  range are chosen as model substrates. Related analyses were done in previous works in the context of the semiconductor industry, mainly in the 1990's, to determine the step coverage of electric circuits with an insulating or passivation layer [8, 68, 47, 69]. There, the precursor used for the deposition of silicon oxide is often TEOS (tetraethoxysilane)

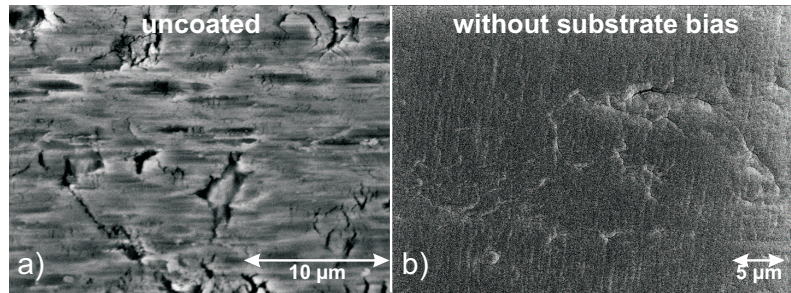


**Fig. 4.1:** a) Surface of an uncoated rough steel substrate, on which thin-film solar cells are planned to be fabricated. b) Surface of a substrate, which was coated in a microwave-PECVD process. The surface structure of the substrate is replicated on the film surface.

in combination with oxygen or ozone. The layer-forming particles in a TEOS plasma have a high surface mobility and, hence, they offer a long surface diffusion before forming  $\text{SiO}_x$  [41, 70], so that a widely homogeneous coating can be achieved [47, 68]. For the deposition of silicon nitride, the standard precursor is monosilane in combination with ammonia as also used in this work (section 3.1.1). Monosilane is well-known for the high surface mobility of its layer forming radicals [71].

The considered trench dimensions in these publications are of the same order of magnitude as those investigated in this chapter, namely a few  $\mu\text{m}$  in height and width. The devices used in previous experiments include a wide spectrum of plasma generation: Most of them are parallel-plate reactors with a driving frequency in the MHz range [8, 47]. In these deposition processes, the ion bombardment of the substrate surface is caused only by the self bias (the corresponding theory is described in section 2.4.1 and 2.6). In other works, an additional substrate bias in the kHz range is applied to regulate the ion bombardment independently of the self bias [48]. Besides coatings, which are deposited by a sputter process [72], the microwave plasma process plays an essential role in the coating of cavities. These plasmas are widely spread because of their comparably high ion density, so that the layer growth can be highly influenced by ion bombardment with an additional substrate bias [41, 68]. The theory of this mechanism was introduced in section 2.6.

In this work, a microwave plasma process in combination with a superimposed capacitive discharge driven with a frequency in the kHz range is used for the deposition of the barrier layers. In this process, the advantages of both discharges are united: The high dissociation rate and, therefore, high deposition rate of a microwave plasma and the direct influence of the kHz-driving frequency on the ion motion, which – compared to a substrate bias in the MHz range [41] – results in a higher energy of ions impinging on the substrate surface.

HMDSO in combination with oxygen was chosen as precursor for the deposition of the silicon oxide, because in previous works very good results for the barrier properties of these layers were obtained [50, 51]. The aim here is to overcome the well-known low surface mobility [73] by the additional energy from the ion



bombardment. For the deposition of silicon nitride, monosilane is used as precursor. Its surface mobility is known to be much higher than the one of HMDSO. Therefore, a more conformal coverage of the  $\text{SiN}_y$  film on a step is expected.

At the beginning of this chapter, the model substrates, which are used for the characterization of the achieved step coverage, will be introduced. A simple layer-growth model, which describes the resultant coated step profiles, is given in section 4.1. In section 4.2, the distinct influence of the bias parameters is analyzed and standard parameters for further investigations are determined. The coating profiles at the positions of the trenches will be compared in section 4.3 for an unbiased and a biased deposition. In particular, an application oriented analysis of barrier-film depositions on flexible steel is carried out. Section 4.4 is dedicated to the analyses of insulation properties. A short conclusion of this chapter is given in section 4.5.

## 4.1 The layer-growth model

To guarantee comparable preconditions for the coatings deposited at various bias parameters, substrates with a well-defined surface structure are needed. For this purpose, silicon wafers with a trench structure in the  $\mu\text{m}$  range (which is up to the surface-defect dimensions on steel foils) are used as model substrates. Their great advantage is the offering of all relevant surface dimensions on one wafer. They will also be utilized in chapter 5 to analyze the layer-growth mechanisms by simulations.

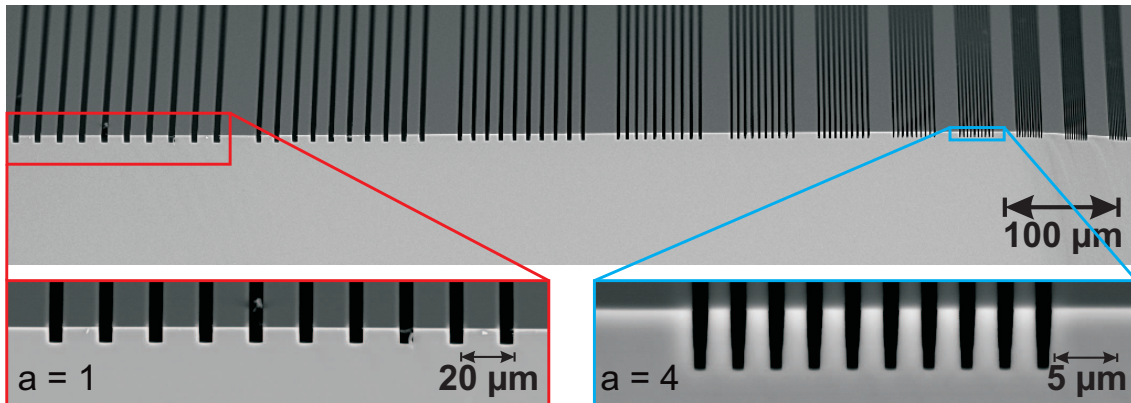


**Fig. 4.2:** View of the breaking edge of a silicon wafer with a well-defined surface structure in the  $\mu\text{m}$  range. The wafers are used as model substrates for analyzing the layer growth on rough substrate surfaces.

The width  $w$  of the trenches varies from  $0.6$  to  $4.4 \mu\text{m}$ , their height  $h$  is almost constant with a value of  $3$  to  $4 \mu\text{m}$ . Hence, the aspect ratio  $a = h/w$  covers a range from  $1$  to  $5$ . The aspect ratio is the most relevant parameter, which influences the layer growth on these trenches. For the interpretation of the coated wafers, their breaking edge (which is very easy to prepare alongside the lattice planes of these wafers) is analyzed in a scanning electron microscope (SEM). Hence, the layer

deposition inside the cavities can be investigated. The breaking edge of an uncoated substrate is shown in Fig. 4.2. The analyses will be done on the basis of the widest trench with an aspect ratio of  $a \approx 1$  (representing a wide indentation) and one with  $a \approx 4$  (representing a small cavity).

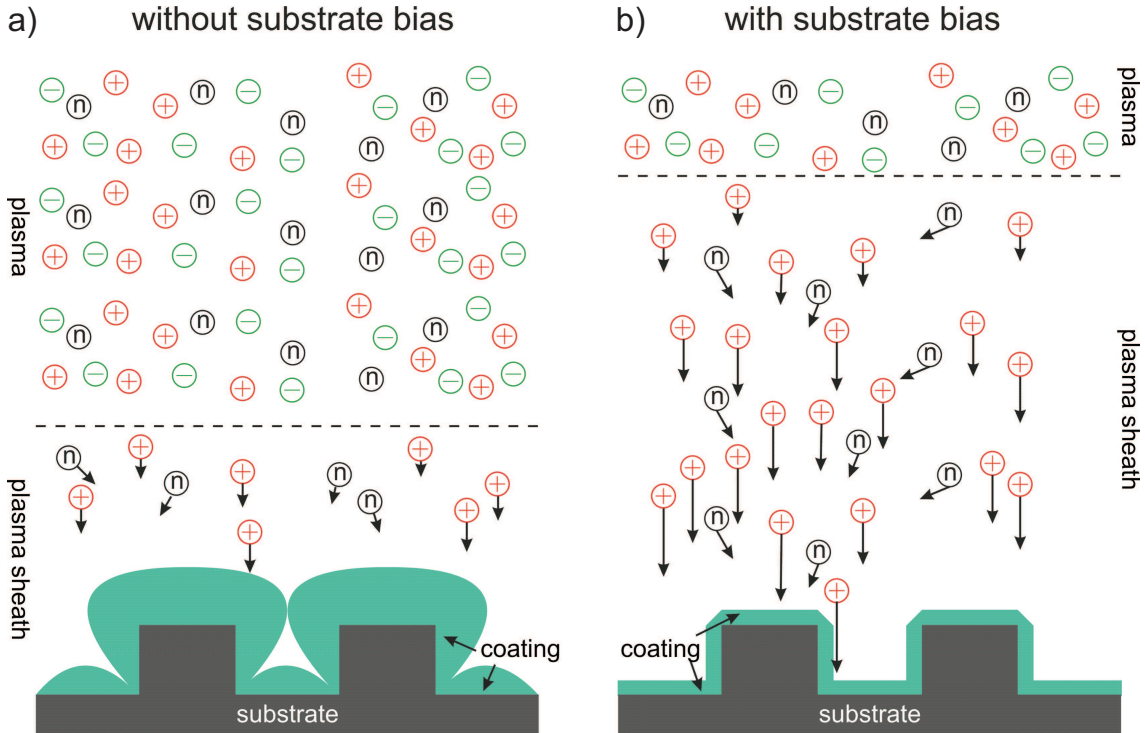


**Fig. 4.3:** Illustration of the popular model [74] to describe the layer growth on a cavity in the substrate surface in a PECVD-microwave process a) without any substrate bias, b) with an applied substrate bias.

Figure 4.3 shows the qualitative difference of the shape of the coating deposited without (Fig. 4.3a) and with (Fig. 4.3b) substrate bias at the position of a trench. Without a substrate bias, the layer forming radicals as well as the ions impinge non-directional on the substrate surface. Furthermore, both species have thermal energy. In a microwave plasma, the plasma sheath is insignificantly small, since almost no accelerating potential exists in front of the substrate (see section 2.5). The growing film shows the shape depicted in Fig. 4.3a as a consequence of screening effects of the substrate geometry as well as the self-shadowing induced by the growing layer [75]. The coating is formed ball-shaped over the enhancements on the substrate surface. Hence, the layer is closed over the cavity and a void is developed. It is obvious, that the barrier property is not guaranteed at this position, because the film is not melted over the cavity and a crack is developed in the growing layer. Through this defect, particles can diffuse or an electrical breakdown can occur.

By applying a substrate bias, the plasma-sheath region in front of the substrate is extended and the potential drop leads to an acceleration of the ions perpendicular

to the substrate surface (section 2.3). The uncharged radicals are unaffected by the bias voltage. Due to the application of energy on the layer surface by the impinge of energetic ions, the surface mobility of all layer forming particles is increased. This is consistent with a "quasi-fusion" of the film surface, which leads to a more homogeneous distribution of the particles on the substrate geometry due to their rearrangement. Due to the impinge of high-energetic ions, already bonded particles can be relocated on the layer surface, existing chemical bonds can be cracked and replaced by new (higher energetic) ones. Hence, a change in the molecular composition of the coating is possible. This will be studied in chapter 6. An additional effect of the high-energetic ions is a sputtering of the already deposited film. This sputtering can smooth out the layer shoulders above the cavity. The result is a retardation of the film closure. Hence, the absolute layer thickness inside the indentation is increased compared to the unbiased coating. In the ideal case, a uniform filling of the cavity is achieved. This is depicted in Fig. 4.3b.

An increase of the substrate temperature can increase the surface mobility as well [75] and, therefore, have a similar effect on the layer profile as the substrate bias. As mentioned in section 3.2.1, the substrate temperature varies during the deposition with an applied substrate bias. For this reason, unbiased coatings deposited at a substrate temperature of 250 and 400 °C were compared. Their profiles at the position of the trenches did not show a clear difference. Hence, all following worked out differences of the layer profiles with and without substrate bias result from the ion bombardment and not from the additional heating of the substrate.

The combination of a deposition and a sputter process for obtaining a uniform layer growth on rough surfaces was carried out in Ref. [76]. In that work, the deposition and etch cycles were operated in turn, because they were carried out in different devices. Here, both processes take place simultaneously.

## 4.2 Influence of the bias parameters

In order to analyze the influence of the three particular bias parameters (frequency, voltage and pulse width) on the layer growth, a specific value, which characterizes the particular film shape, must be introduced. Hereby, the optimized bias parameters for the best coating of the cavity can be determined. For this purpose, two values are defined: the relative layer thickness  $\Delta$  and the relative coating of the flanks  $\Phi$ :

$$\Delta = \frac{b}{d} \quad \text{and} \quad \Phi = \frac{f_b}{f_t}. \quad (4.1)$$

$d$  is the absolute layer thickness at the top of the trench,  $b$  the film thickness at the bottom of the trench,  $f_t$  and  $f_b$  are the thicknesses of the coating at the top and the bottom of the flanks. These values are illustrated in Fig. 4.4. For a homogeneous coating inside the trench  $\Delta = \Phi = 1$ , i.e. the layer thickness is equal at each position of the substrate surface. Similar definitions can be found in Ref. [75].

The dependence of  $\Delta$  and  $\Phi$  on the three bias parameters is depicted in Fig. 4.5 separately for the  $\text{SiO}_x$  and  $\text{SiN}_y$  layers. The dependence on each bias parameter is analyzed by keeping the two others constant. Only fully open cavities are taken into account (aspect ratio  $a = 1$ ) to guarantee an unaltered result of the layer thickness inside the cavity.

The dependence of  $\Delta$  and  $\Phi$  on the bias frequency is illustrated in Fig. 4.5a. The unbiased coating is depicted as  $f = 0$  kHz. An increase of these parameters and, therefore, of the filling of the trench is observed with increasing bias frequency. This is explainable by comparing the ion-plasma frequency in an oxygen plasma  $\omega_{\text{pi}} = 22.3$  MHz (see Tab. 3.2) with the bias-driving frequency:  $\omega_{\text{pi}}$  is quite higher than the applied bias frequency and, hence, the ions follow the applied external electric field. Therefore, the higher the applied frequency the more ions impinge on the substrate. Thus, a higher efficiency of the ion bombardment is achieved.

Furthermore, the values of  $\Delta$  and  $\Phi$  increase with increasing bias voltage (Fig. 4.5b). The higher the voltage amplitude, the higher is the energy of the impinging ions. Hence, the sputter yield increases with increasing bias voltage and the closure of the layer over the indentations is retarded. Therefore, the layer-forming particles have the opportunity to enter the cavity.

The dependence of  $\Delta$  and  $\Phi$  on the pulse width is shown in Fig. 4.5c. Here, a clear influence of this parameter cannot be seen. This could be explained by the characteristics of the established self bias at the substrate holder (see Eq. (3.4)) in dependence of the pulse width. It is depicted in Fig. 4.6 with  $U_1 = 37$  V,  $T_e = 2$  eV (from section 3.4.2),  $\eta = 12.17$  and  $x = 0.7$ . The self bias increases abruptly at very low pulse width and remains almost constant in the investigated range of 15 to 35%. Consequently, this parameter does not suggest any influence on the filling of the trenches.

In conclusion, the most homogeneous  $\text{SiO}_x$  as well as  $\text{SiN}_y$  films are achieved

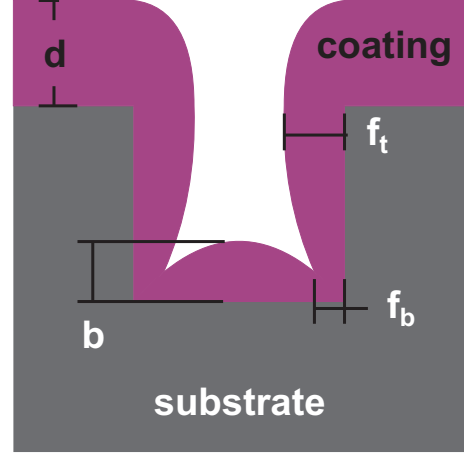


**Fig. 4.4:** Definition of the values  $d$ ,  $b$ ,  $f_t$  and  $f_b$  for the characterization of the coating by the dimensionless parameters  $\Delta$  and  $\Phi$ .

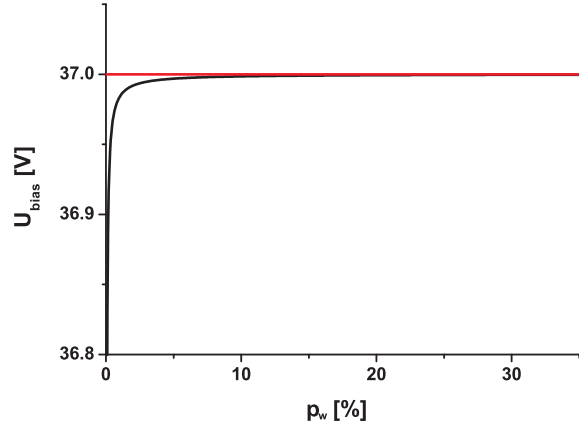


**Fig. 4.6:** Characteristics of the self bias  $U_{\text{bias}}$  in dependence of the pulse width  $p_w$ .

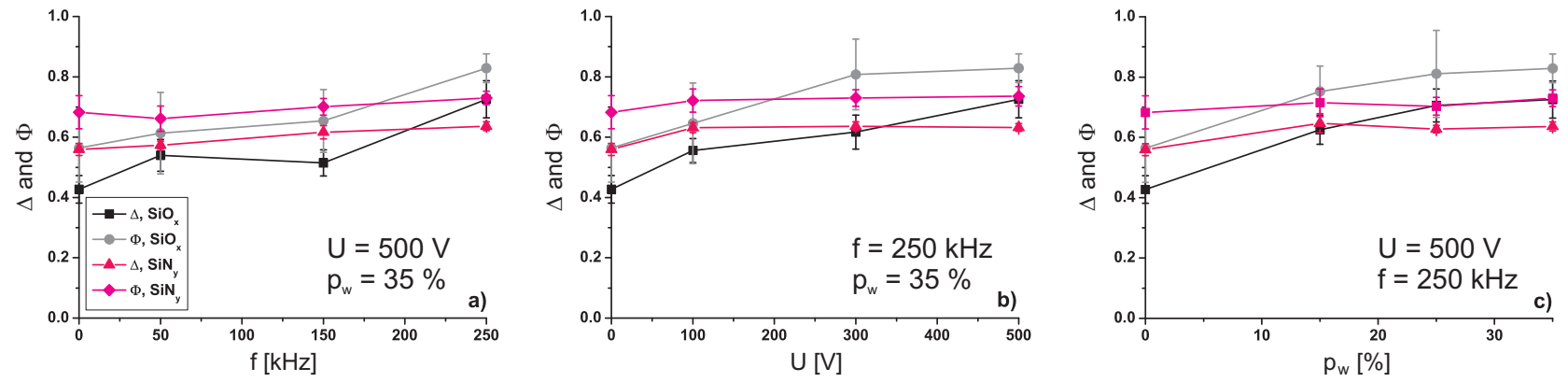


**Fig. 4.5:** Dependence of the parameters  $\Delta$  and  $\Phi$  on the bias parameters a) frequency, b) voltage and c) pulse width. All three characteristics are determined for the  $\text{SiO}_x$  as well as for  $\text{SiN}_y$  films.

for the parameters  $f = 250 \text{ kHz}$ ,  $U = 500 \text{ V}$  and  $p_w = 35 \%$ , which, therefore, are chosen as standard parameters for further investigations. The unbiased  $\text{SiO}_x$  coating of the trenches offers  $\Delta_{\text{SiO}_x} = 0.43$  and  $\Phi_{\text{SiO}_x} = 0.56$ . On the other hand,  $\Delta_{\text{SiN}_y} = 0.56$  and  $\Phi_{\text{SiN}_y} = 0.68$  is obtained. This means that in the unbiased case, the cavities are filled more homogeneously with silicon nitride. This confirms the higher surface mobility of the layer-forming particles by using monosilane as precursor compared to HMDSO. These values increase to  $\Delta_{\text{SiO}_x} = 0.73$ ,  $\Phi_{\text{SiO}_x} = 0.83$ ,  $\Delta_{\text{SiN}_y} = 0.64$  and  $\Phi_{\text{SiN}_y} = 0.73$  at the standard bias parameters. The growth of the silicon-nitride layers can hardly be manipulated (see also section 4.3.1). In addition, the biased  $\text{SiO}_x$  coating becomes more homogeneous than the  $\text{SiN}_y$  one, in spite of the worse surface mobility of HMDSO. This is due to the quantity of the impinging ions: Comparing the used gas-mixture ratios of HMDSO :  $\text{O}_2 = 1 : 20$  and  $\text{SiH}_4 : \text{NH}_3 = 3 : 22$ , less nitride than oxygen ions relative to the number of silicon atoms are available to influence the layer growth. It turns out, that for these geometries of the substrate surface, the trenches cannot be completely coated, such that cavities are developed.

### 4.3 Influence of ion bombardment on the growing layer

In this section, the influence of the ion bombardment on the deposited silicon-oxide and silicon-nitride layers is investigated. First, this will be done on the basis of the model substrates. Subsequently, the surface coatings on steel substrates are analyzed.

#### 4.3.1 Layer growth on model substrates

The analyses of the profile of the deposited layer are carried out separately for silicon-oxide and silicon-nitride layers. The results presented here are for the gas-mixture ratios of HMDSO and oxygen or monosilane and ammonia, for which the deposited  $\text{SiO}_x$  and  $\text{SiN}_y$  films offer the best barrier properties [50]. To guarantee comparable conditions, all investigated layers have an absolute thickness of  $2 \mu\text{m}$  on the upper horizontal surface. All biased coatings were deposited with the standard bias parameters determined in the previous section. To determine the shape of the deposited film especially inside the cavities, the breaking edge of the wafers are analyzed in the scanning electron microscope (SEM) with an observation angle of  $20^\circ$  to the edge, which is often used as standard for considering breaking edges in the material science [77].



### SiO<sub>x</sub> coatings

The SiO<sub>x</sub> coatings shown in Fig. 4.7 were deposited at a gas-mixture ratio of HMDSO : O<sub>2</sub> = 1 : 20. The aspect ratios of  $a = 1$  and  $a = 4$  are considered. The films shown on the left side of the picture (Figs. 4.7a-d) were deposited with a total gas flux of 105 sccm. As reference, a wafer was coated without substrate bias (Figs. 4.7a,b). Above the enhancements, the ball-shaped layer growth as predicted in section 4.1 can be seen. On the smaller trenches, the layer grown left and right of the trench closes rapidly, thus nearly no film is deposited inside the cavity. A crack between the layer parts still remains even though the layer thickness is increased. Hence, such a layer cannot guarantee reliable barrier properties. In the case of the broader trench, the situation is different: Here, a coating of the whole trench is observed, but the deposited film is not homogeneous. The layer thickness decreases along the flanks of the cavity towards the bottom.

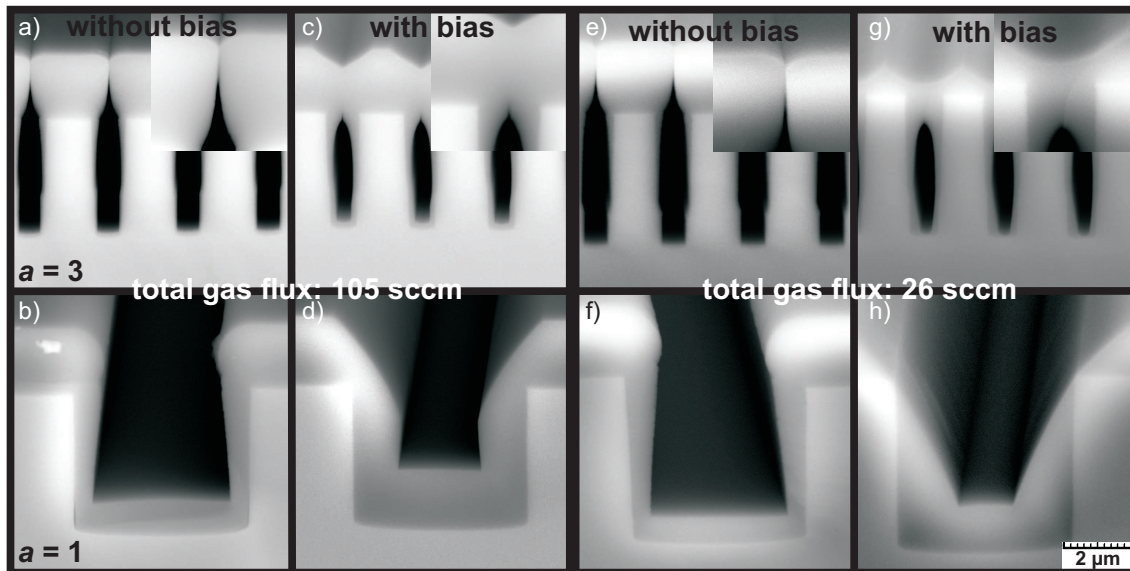


**Fig. 4.7:** Comparison of the profile of layers deposited with and without substrate bias. The analyses are done on trenches with two different aspect ratios (1 and 4) and with two different total gas fluxes (105 and 26 sccm).

The influence of the substrate bias on the step coverage can be observed in Figs. 4.7c,d. In spite of the generally higher deposition rate compared to the unbiased case, the coating of the smaller trenches is not significantly increased. However, the layer over the cavity closes faster because of the higher deposition rate. In comparison with Fig. 4.7a, a great difference is observed: The contact point of the two layer parts is merged due to the enhanced surface mobility of the layer-forming particles induced by the bombardment by high-energetic oxygen ions. This leads to a relocation of the particles in the few upper atomic layers. The effect of the ion bombardment on the chemical structure of the deposited coating will be analyzed

in chapter 6. Since the layer above the still existing cavity merges, the barrier properties of the coating should be guaranteed. This merging leads to smoother layer surfaces as seen in Fig. 4.7c. The coating of the broader trench in Fig. 4.7d is clearly more homogeneous than the one without substrate bias. This effect can be explained by the sputtering of the film edges at the top by the impinging oxygen ions (flattening of the edges). The best sputter yield is observed at an impact angle of  $45^\circ$ . Due to the sputtering, the trench remains open and it can be filled completely. With further deposition, a smoothing of the layer surface is achieved by the fractional sputtering of the film.

In order to study the influence of the deposition rate on the step coverage, analogue depositions were carried out with one fourth of the total gas flux, namely 26 sccm. The results are depicted in Figs. 4.7e-h. The shape of the coating is not changed in the case of the deposition without substrate bias (Figs. 4.7e,f), but in Figs. 4.7g,h, an increased importance of the sputter effect is observed. This is due to the decreased deposition rate. In the smaller trench, a slight increase of the layer thickness on the flanks is observed, but at the bottom no deposition is seen at all. The merging of the film is found deeper inside the trench. This is possible because of an increased surface mobility at decreased deposition rate [41]. In addition, a higher smoothing of the film shoulders is observed, which suggests a complete defect-free filling of the broader trench with further deposition. The abrasive of the layer edges is extended towards the bottom of the indentation. Furthermore, a part of the particles deflected at the flanks are deposited inside the trench, too, which leads to an increased deposition rate.

In conclusion, the barrier properties of  $\text{SiO}_x$  coatings can be improved by substrate biasing. Cracks in the deposited layers are merged because of the enhanced surface mobility. In principle, a more homogeneous coating can be achieved. Lowering the gas flux reduces the deposition rate in favor of the sputter process, which smooths out the layer roughness. This way, broad trenches can be filled completely. However, low deposition rates ( $< 10 \text{ nm/min}$ ) are not competitive for an industrial application to deposit barrier layers with a thickness of 3 to  $4 \mu\text{m}$ . Hence, only the higher gas flux is considered in the following.

### **$\text{SiN}_y$ coatings**

The studies of the  $\text{SiO}_x$ -layer growth at positions of indentations in the substrate surface from the previous paragraph are conferred on  $\text{SiN}_y$  films (Ref. [78]). The coatings were deposited at a gas-mixture ratio of  $\text{SiH}_4 : \text{NH}_3 = 3 : 22$  and a total gas flux of 105 sccm. The coated trenches have the same geometry as the ones deposited with silicon oxide.

The unbiased  $\text{SiN}_y$  coating in Figs. 4.8a and b shows exactly the same properties as the  $\text{SiO}_x$  film shown in Figs. 4.7a and b. A crack is developed in the layer above the remaining cavity. The sputter effect with substrate bias is not as distinctive as in case of the  $\text{SiO}_x$  layers because of the lower number of high-energetic nitrogen



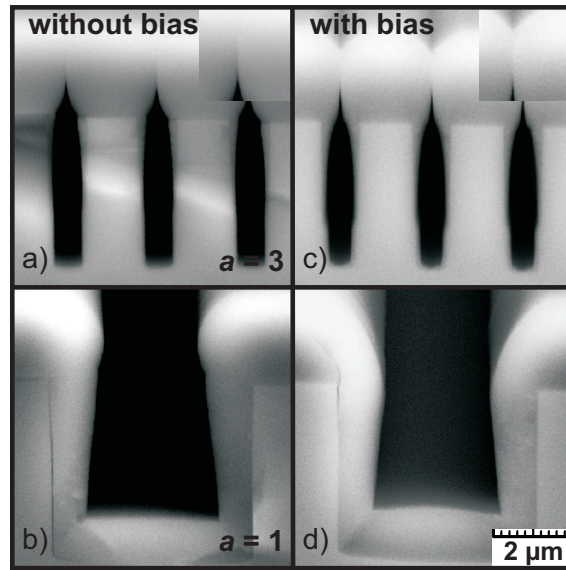


**Fig. 4.8:** Comparison of the shape of  $\text{SiN}_y$  layers deposited with and without substrate bias. The analyses are done on trenches with two different aspect ratios (1 and 4) and with a total gas fluxes of 105 sccm.

ions impinging on the coating surface. The lower number of nitrogen ions compared to the oxygen ions in the HMDSO– $\text{O}_2$  plasma is a result of the different gas-mixture ratios used for these investigations. However, as can be seen in Fig. 4.8c, the energy of the impinging nitride ions is sufficient to merge the coating over the gap, which plays an important role for the barrier properties of the deposited layer.

### 4.3.2 Layer growth on steel

For manufacturing CIGS solar cells on steel as substrate, the layer growth and the barrier properties of the coatings on these substrates is relevant. Here, the layer growth of  $\text{SiO}_x$  coatings on steel with variable surface roughness is studied. Resistance measurements of these coatings are analyzed in section 4.4.

As "test substrates", steel with three different values of the surface roughness characterized by the  $R_a$  value (averaged roughness) is used, namely  $R_a = 30, 34$  and  $182$  nm. The results were published in Ref. [79]. Figure 4.9 shows the surface of the coatings on these substrates, in each case deposited with and without an applied substrate bias. The pictures were done by StEM–Stuttgart Center for Electron Microscopy, Max Planck Institute for Metals Research, Stuttgart. The total thickness of each film is  $3 \mu\text{m}$ .

In each unbiased case (Figs. 4.9a,c and e), the surface structure of the substrate is mapped on the surface of the coating. E.g., in Fig. 4.9a, a crack can be seen in the deposited layer, which is due to the roughness of the substrate surface. In the unbiased cases, the grown layers generally appear rough and cauliflower-like. This

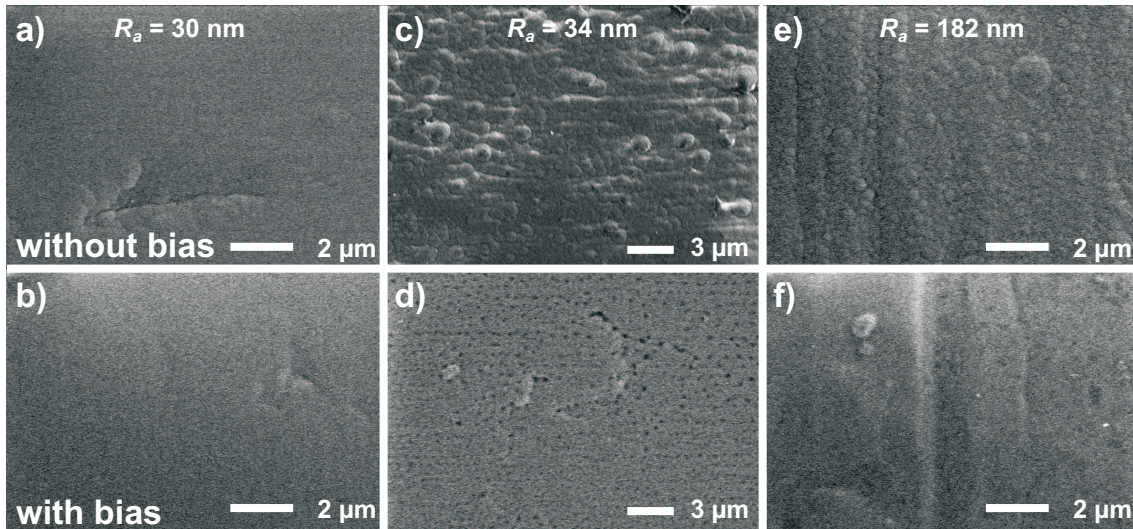


**Fig. 4.9:** Comparison of the surface of  $\text{SiO}_x$  layers deposited on steel with and without substrate bias for a variable surface roughness. The influence of the substrate roughness can be observed. a,b)  $R_a = 30$  nm, c,d)  $R_a = 34$  nm (original substrate used for fabrication of solar cells), e,f)  $R_a = 182$  nm. (STEM–Stuttgart Center for Electron Microscopy, Max Planck Institute for Metals Research, Stuttgart)

structure is more pronounced with increasing substrate roughness.

By biasing the substrate during the deposition, a clear smoothing of the film surface is noticed on all three substrates (Figs. 4.9b,d and f). Hence, a mapping of the substrate surface on the surface of the coating as well as the cauliflower-like layer growth is mostly prevented. This can be seen best in Figs. 4.9a and b: Cracks, which are developed in the deposited layer without bias are smoothed out in the biased coating. In Fig. 4.9f, the filling of the chamfer, which is formed by the milling of the steel, is clearly improved compared with the unbiased deposition. The black speckles in Fig. 4.9d are due to the preparation of the sample. This is no real effect of the film surface.

The results of these studies confirm the ones obtained from the analyses of the layer growth on the model substrates in section 4.3.1. The merging as well as the smoothing of the layer surface, which was shown by analyzing the breaking edge of the model substrates, is observed on the coating of the steel substrates, too.

## 4.4 Analyses of insulation properties

In order to characterize the quality of the barrier layers quantitatively, the resistance of the  $\text{SiO}_x$  and  $\text{SiN}_y$  coatings deposited on steel has been measured before and after the process, in which the CIGS solar cells were applied on the barrier coatings (so-called CIGS process). The resistance was measured with an ohmmeter. For this purpose, separate gold or aluminum pads were vapor-deposited on the film

surface. These pads and the steel substrate form the two electrodes, between which the resistance and the breakdown voltage were measured at different points on the substrate. The percentage of the pads is plotted on the axis of ordinates against the corresponding resistance in logarithmic depiction or breakdown voltage. The influence of the surface roughness as well as the substrate bias on these measurands will be discussed in the following separately for the  $\text{SiO}_x$  and the  $\text{SiN}_y$  layers.

#### 4.4.1 $\text{SiO}_x$ coatings

In Fig. 4.10, the resistance of the barrier films, which were deposited on the steel with variable surface roughnesses, is depicted. Measurements were done before and after the CIGS process. Hence, the influence of this process – especially the heating of the probe up to  $600^\circ\text{C}$  – can be studied. For the measurements after this process, the deposited molybdenum and CIGS film has to be removed. This is done by a chemical etching process.

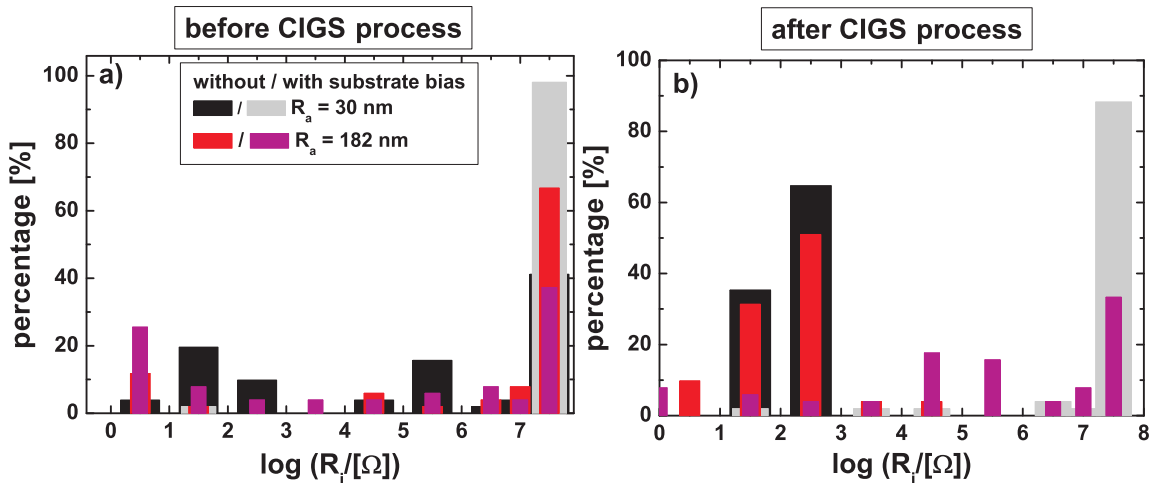


**Fig. 4.10:** Resistance of the  $\text{SiO}_x$  coatings deposited on steel with variable surface roughness, measured a) before the CIGS process, b) after the CIGS process. (ZSW – Center for Solar Energy and Hydrogen Research Baden-Württemberg)

Regarding the case without substrate bias before the CIGS process, there is no clear trend with the surface roughness  $R_a$ . Applying the bias clearly improves the insulation properties of the coating at small  $R_a$ . For large  $R_a$ , the insulation even gets worse. For this phenomenon, no conclusive explanation is found, yet.

However, the situation after the CIGS process, as shown in Fig. 4.10b, is more relevant. In fact, the insulation properties of the unbiased coatings decrease clearly through the CIGS process, whereas the resistance values of the biased films remain nearly constant. Therefore, the  $\text{SiO}_x$  layers deposited with the substrate bias offer a highly improved insulation after the CIGS deposition.

The same trends are found in the breakdown voltage (Fig. 4.11) measured on the same samples as for Fig. 4.10. The breakdown voltage is represented in the

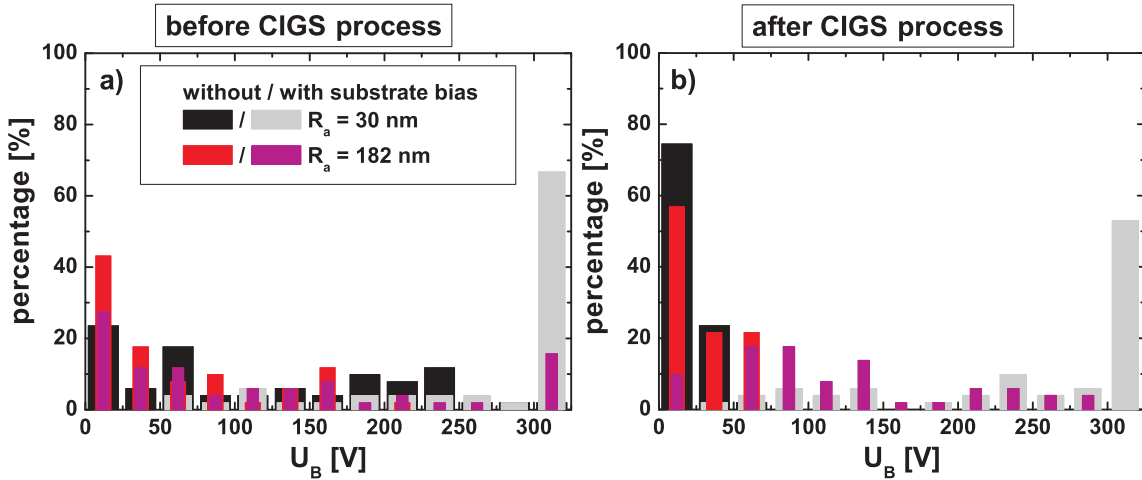


**Fig. 4.11:** Breakdown voltages of the  $\text{SiO}_x$  coatings deposited on steel with variable surface roughness, measured a) before the CIGS process, b) after the CIGS process. (ZSW – Center for Solar Energy and Hydrogen Research Baden-Württemberg)

same way as the layer resistance. The breakdown voltages were measured before (Fig. 4.11a) and after (Fig. 4.11b) the CIGS process, too.

Before the CIGS process, the breakdown voltage of the unbiased coatings are somewhat lower than those of the biased ones. During the CIGS process, the breakdown voltage of the unbiased coatings for both, smooth and rough surfaces, are further reduced. The biased coatings, however, generally feature higher breakdown voltages.

#### 4.4.2 $\text{SiN}_y$ coatings

Measurements equivalent to those described in section 4.4.1 were carried out for the silicon-nitride coatings. Similarly, their resistance and their breakdown voltage were determined, but only on the substrates with  $R_a = 34$  nm. Hence, their roughness is comparable with the one of the smoother substrates of the  $\text{SiO}_x$  coatings in section 4.4.1 with  $R_a = 30$  nm. In Fig. 4.12, the results for the  $\text{SiN}_y$  are compared with the corresponding ones of the  $\text{SiO}_x$ , again before and after the CIGS process.

Before the CIGS process (Fig. 4.12a), the  $\text{SiN}_y$  layers offer clearly better insulation properties than the corresponding  $\text{SiO}_x$  films. The unbiased coating shows only one point of measurement with a value below the upper limit of the ohmmeter (100 M $\Omega$ ). Hence, its insulation is comparable with the one of the biased  $\text{SiO}_x$  coating. The biased one is perfectly insulating. This is due to the a priori higher surface mobility of the monosilane used as precursor for the deposition of the silicon nitride compared to the HMDSO.

During the heating of the CIGS process, the  $\text{SiN}_y$  develops cracks and thus flakes off the substrate. Hence, only one biased layer was preserved enough to carry out measurements. But consequently, the resistance value decreases drastically. It is

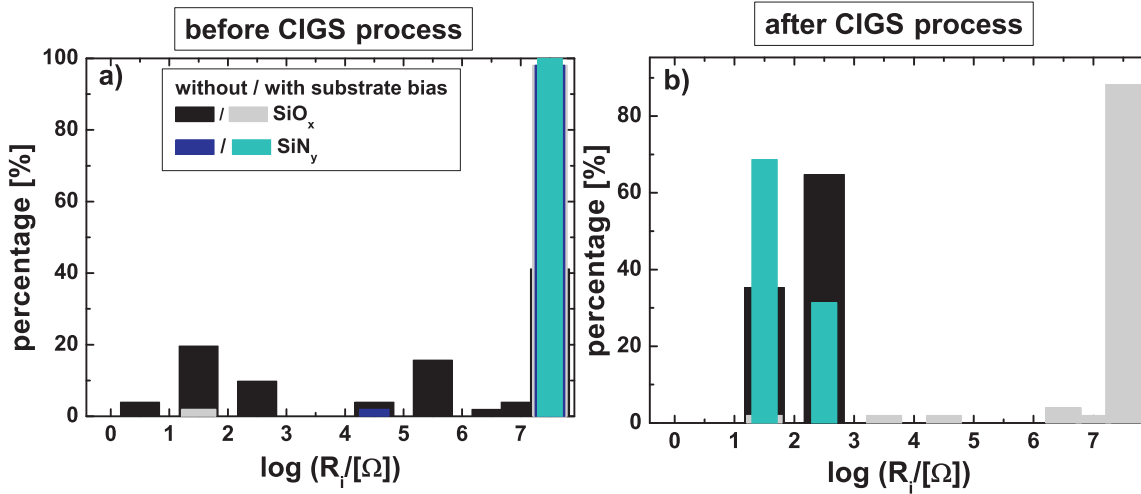


**Fig. 4.12:** Resistance of the SiN<sub>y</sub> coatings on RPG steel with  $R_a = 34$  nm compared with the resistance values of the SiO<sub>x</sub> layers on the steel with  $R_a = 30$  nm from Fig. 4.10, measured a) before the CIGS process, b) after the CIGS process. (ZSW – Center for Solar Energy and Hydrogen Research Baden-Württemberg)

lower than the one of the unbiased SiO<sub>x</sub> coating (Fig. 4.12b).

For this reason, it was only possible to measure the breakdown voltage before the CIGS process. As consistent with the results of the resistance, the breakdown voltage of the SiN<sub>y</sub> films is higher than the one of the SiO<sub>x</sub> coatings. The best properties are offered by the silicon nitride deposited with the substrate bias. The unbiased one has a breakdown voltage comparable to the biased SiO<sub>x</sub>.

## 4.5 Conclusion

The influence of the high-energetic ions impinging on the film surface was analyzed in terms of the layer growth on a rough surface and the insulation properties of the SiO<sub>x</sub> and SiN<sub>y</sub> coatings. To guarantee comparable conditions, model substrates with a trench structure in the  $\mu\text{m}$  range on the surface were used. The layer profiles were analyzed by their breaking edge. The effect of the particular bias parameters were analyzed. The most homogeneous coating of the trenches were obtained for  $f = 250$  kHz,  $U = 500$  V and  $p_w = 35\%$ . These parameters are chosen as standard parameters.

Without substrate bias, the layer tends to close above cavities, but cracks develop at the closure positions. By applying the bias, the coating merges such that the barrier properties of the films are improved. Improved insulation properties were verified by measuring the resistance and breakdown voltage of these coatings. In the unbiased case, SiN<sub>y</sub> coatings already show good insulation properties, which confirms previous results from [50]. Substrate biasing slightly increase their insulation properties. A striking improvement of barrier properties by substrate biasing is



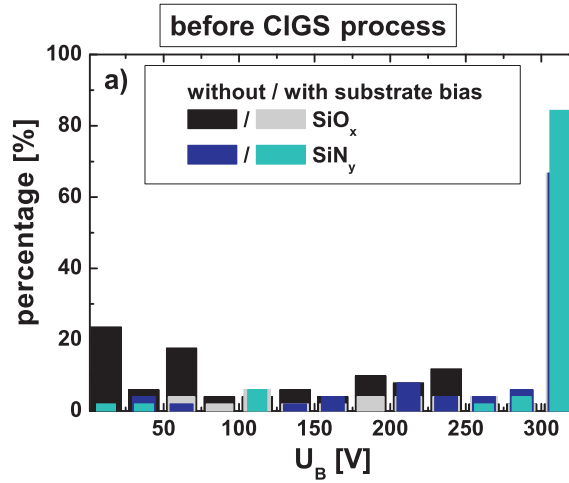


**Fig. 4.13:** Breakdown voltage of the SiN<sub>y</sub> coatings on RPG steel with  $R_a = 34$  nm used as substrate, measured before the CIGS process. It is compared with the results of the SiO<sub>x</sub> layers on the substrate with  $R_a = 30$  nm. (ZSW – Center for Solar Energy and Hydrogen Research Baden-Württemberg)

observed for SiO<sub>x</sub> coatings, which, in this process, reach insulation properties comparable to SiN<sub>y</sub>. Biased SiO<sub>x</sub> coatings could be shown to keep these properties even during the CIGS process, which is more relevant for the fabrication of CIGS solar cells. Biased and unbiased SiN<sub>y</sub> coatings produced in this work, however, failed to survive the CIGS process and results from [50] (i.e. without substrate bias) could not be reproduced. Here, SiN<sub>y</sub> coatings rather tend to higher rejections.

Nevertheless, CIGS solar cells were fabricated successfully on steel substrates ( $R_a = 34$  nm) coated with a SiO<sub>x</sub> barrier. The best results were solar cells with an efficiency of 11.5%. For comparison, CIGS solar moduls available on glass substrates offer an efficiency of 10 to 12%. Here, the CIGS solar cells were fabricated by the ZSW – Center for Solar Energy and Hydrogen Research Baden-Württemberg, which was a project partner within the BMBF project "FlexNet", in whose context the presented analyses were carried out.

## Chapter 5

# Simulations on layer-forming mechanisms

In chapter 4, investigations of the layer growth on substrates with a rough surface were presented. These analyses were done in terms of the step coverage on the basis of model substrates, which guarantee comparable conditions for each coating. The growth processes, which lead to the specific layer shape at the position of indentations on the substrate surface, will be determined by analyzing the layer growth in detail. In particular, the time-dependent process of the layer closure above the cavities is of special interest. This will be done in this chapter by means of simulations with the Monte-Carlo Code SDTrimSP-2D [9], which calculates the interaction of the incoming particles (neutrals or ions) with the substrate surface. Therefore, deposition as well as sputter processes can be computed.

The beginning of investigations of the layer growth on non-planar substrate surfaces is found at the end of the 1960's. It has its origin in semiconductor industry, where the coating of conduction paths on electrical components is of great interest. The size of these steps are in the  $\mu\text{m}$  range. In Ref. [10, 11, 12], the step coverage of such trenches is calculated analytically by taking into account the geometric configuration of the substrate surface and the incoming particles in a sputter process. The systems are characterized by screening effects of the step edges and – with increasing layer thickness – self-shadowing of the coating. In these first calculations, the specific properties of the different species of the layer-forming particles were not regarded. An extension to this approach is the distinction of the various film-forming particles. By an inclusion of their sticking probability, this problem necessitates a numerical solution, which was treated in several works in the 1970's and 1980's [80, 81, 82, 83, 84]. The used simulation algorithm is the Monte-Carlo method in all cases. These analyses calculate the step coverage in dependence of some special process parameters: the substrate temperature (included indirectly by the sticking coefficient), the kind of deposited material as well as the flux and the direction of the incoming particles.

The code SDTrimSP-2D takes all mentioned effects into account, but includes

several add-ons compared to previous simulation codes. It calculates the interaction between the incoming particles and the bombarded target by the binary collision approximation [85]. This offers the possibility to analyze the influence of high-energetic ions bombarding the growing layer surface on the film-forming mechanisms. This ion bombardment occurs in the case of an applied substrate bias during the deposition process.

In the utilized version of the simulation code, chemical reactions on the film surface are not considered. Hence, a simple model system has to be regarded, in which these reactions can be neglected. Taking the deposition of silicon nitride as starting point, the simplest gas system, for which chemical reactions do not play an essential role with respect to the deposition, is a pure monosilane plasma. Therefore, the deposition of hydrogenated amorphous silicon layers is considered. In the present plasma, the main film-forming particles are  $\text{SiH}_3$  radicals. In the case of an applied substrate bias, the impinging  $\text{Si}_2\text{H}_4^+$  ions have to be taken into account additionally. Because both species are generated in the plasma, no chemical surface reactions occur in this system. The film-forming model of this system was introduced in section 3.1.3. The binding reactions, which lead to the adsorption of silicon and hydrogen on the coating surface, are replaced by implanting Si and H in the target.

At the beginning of this chapter, the Monte-Carlo Code SDTrimSP-2D is introduced. The input parameters will be determined, the simulation results will be compared with the experimental ones and the particular film-forming processes, especially in the case of the applied substrate bias, will be discussed. At last, the results will be concluded.

## 5.1 Monte-Carlo code for analyzing ion-solid interactions

The Monte-Carlo code SDTrimSP-2D is the two-dimensional extension of the previous one-dimensional version SDTrimSP [86], which is briefly introduced in the next section. With its help, the main principles forming the basis of these simulation codes calculating collision phenomena in randomized amorphous targets are illustrated. Both Monte-Carlo Codes are a very valuable tool for analyzing ion-solid interactions like implantation, backscattering, transmission, sputtering and composition changes of the ion-bombarded solid. They are mainly used in fusion research to calculate erosion at the reactor wall or the divertor [87]. With the two-dimensional version introduced in section 5.1.2, the influence of a surface structure on the interaction of the incoming particles and the target compounds can be determined.

### 5.1.1 SDTrimSP

The one-dimensional version SDTrimSP combines the two Monte-Carlo simulation codes TRIM [88] and TRIDYN [89] under a new and handy user interface. TRIM



was the first version of this series. It calculates atomic collisions in randomized amorphous targets by the binary collision approximation [85]. In addition, effects of collisions with electrons are implemented in a continuum approach. In its original version, only the slowing down of fast projectiles in the bombarded target is calculated, any recoil atoms and their descendants are disregarded. In the course of time, the code was amended by additional tools, which allow the computation of recoil atoms. Hence, sputtering, reflection and atomic relocation is included as well. Furthermore, the opportunity of utilizing a target, which consists of different material components, was established. As a further development of this feature, the TRIDYN simulation code was developed. It allows treating a non-static target composition and, hence, coating or abrasive processes induced by the incoming particles are included. Thereby, the target composition as well as the kind of incoming particles is not limited. An inhomogeneous target substance is described by  $N$  slabs of different material with an initial thickness  $\Delta x_0^i$ . This is illustrated in Fig. 5.1a.

The quantitative change of the target composition is obtained by taking the total flux of the incoming particles and their energy as well as their solid angle distribution (polar and azimuthal angle) into account. These input parameters lead to a three-dimensional calculation of the collision processes in the target. The output facilities are the reflection coefficients and sputtering yields, the depth distribution of implanted and energy distributions of backscattered and sputtered atoms only in one dimension. A complete overview of the necessary input parameters is given in Tab. 5.1. The visualization is carried out by the scientific data visualization software IDL.

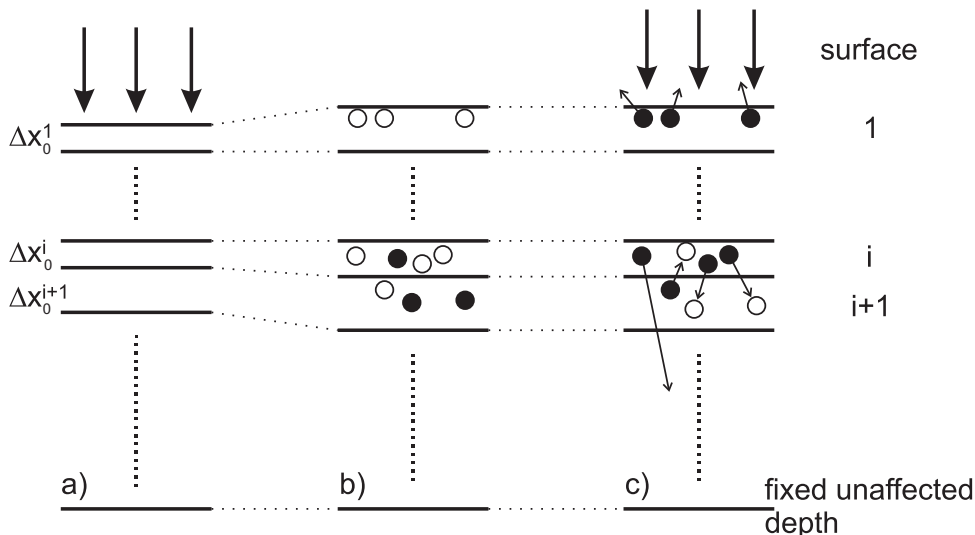


**Fig. 5.1:** Illustration of the processes in the substrate, which occur by bombarding a target with fast projectiles and lead to the resulting deposition or sputtering. The target is sub-divided into separate layers. a) Initial situation, b) the incoming particles cause relocations and sputtering, hence vacancies  $\circ$  and additional atoms  $\bullet$  occur in the different target layers, c) these vacancies are allowed to relax by re-sorting the additional atoms.

The possible change of the one-dimensional target configuration by particle incidence is illustrated in Fig. 5.1. By bombarding the target with energetic projectiles (Fig. 5.1a), atoms can leave it or relocate themselves. Thus, a vacancy at their original target position is generated (Fig. 5.1b). At this position, an additional particle can be implanted directly or by relocating the target atoms (Fig. 5.1c). These mechanisms can take place in the first few target layers close to the surface. Hence, the different target layers have the possibility to grow or to shrink. The expansion or shrinking of the layers is calculated from the total flux of particles (outgoing and incoming ones). By falling below the lower cutoff layer thickness defined in the input file, it is combined with its neighbors. If the target layer exceeds the upper limit, it is split up and the number of layers is increased. Hence, the shrinking or the increase of the summed up layer thicknesses describes the sputtering or the growing of the target, respectively.

The simulation calculates the collision cascades in the target of  $N$  particles, determined by the particle flux and the deposition time. Additionally, the collision cascades of the recoil atoms are computed until the particles reach the cutoff energy. It is defined as the threshold energy, above which the recoil particles can collide with target atoms. The structure of the code consists of three main parts: the projectile loop, the recoil loop and the target update. In the projectile loop, the trajectory of  $NR \geq 1$  particles ( $NR$  is defined by the total particle flux  $N$  and the number of loops  $NH$ ) is calculated by following the projectiles from collision to collision. The parameters of the recoil atoms are computed in the separate recoil loop. After this, the target is updated following the scheme described above. This procedure is iterated until all  $N$  considered impinging projectiles are processed. This leads to  $N/NR = NH$  calculation loops.

### 5.1.2 SDTrimSP-2D

With the two-dimensional version SDTrimSP-2D, whose structure is organized analogically to the one-dimensional code, the interaction of particles impinging on a two-dimensional target surface and the target atoms can be computed. This allows for a morphological analysis of a target by a bombardment of high-energetic projectiles as well as for studies of the influence of the surface roughness on deposition and sputtering processes. Hence, this code allows to simulate the layer growth on the model substrates introduced in section 4.3.1.

The grid discretization determines the dimensionality of the output, because the particle collisions are already computed in three dimensions. Hence, the only difference to SDTrimSP is a modified target model in this two-dimensional version. The target is sub-divided into cells instead of layers. Thus, a second dimension of the target is obtained and a two-dimensional exchange of particles between the discrete cells is possible. The density changes in the target material are due to projectile and recoil particles coming to rest at the end of their trajectories by reaching a predefined cutoff energy. Along its trajectory, each particle creates a mass flux by

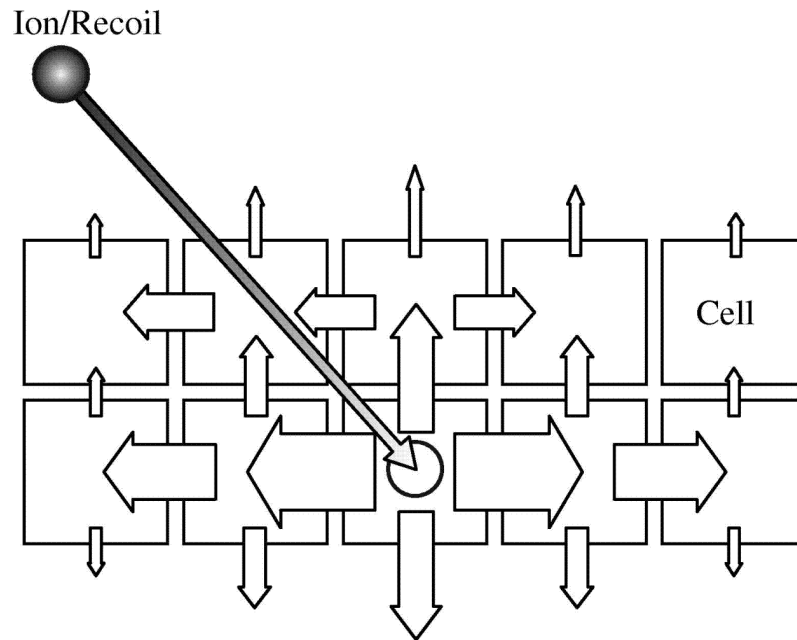


**Fig. 5.2:** This figure shows the two-dimensional cell configuration of the target in the Monte-Carlo code SDTrimSP-2D with the possible growing or shrinking mechanisms of these cells. The arrows illustrate the incoming and outgoing particle flux at the cell edges, from [90].

collisions in the cells it passes, which leads to a change in the particle densities in these cells. These fluxes can act as sink or source terms for the particle densities. This is illustrated in Fig. 5.2. Particle conservation within the numerical setup is reflected in volume changes of the cells, which are used to represent changes of the number of particles in a cell. For each cell, the resulting mass fluxes (representing the transfer of particles into or out of the cell) are taken to be anisotropic by introducing an anisotropy coefficient. This anisotropy coefficient defines the ratio of horizontal and vertical volume changes. The horizontal transport (parallel to the surface) is usually set smaller than the vertical one, because experimentally, swelling or shrinking are primarily observed in the vertical direction. In the simulations presented here, an anisotropy coefficient of 0.5 was used. The relaxation process is done in several iterations until the divergence of the mass fluxes becomes zero and steady-state conditions without internal tension are obtained. In addition, splitting and annihilation of cells was introduced in SDTrimSP-2D – similar to the target layers in SDTrimSP – relying on a maximum and minimum number of atoms per cell volume in order to accommodate the creation of holes or strong deposition.

## 5.2 The input parameters

To simulate the specific layer growth with the code SDTrimSP-2D, the corresponding input parameters of this deposition process have to be determined. These are the plasma parameters in the Plasmodul as well as the coating parameters obtained by characterizing the deposited films. Because of different coatings deposited with and without substrate bias, the parameters must be defined for each case separately. The effect of the  $\text{Si}_2\text{H}_4^+$  ions, influencing the layer growth in the case of an accelerating potential in front of the target, have to be taken into account in the case of an applied substrate bias. Hence, the ions and the  $\text{SiH}_3$  radicals must be treated independently. The detailed growth mechanism of an a-Si:H layer in a monosilane plasma is explained in section 3.1.3.

An overview of the determined input parameters is given in Tab. 5.1. How they are estimated is described in the following.

impinging particle		
parameter	$\text{SiH}_3$ radicals	$\text{Si}_2\text{H}_4^+$ ions
impact energy [eV]	1	1500
azimuthal impact angle	$2\pi$	$2\pi$
polar impact angle	$0..80^\circ$ (uniformly distributed)	$0^\circ$
particle flux [ $\text{m}^{-2}\text{s}^{-1}$ ]	$1.27 \cdot 10^{20}$	$6.34 \cdot 10^{18}$
sticking coefficient	0.25	0.25
coating		
parameter	unbiased	biased
H content of coating [at%]	16	11.8
atomic density of coating [ $\text{g}/\text{cm}^3$ ]	1.67	1.67
surface binding energy of Si [eV]	2.25	2.25 [91, 92, 93]
surface binding energy of H [eV]	0	0
cell dimensions [nm]	5	5

**Tab. 5.1:** Overview of the input parameters of the code SDTrimSP-2D in the case of an unbiased (only  $\text{SiH}_3$  radicals) and a biased ( $\text{SiH}_3$  radicals and  $\text{Si}_2\text{H}_4^+$  ions) target.

- **Impact energy:** The impact energy of the  $\text{SiH}_3$  radicals on the target is the thermal energy in each case (1.1 eV), because the flow of neutrals cannot be influenced by an external electric field. Without any substrate bias, the energy of the ions is the thermal one as well. Thus, the energy input of the ions on the layer surface is insignificant and can be neglected. With substrate bias, their energy is determined on the basis of the voltage characteristics (measured at the standard bias parameters) shown in Fig. 5.3:

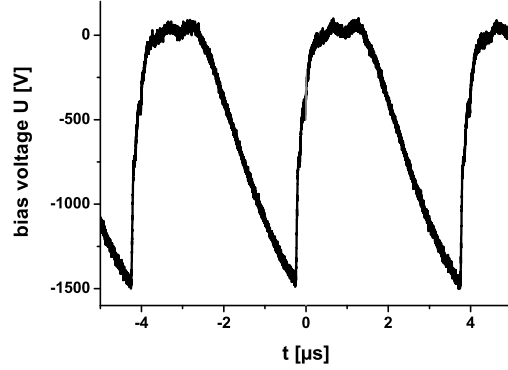


**Fig. 5.3:** Voltage characteristics of the applied substrate bias in the monosilane plasma

By inserting the plasma parameters in front of the substrate holder ( $n_e = 7 \cdot 10^{16} \text{ m}^{-3}$ ,  $T_e = 0.8 \text{ eV}$  at  $U = 500 \text{ V}$  from 3.4.1) into Eq. (2.23), the residence time of the ions in the plasma sheath is estimated to  $\tau_i \approx 0.18 \mu\text{s}$ . Thus, the ions remain much shorter than one cycle in the sheath region. Therefore, they can absorb a maximum energy of 1500 eV by crossing the plasma sheath. For simplification, this value is kept constant. It corresponds to the ion energy calculated by Eq. (2.55).

- **Flux of the  $\text{SiH}_3$  radicals:** The flux of the  $\text{SiH}_3$  radicals is estimated by the gas flow through the setup:

$$\phi_{\text{SiH}_3} = n_{\text{SiH}_3} v = n_{\text{SiH}_3} \frac{V_V}{At} = n_{\text{SiH}_3} \frac{1}{At} \frac{p_A V_A T_V}{T_A p_V}. \quad (5.1)$$

$n_{\text{SiH}_3}$  is the density of the  $\text{SiH}_3$  radicals,  $v$  their velocity,  $t$  the duration of stay of the particles in the device,  $A$  the area of the setup ( $0.071 \text{ m}^2$ , see section 3.2.1) and  $V_V$  the gas volume under low-pressure conditions. With the general gas equation,  $V_V$  is expressed by the gas volume  $V_A$  at atmospheric pressure  $p_A$  and room temperature  $T_A$ , the temperature in the plasma  $T_V$  and the working pressure  $p_V$ . The pressure for the deposition of a-Si:H films was  $p_V = 0.06 \text{ mbar}$ , the temperature in the plasma is assumed to be  $500^\circ\text{C}$ , room temperature is  $20^\circ\text{C}$ , the fed gas volume was  $20 \text{ sccm}$  and the density of the radicals in the plasma is approximately  $n_{\text{SiH}_3} = 2 \cdot 10^{19} \text{ m}^{-3}$  [94]. With these parameters, the  $\text{SiH}_3$  flux is  $\phi \approx 1 \cdot 10^{19} \text{ m}^{-2}\text{s}^{-1}$ . The flux used in the simulations is about one order of magnitude higher, namely  $\phi = 1.27 \cdot 10^{20} \text{ m}^{-2}\text{s}^{-1}$  (determined by comparing the simulation with the experimental

results). This is justified, because in Ref. [94] the electron temperature was measured to  $\approx 1.5$  eV, and in the setup used in this work, it was determined to 2.4 eV (section 3.4). Therefore, the dissociation rate can be considerably higher than in [94]. A second difference in the experiments is the way of coupling the microwave into the plasma, which can lead to different plasma parameters as well.

- **Flux of the  $\text{Si}_2\text{H}_4^+$  ions:** The flux of the ions in Ref. [94] is about 1 % of  $\phi_{\text{SiH}_3}$ . In this work, best agreement of simulations and experiments was obtained for  $\phi_{\text{Si}_2\text{H}_4} = 0.05\phi_{\text{SiH}_3}$ .
- **Sticking coefficient:** The sticking coefficient of the  $\text{SiH}_3$  radicals at an a-Si:H surface is found in literature. It is temperature dependent. In Ref. [59],  $s = 0.1$  for  $T < 350$  °C and above this temperature  $s = 0.25$  is given. In other works, the threshold for a change in the sticking coefficient is given in the range of 250 to 400 °C [95, 96, 61]. Here, the sticking coefficient is set to 0.25 for the standard substrate temperature of 250 to 300 °C.
- **Target material:** The target consists of pure silicon (section 4.1) at the beginning of the deposition process. However, the deposited coating includes hydrogen as well. The hydrogen content of the deposited silicon film was measured by the effusion method [97]. An H content of 11.8 % and 16 % was measured with and without substrate bias, respectively.
- **Target density:** The density of the deposited layers was determined by measuring the mass of the substrate before and after the deposition. It is given by the ratio of the mass difference and the volume of the deposited film.

### 5.3 Comparison of simulation and experimental results

In a first step, the growth of coatings deposited without any substrate bias were simulated. On their basis, the flux of the  $\text{SiH}_3$  radicals was determined by comparing the layer thickness from simulation and experiment. Taking the deposition rate (obtained by the deposition time and layer thickness) and the density of the coating into account, the particle flux can be deduced. This was necessary, because this input parameter is the only one, which could not be identified exactly by measurements or from literature, see section 5.2. The flux of the radicals is assumed to be equal in the case of an applied substrate bias. The flux of the  $\text{Si}_2\text{H}_4^+$  ions is then determined separately from the coatings deposited with an applied substrate bias in an analogue way.

The simulation analyses were carried out on the basis of the investigations on the layer growth described in section 4.3.1. Two different aspect ratios of the model



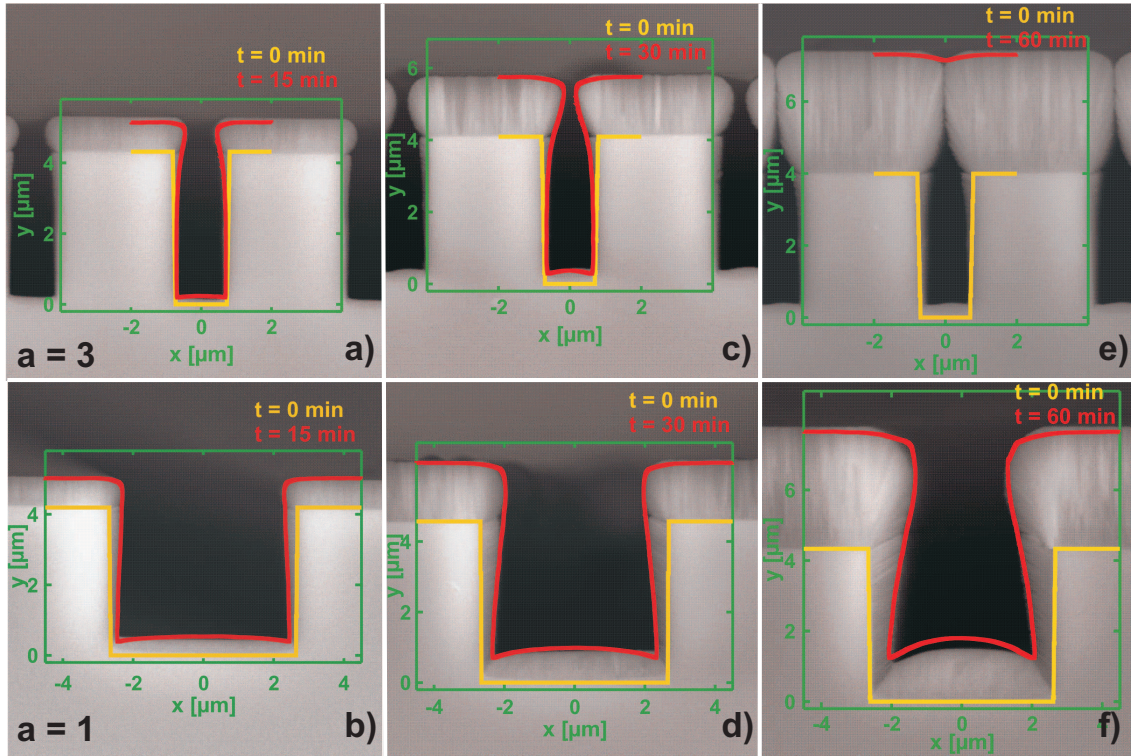


**Fig. 5.4:** Comparison of simulated and measured layer growth, deposited without substrate bias onto indentations in the substrate surface. The aspect ratio of the two investigated trenches is  $a = 3$  and  $a = 1$ . The shape of the original substrate cavity is depicted as the line at  $t = 0$  min. (These results were carried out in cooperation with Ralf Schneider, Ernst-Moritz-Arndt University Greifswald and Andreas Mutzke, IPP Greifswald - Max-Planck Institute for plasma research.)

substrate are regarded:  $a = 3$  and  $a = 1$ , describing a relatively small and a wide indentation in the substrate surface, respectively. Figure 5.4 shows the temporal evolution of the layer forming on these substrates without any substrate bias. A deposition time of 15, 30 and 60 min was chosen. After simulated 60 min of the deposition, the layer is just closed over the smaller cavities. The shape of the Si wafer before the deposition is depicted as the state at the time  $t = 0$  min. In Fig. 5.4, the simulation results are plotted over the SEM pictures of the corresponding experimental coatings. A very good agreement of the simulated and measured layer growth is observed in the case of both aspect ratios. The simulation shows the decreasing film thickness alongside the flanks of the bars similar to the real layer as well as the spherical layer growth on the top. The profiles of the coating at the bottom of the trench agrees, too. In Fig. 5.4e, the only restriction of the simulation code becomes apparent: If the layer is closed over the indentation the developed cavity is not reproduced, because the code SDTrimSP-2D only computes surface effects. This implies that a crack, which can separate the two film spheres on the enhancements,

is not illustrated as well. However, the surface of the coating is reproduced very well. Because of the agreement of the simulations with the experiment during the whole process for different substrate geometries, the choice of the input parameters can be regarded as correct.

Similar investigations were carried out for layers deposited with substrate bias. The following coatings were created with the standard bias parameters determined in section 4.2:  $f = 250$  kHz,  $U = 500$  V and  $p_w = 1376$  ns. With the given flux of  $\text{SiH}_3$  radicals, the flux of the  $\text{Si}_2\text{H}_4^+$  ions can be determined. The result is  $\phi_{\text{Si}_2\text{H}_4} = 0.05\phi_{\text{SiH}_3} = 6.34 \cdot 10^{18} \text{m}^{-2}\text{s}^{-1}$ . This ratio is of the same order of magnitude as the one given in Ref. [94].

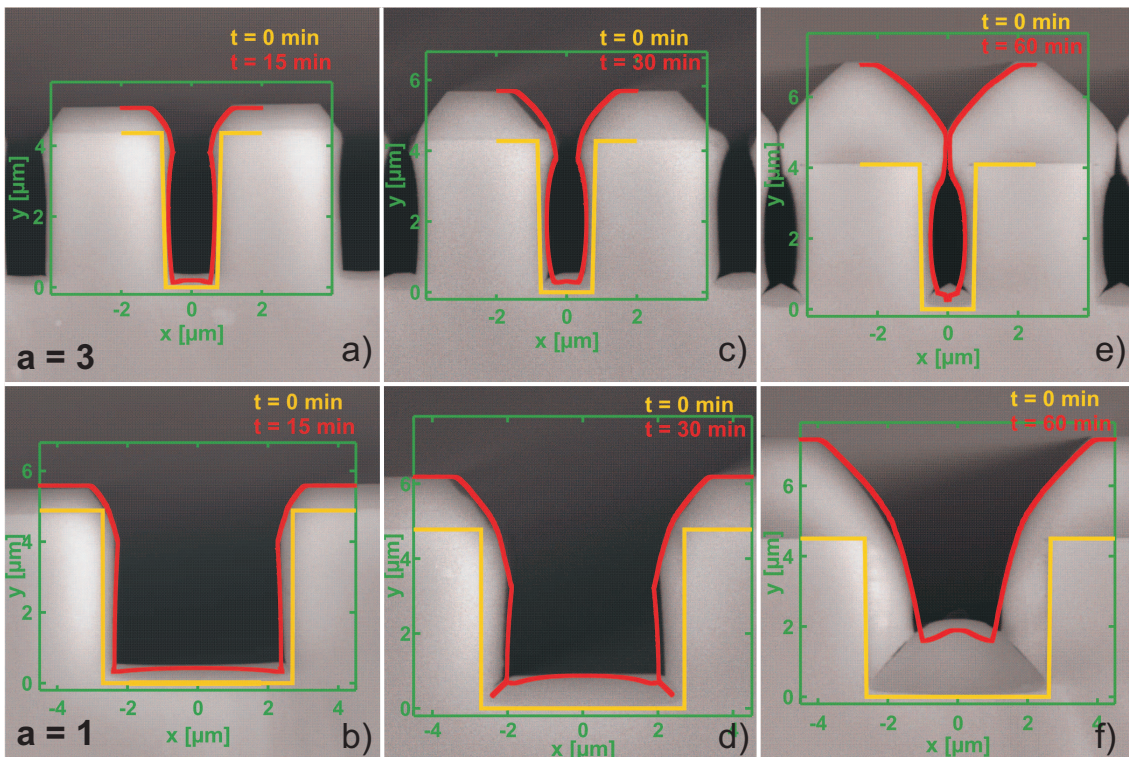


**Fig. 5.5:** Comparison of simulated and experimental coatings deposited with substrate bias in the same representation as in Fig. 5.4 for the same aspect ratios. (These results were carried out in cooperation with Ralf Schneider, Ernst-Moritz-Arndt University Greifswald and Andreas Mutzke, IPP Greifswald - Max-Planck Institute for plasma research.)

The results of the simulation are shown in Fig. 5.5 in the same representation as in Fig. 5.4. As for the unbiased coatings, the growth process is well described by the simulation. The sputter effects induced by the energetic ions as observed mainly at the upper edges of the coating are reproduced very well. A difference between simulation and experiment is observed at the bottom of the cavities. This can be seen best after 60 min deposition in Figs. 5.5e,f, where a smaller layer thickness is produced by the simulations compared with the experimental results. Consequently,



an additional mechanism, which is not accounted for in the code, must contribute to the layer growth. A possible mechanism is the entrainment of material, which is sputtered or reflected at the edge by the incoming flux of the high-energetic ions into the cavity. This is a process, which occurs in the plasma phase and is not considered in the code SDTrimSP-2D, which only computes the interaction of the particles from the plasma with the substrate atoms.

The cracks above the overgrown cavities, which are developed in the layer deposited without substrate bias, cannot be reproduced by the simulation. The differences in the layer growth at these positions, as they are worked out in detail in section 4.3.1, cannot be resolved here. Nevertheless, the physical processes, which lead to the particular shape of the deposited film, can be analyzed with the simulation code. This will be done in the following section.

## 5.4 Film-forming processes

In a common PECVD process, the shape of the deposited layer can be explained mainly by the geometry of the substrate surface (shadowing effects), the angular distribution of the incoming particles and their sticking probability. Thus, the layer growth of these coatings can be simulated with the already existing Monte-Carlo codes, which can be found in literature [80, 81, 82, 83, 84]. In such a deposition process, the chemical reaction of the layer-forming radicals with the target or the already grown coating is more or less insignificant, because of the (low) thermal energy of the film-forming radicals. Hence, the mechanism, which leads to the layer growth and, therefore, to the observed shape of the coating, is only the adherence of the incoming radicals.

By applying a bias voltage to the substrate, the ions are accelerated from the plasma to the substrate surface. Their high-energetic impinge on the surface leads to an increase of the total surface mobility of all target atoms. Thus, the interaction of the impinging ions and the target (collision cascades inside the target) becomes important for the layer growth. In addition to the local deposition, the code SDTrimSP-2D calculates the local reflection, loss, sputtering and redeposition. The locally lost atoms have the opportunity to redeposit at another position with the sticking probability  $s$ . Figure 5.6 explains the representations of these values in dependence of the normalized coating surface. This example shows the case for a deposition time of 0 min, i.e. the beginning of the deposition. To this end, the surface is expanded and then replicated on the abscissa. The positions  $t_1$  and  $t_2$  represent the edges on the top of the flanks,  $b_1$  and  $b_2$  the corners at the bottom of the cavity. The following diagrams are depicted in this way.

In Figs. 5.7a and b, the local reflection, loss, sputtering and deposition calculated with regard to the ions and the radicals are shown. In Figs. 5.7c and d, these parameters are opposed to those analyzed on the basis of the ion influence only. In Figs. 5.7a and b, the local deposition exceeds the local loss. Otherwise, no coating

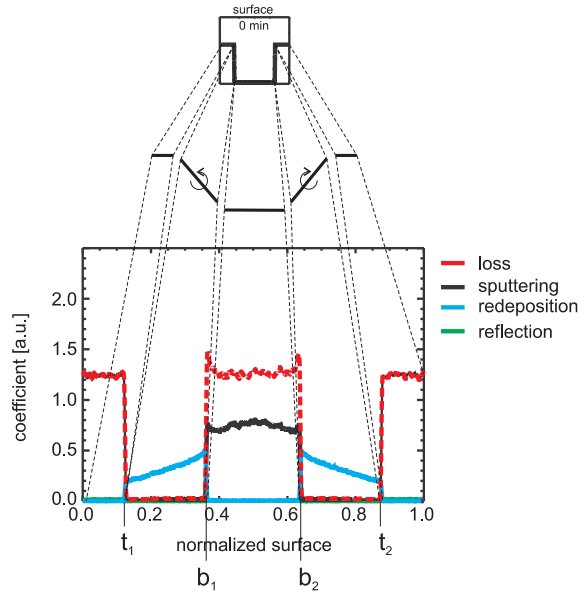


**Fig. 5.6:** Illustration of the normalized surface as abscissa for representing the code output. (These results were carried out in cooperation with Ralf Schneider, Ernst-Moritz-Arndt University Greifswald and Andreas Mutzke, IPP Greifswald - Max-Planck Institute for plasma research.)

would be deposited and a sputter process would be obtained. The local deposition has its largest value on the upper surface of this geometry and inside the cavity it is reduced, especially at the flanks. In order to distinguish between directly deposited particles (mainly radicals) and redeposited ones (mainly induced by the ions), the same parameters are depicted in Figs. 5.7c and d for the case, where the effect of the ions is taken into account. Obviously, the local loss, sputtering and reflection are affected only by the ions, because they show the same characteristics as in Fig. 5.7a and b. However, the characteristics as well as the values of the local deposition changes significantly, which is now determined by the redeposition of lost particles. In order to understand the differences in the layers formed with and without substrate bias as observed experimentally in section 4.3.1, the effect of the impinging ions can now be isolated. The influence of only the ions will be examined in the following.

Figure 5.8 shows the local loss, sputtering, redeposition and reflection in dependence of the normalized film surface at three different time steps of the deposition process (0, 30 and 60 min) and for the coating on the two cavity dimensions ( $a = 1$  and  $a = 3$ ). The deposition time of 0 min (Figs. 5.8a and b) represents the geometry of the uncoated model substrate. At the beginning of the deposition, the main occurring process is the local loss on the horizontal surfaces on the top of the substrate as well as at the bottom of the trench. Because of the vertical incident of the ions, a particle loss on the parallel flanks cannot occur. The atoms lost at the top of the substrate are sputtered; they leave the substrate surface since redeposition on the

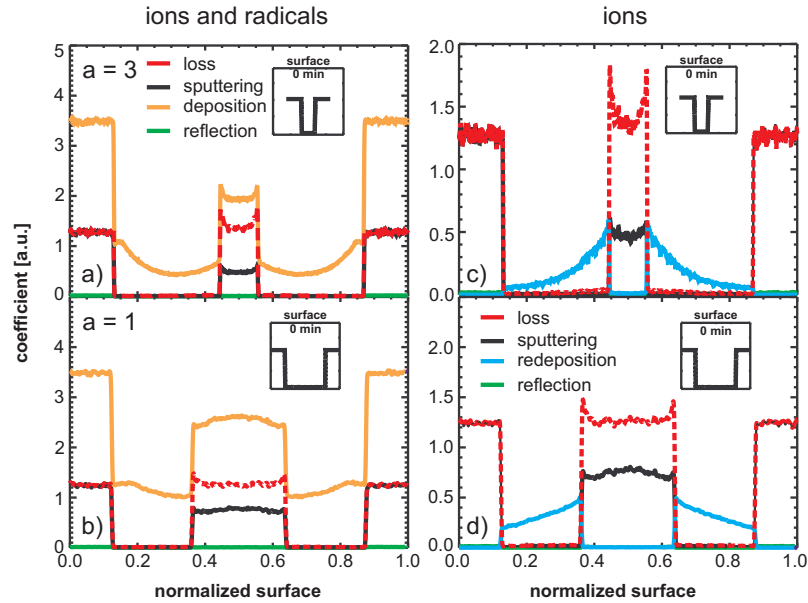


**Fig. 5.7:** Local layer-forming mechanisms (reflection, loss, deposition and sputtering) at the beginning of the deposition on a trench with an aspect ratio of  $a = 3$  (a,c) and  $a = 1$  (b,d). The local processes are depicted in dependence of the normalized film surface. a,b) Influence of radicals and ions on the parameters, c,d) ion influence on these parameters, only. (These results were carried out in cooperation with Ralf Schneider, Ernst-Moritz-Arndt University Greifswald and Andreas Mutzke, IPP Greifswald - Max-Planck Institute for plasma research.)

horizontal surface is not possible. The lost particles at the bottom of the cavity can leave it or be redeposited at the flanks of the indentation. The greatest value of the redeposition occurs at the lower edges of the trench  $b_1$  and  $b_2$  and decreases upwards. This explains the observed coating at the flanks. The number of the lost particles is the sum of the sputtered and redeposited ones.

Another peculiarity are the two peaks occurring in the local loss and sputter yields. These peaks correspond to the bottom corners  $b_1$  and  $b_2$ , which do not have any neighbor cells on one side. Hence, one half of the compensating particle flux is missing. The consequence is a higher loss of particles. Additionally, this is intensified by geometrical focussing effects of the particles in these corners. These peaks are observed in [98], too, where the sputtering of a surface structure was analyzed.

Figures 5.8b and e show the situation after a deposition time of 30 min for the two considered trenches. A distinct feature is the change at the flattened layer edges  $t_1$  and  $t_2$ . The local loss is clearly increased at these positions compared to the one on the horizontal surfaces. The maximum value of this parameter is found at an angle of incidence of  $45^\circ$  of the ions on the film surface. Like for the situation at  $t = 0$  min, the number of lost particles on the horizontal surface at the outside of the indentation is governed by the sputtered ones. The situation inside the cavity is also comparable with the initial situation: The atoms lost at the bottom can leave

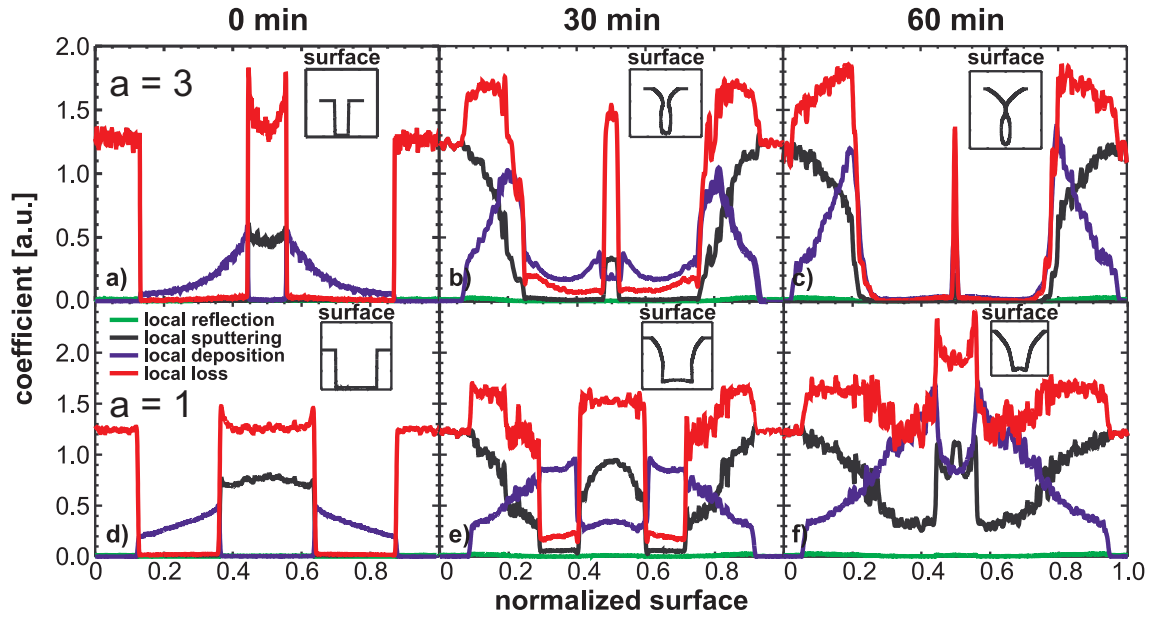


**Fig. 5.8:** Local layer-forming mechanisms (reflection, loss, redeposition and sputtering, induced only by ion bombardment) at different deposition times (0, 30 and 60 min) on a trench with an aspect ratio of 3 (a,c,e) and 1 (b,d,f). The local processes are depicted in dependence of the normalized coating surface. (These results were carried out in cooperation with Ralf Schneider, Ernst-Moritz-Arndt University Greifswald and Andreas Mutzke, IPP Greifswald - Max-Planck Institute for plasma research.)

the film surface, or they can be redeposited. For the redeposition, a clear difference to the first case can be observed: The particles lost at the flattened layer edges above have the opportunity to enter the indentation. To explain the redeposition at the flattened layer edges  $t_1$  and  $t_2$  above the cavity, the two different aspect ratios have to be distinguished: At the smaller trench in Fig. 5.8b, the cavity is almost closed by the deposited film. The layer edges overlap the gap. Hence, the lost particles inside the hole have almost no opportunity to leave the indentation. This first leads to a decreasing and then again increasing redeposition along the upward flanks. At the positions, where the formed layer tends to close the cavity, the local redeposition has its largest value. On the one hand, this is caused by the process inside the cavity as explained. On the other hand, the particles, which are lost at the flattened coating edges above the closure, are increasingly prevented from entering the cavity and, therefore, contribute to the redeposition, too. Due to the abrasion of the edges, the closure of the film is drawn deeper inside the trench compared to the unbiased case. In comparison, the wider cavity depicted in Fig. 5.8d shows a smooth hill-shaped characteristics of the redeposition at the bottom of the trench and an almost constant value of this parameter alongside the flanks. The sputter characteristics is similar to the one of the small trench. Most of the sputtered atoms are lost in the middle of the bottom level, without colliding with the film surface

and then being redeposited.

At  $t = 60$  min, the smaller trench (Fig. 5.8c) is narrowed further. Hence, only in the very middle of the cavity, particles can be lost. The parameter characteristics outside the indentation is comparable to that in Fig. 5.8b. For the wider cavity in Fig. 5.8f, the situation is similar to that in Fig. 5.8e with the only difference that the flanks are not parallel to the ion direction anymore. They are formed aslope by the lost and redeposited particles. As a consequence, the local loss at the flanks is non-zero.

In general, it is observed that the decrease of the local redeposition results in an increase of the local sputtering. Additionally, the reflection of incoming particles at the coating surface turns out to be zero at all time steps.

## 5.5 Conclusion

By analyzing the parameters like the local reflection, loss, redeposition and sputtering, the special shape of the deposited layer at positions of indentations in the substrate surface can be explained. Especially the effect of an ion bombardment of the substrate surface as induced by an applied substrate bias can be differentiated. It was shown, that the deposited radicals do not effect loss and sputtering processes because of their low impact energy. These processes are caused by the impinging high-energetic ions. The strongest effect of the ions is obtained at the upper edge of the flanks ( $t_1$  and  $t_2$ ). Here, the local loss reaches its maximum. Before the film is closed above the cavity, the locally lost particles can effectively be redeposited at the bottom, which leads to thicker and more homogeneous coatings inside the cavity.



# Chapter 6

## Influence of the ion bombardment on the molecular composition

The ion bombardment influences not only the profile of the growing layer, like it was discussed in the chapters 4 and 5, but also the molecular composition of the deposited film. Due to the impact of energy on the film surface, already existing chemical bonds can crack and new ones can be formed. The molecular composition in the microscopic point of view has a significant influence on the macroscopic material properties like adhesion, flexibility and diffusion behavior. Since there was no possibility to directly measure the diffusion behavior of the coatings in the context of this work, the effect of the bias on the molecular structure will be analyzed in section 6.1, so that conclusions on the diffusion behavior are drawn indirectly.

Additionally, a possible variation of the refractive index of these layers with increasing bias voltage will be analyzed in section 6.2. This is of special interest for optical applications of the films like anti-reflection or interference filters. This topic is discussed in Ref. [99] in detail. At the end of this chapter, a short conclusion will be given.

### 6.1 Fourier-transform infrared spectra

The molecular composition of the coatings will be analyzed on the basis of Fourier-transform infrared spectra. They were measured ex-situ with an angle of incidence of  $12^\circ$  in reflection with the spectrometer introduced in section 3.3.1. This low angle of incidence was chosen to prevent strong interferences in the spectra. Additionally, a polarizator prevents the Berreman peak, which is an optical effect and superimposes the oscillation peaks in the spectra. This effect is discussed in detail in Ref. [51, 100]. To exclude a shift of the particular peaks in the spectra with increasing bias due to a possible shift of the refractive index, films with the same optical thickness were investigated. The optical thickness is defined as the product of the refractive index and the total layer thickness  $N \cdot d$ . Thus, if the refractive index increases,  $d$  will

decrease and vice versa. Consequently, the duration of stay of the IR beam inside the analyzed film remains constant and the resulting spectra are comparable.

The optical thickness was controlled with the in-situ FTIR diagnostics during the deposition. For stoichiometric silicon dioxide with a refractive index of  $N = 1.46$  [101] and a total layer thickness of  $1 \mu\text{m}$ , the first destructive interference occurs at a wavelength of  $4 \mu\text{m}$  at an angle of incidence of  $72^\circ$ . This wavelength is related to a wavenumber of  $2500 \text{ cm}^{-1}$ . Hence, the corresponding optical thickness is about  $1.5 \mu\text{m}$ . Like in Ref. [51], this value is chosen as a constant parameter for the further analyses.

The influence of the gas-mixture ratio on the molecular composition was analyzed in previous works for  $\text{SiO}_x$  [51, 102, 43, 42] as well as for  $\text{SiN}_y$  films [99, 63, 50, 55]. Therefore, the main aspect of this chapter is the analysis of the influence of increasing bias voltage on the molecular composition. This will be done separately for the  $\text{SiO}_x$  and the  $\text{SiN}_y$  films, each for two different ratios of the plasma-forming gases.

### 6.1.1 Silicon oxide

Figure 6.1a shows the IR spectra (in the spectral range from  $4000$  to  $400 \text{ cm}^{-1}$ ) of the coatings deposited with  $\text{HMDSO} : \text{O}_2 = 1 : 20$ . To analyze the influence of the bias voltage, it was increased in  $100 \text{ V}$  steps up to  $500 \text{ V}$ . The frequency and the pulse width were kept constant at  $f = 250 \text{ kHz}$  and  $p_w = 35 \%$ , respectively. The substrate temperature was set to  $250^\circ\text{C}$  during all depositions. All spectra show the characteristic band spectrum of  $\text{SiO}_x$  films with its main peak at approximately  $1000 \text{ cm}^{-1}$ , which is accompanied by the lateral band at about  $810 \text{ cm}^{-1}$  and a broad shoulder at  $1150 \text{ cm}^{-1}$ . These peaks, together with the single one at  $440 \text{ cm}^{-1}$ , are related to  $[\text{Si-O}]$  vibrations in the  $\text{SiO}_x$  network. Additionally, a weak band at  $3650 \text{ cm}^{-1}$  occurs, which represents free  $[\text{O-H}]$  oscillations [103]. The absence of associated  $\text{Si-}[\text{O-H}]$  oscillations in the range  $3100$  to  $3600 \text{ cm}^{-1}$ , however, indicates that the contribution of the OH compound is low. The double peak at  $2316$  and  $2364 \text{ cm}^{-1}$  results from  $[\text{C-O}]$  oscillations of the  $\text{CO}_2$  molecule, which was detected in the ambient air of the sample. Hence, this peak is not an effect of the coatings and is neglected in the following. A clear influence of the bias voltage is not observed in this depiction.

$\text{SiO}_x$  coatings deposited with such high gas-mixture ratios are very hard layers, because the molecular network consists of almost only silicon and oxygen, which build very strong bonds among themselves [51]. Hence, any kind of organic compounds ( $\text{CH}_x$  groups) is missing. The missing cross-linked network at existing  $\text{CH}_2$  groups gives the film a polymeric character. Therefore, these groups make the film more flexible. Hence, the molecular network is not as strongly tied as without these compounds. The effect is a more porous layer on the microscopic point of view. Because of the very weak IR activity of the  $\text{CH}_2$  bonds, the much more IR active  $\text{CH}_3$  groups are analyzed. This is justified by the correlation of their quantity with the one of the  $\text{CH}_2$  groups.



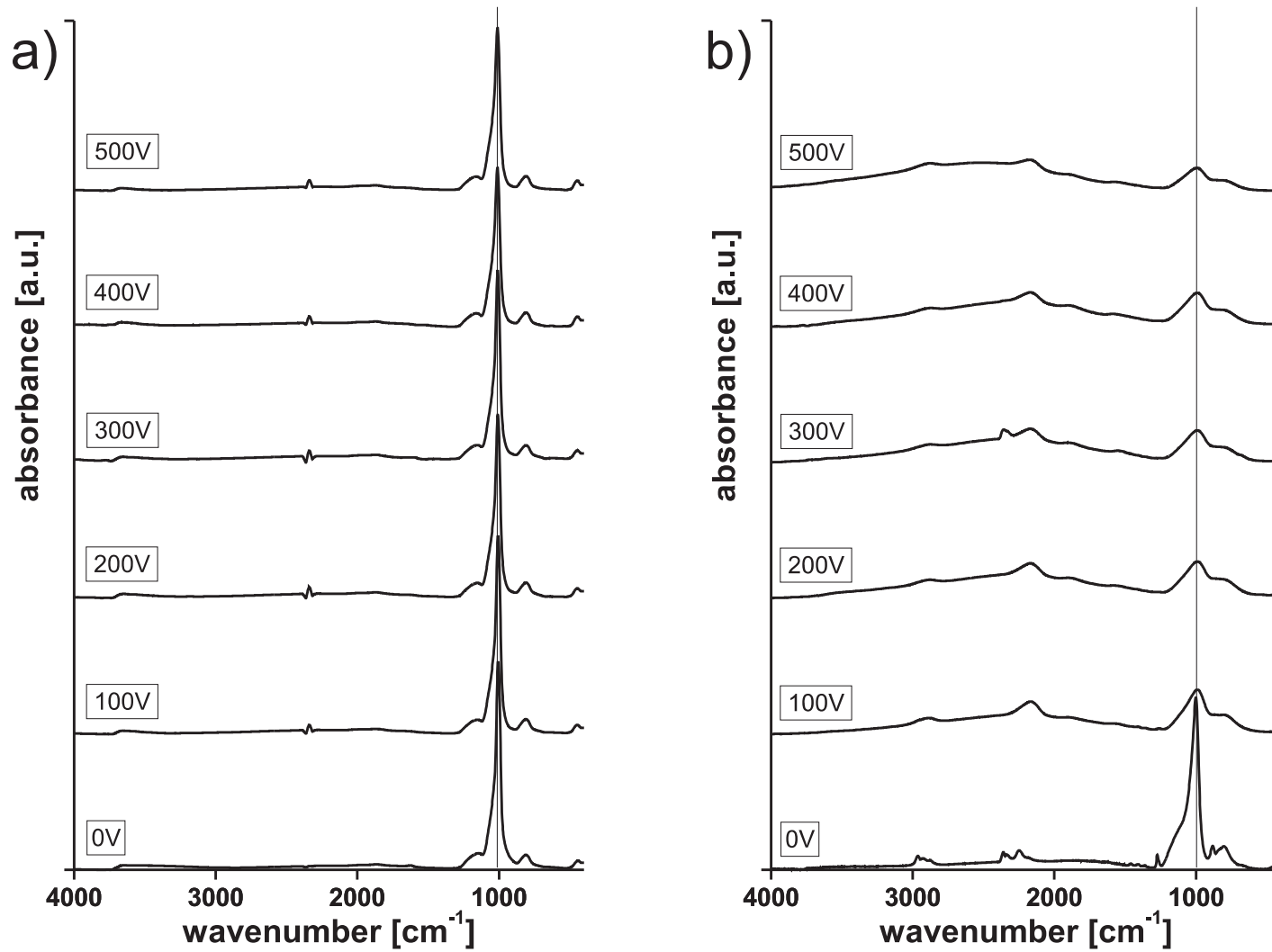


**Fig. 6.1:** Overview of FTIR spectra of  $\text{SiO}_x$  coatings deposited with a gas-mixture ratio of a)  $\text{HMDSO} : \text{O}_2 = 1 : 20$ , b)  $\text{HMDSO} : \text{O}_2 = 1 : 1$  with variable bias voltages in the range of 0 to 500 V in 100 V steps. Obviously, the bias influences mainly the organic compounds of the films.

wavenumber [ $\text{cm}^{-1}$ ]	corresponding molecular oscillation		reference
465	[Si-O]-Si	rocking vibration	[104]
812	[Si-O]-Si	asymmetric bending mode	[104, 105]
885	H-[Si-H]		[106]
930	[Si-O]-H	stretching mode	[105]
970	Si <sub>3</sub> -[Si-O]-SiO <sub>3</sub>	stretching mode, in-phase oxygen motion	[104]
1004	Si <sub>2</sub> O-[Si-O]-SiO <sub>3</sub>	stretching mode, in-phase oxygen motion	[104]
1038	SiO <sub>2</sub> -[Si-O]-SiO <sub>3</sub>	stretching mode, in-phase oxygen motion	[104]
1073	O <sub>3</sub> -[Si-O]-SiO <sub>3</sub>	stretching mode, in-phase oxygen motion	[104]
1100	[Si-O]-C		[107]
1150	[Si-O]-Si	stretching mode, out-of-phase oxygen motion	[104, 105]
1270	Si-[C-H <sub>x</sub> ]		[108]
3650	Si-[O-H]	stretching vibration of free OH groups	[103]

**Tab. 6.1:** Classification of the vibration modes observed in silicon-oxide films (Fig. 6.1)

To analyze the influence of the ion bombardment on possible organic compounds of the film,  $\text{SiO}_x$  coatings deposited with  $\text{HMDSO} : \text{O}_2 = 1 : 1$  are depicted in Fig. 6.1b in comparison to Fig. 6.1a. For  $U = 0 \text{ V}$ , the spectrum features a similar shape as the one in Fig. 6.1a. But in addition, further peaks occur: The peaks at about  $880$ ,  $2180$  and  $2250 \text{ cm}^{-1}$  correspond to  $[\text{Si-H}]$  vibrations. The single one at  $1270 \text{ cm}^{-1}$  and the triple one consisting of peaks at  $2875$ ,  $2930$  and  $2965 \text{ cm}^{-1}$  characterize  $\text{CH}_2$  and  $\text{CH}_3$  vibrations. The broad band in the range from  $1250$  to  $3500 \text{ cm}^{-1}$  is an interference, which superimposes the spectrum. In the spectra of this low gas-mixture ratio, a clear influence of the bias voltage is observed. The main  $[\text{Si-O}]$  peak decreases strongly with increasing voltage. A possible explanation for this decrease will be given later in this section. The organic compounds seem to vanish almost completely. The maximum change of the spectra occurs between the unbiased case and the bias voltage of  $100 \text{ V}$ . But a more precise analysis in this voltage range was not possible, because of the instability of the capacitive discharge with a driving voltage lower than  $100 \text{ V}$ . An overview of all oscillation peaks observed in Fig. 6.1 is given in Tab. 6.1.

To determine the modification of the molecular composition in detail, the separate peaks, each representing another kind of molecular oscillation, have to be analyzed. Each peak has a Gaussian form. Several of them can be superimposed, resulting in a band spectrum like the typical one of  $\text{SiO}_x$  films around  $1000 \text{ cm}^{-1}$ . By comparing the integrated band intensity of the particular peaks, information on the content of the corresponding compounds is obtained, because the integrated intensity gives the probability of the excitation of this oscillation and, therefore, of the number of existing bonds in the film.

The separate peaks, which can underlie the  $\text{SiO}_x$  spectrum in the wavenumber range of  $650$  to  $1300 \text{ cm}^{-1}$ , are listed in Tab. 6.1. Especially the four peaks at  $970$ ,  $1004$ ,  $1038$  and  $1073 \text{ cm}^{-1}$ , characterizing the same  $[\text{Si-O}]$  stretching mode but with different neighbors of the silicon atom, are of interest. The neighbors and next neighbors of the oxygen atom are assumed to be the same in all cases ( $\text{SiO}_3$ ), since the influence of the next neighbors on the oscillation frequency of the  $\text{SiO}$  vibration is weak. In stoichiometric silicon dioxide, the silicon is surrounded by four oxygen atoms. This is illustrated in Fig. 6.2a. The wavenumber of the corresponding  $[\text{Si-O}]$  stretching mode is  $1073 \text{ cm}^{-1}$ . With decreasing oxygen content of the film, the probability of this configuration drops and more and more silicon atoms are incorporated. This results in a replacement of the oxygen atoms by silicon atoms. Hence, the configurations shown in Fig. 6.2b-d become more likely. By substituting the oxygen atoms one after the other by silicon atoms with a lower electronegativity ( $1.9 \text{ eV}$ ) than oxygen ( $3.4 \text{ eV}$ ) [109], the  $[\text{Si-O}]$  bonding length is increased, which leads to a lower oscillation frequency. This  $[\text{Si-O}]$  vibration occurs in a  $\text{SiO}_{0.5}$  structure at a wavenumber of  $970 \text{ cm}^{-1}$ . In fact, all four configurations are possible with different probabilities. Hence, by an increasing amount of oxygen, the maximum of the resultant Si-O band shifts to higher wavenumbers. This shift is described in

Ref. [104, 110], the corresponding formula is given in Ref. [102]:

$$\bar{\nu} = 68.06x + 936.4 [\text{cm}^{-1}], \quad (6.1)$$

where  $x$  is the ratio of silicon to oxygen in the  $\text{SiO}_x$  structure. Thus, the ratio of the intensity of the discrete peaks and, therefore, the position of the maximum of the resultant main peak gives information on the oxygen content.

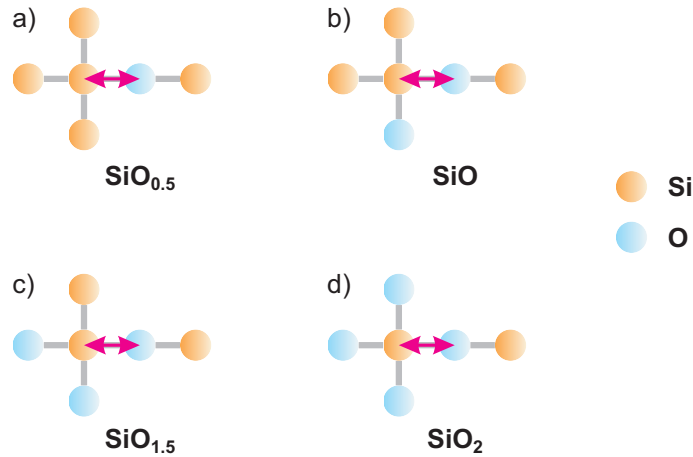


**Fig. 6.2:** Overview of four possibilities of the molecular structure and its influence on the [Si-O]-Si stretching mode: a)  $\text{SiO}_{0.5}$ ,  $\bar{\nu} = 970 \text{ cm}^{-1}$ , b)  $\text{SiO}$ ,  $\bar{\nu} = 1004 \text{ cm}^{-1}$ , c)  $\text{SiO}_{1.5}$ ,  $\bar{\nu} = 1038 \text{ cm}^{-1}$  and d) stoichiometric silicon oxide  $\text{SiO}_2$ ,  $\bar{\nu} = 1073 \text{ cm}^{-1}$  [104].

By fitting the experimental spectra of Fig. 6.1 in the range of  $650$  to  $1300 \text{ cm}^{-1}$  using the peaks from Tab. 6.1 in this wavenumber range, information of the oxygen and hydrogen content is obtained. The comparison of fitted and measured spectra as well as the individual Gaussian peaks, are depicted in Fig. 6.3 for the films deposited with  $\text{HMDSO} : \text{O}_2 = 1 : 1$ . The spectra were fitted by the controlling software [111] of the spectrometer, which uses the Levenberg-Marquardt algorithm [112].

The Gaussian peaks at  $1270 \text{ cm}^{-1}$ , characterizing the  $\text{Si}-[\text{C}-\text{H}_3]$  mode, vanishes completely in the coatings obtained with the substrate bias. This confirms the strong decrease of the  $\text{CH}_x$  triple peak at about  $2900 \text{ cm}^{-1}$ , which is observed in Fig. 6.1b. Consistently, the intensity of the  $\text{H}-[\text{Si}-\text{H}]$  peak at  $885 \text{ cm}^{-1}$  decreases with increasing bias voltage, too. The observed flattening of the characteristic band spectrum around  $1000 \text{ cm}^{-1}$  is due to a general decrease of the four peaks characterizing the [Si-O]-Si stretching vibration. To analyze a possible variation of the oxygen in the film, the intensities of these four peaks have to be compared.

The intensities are relative values depending on the absolute intensity detected by the spectrometer. Thus, a quantitative conclusion on the oxygen content in the different spectra is not possible. However, the ratio of the intensities of the peaks can be compared and a voltage-dependent characteristics of the particular intensity ratios can be determined. For both analyzed gas-mixture ratios, Fig. 6.4 depicts the

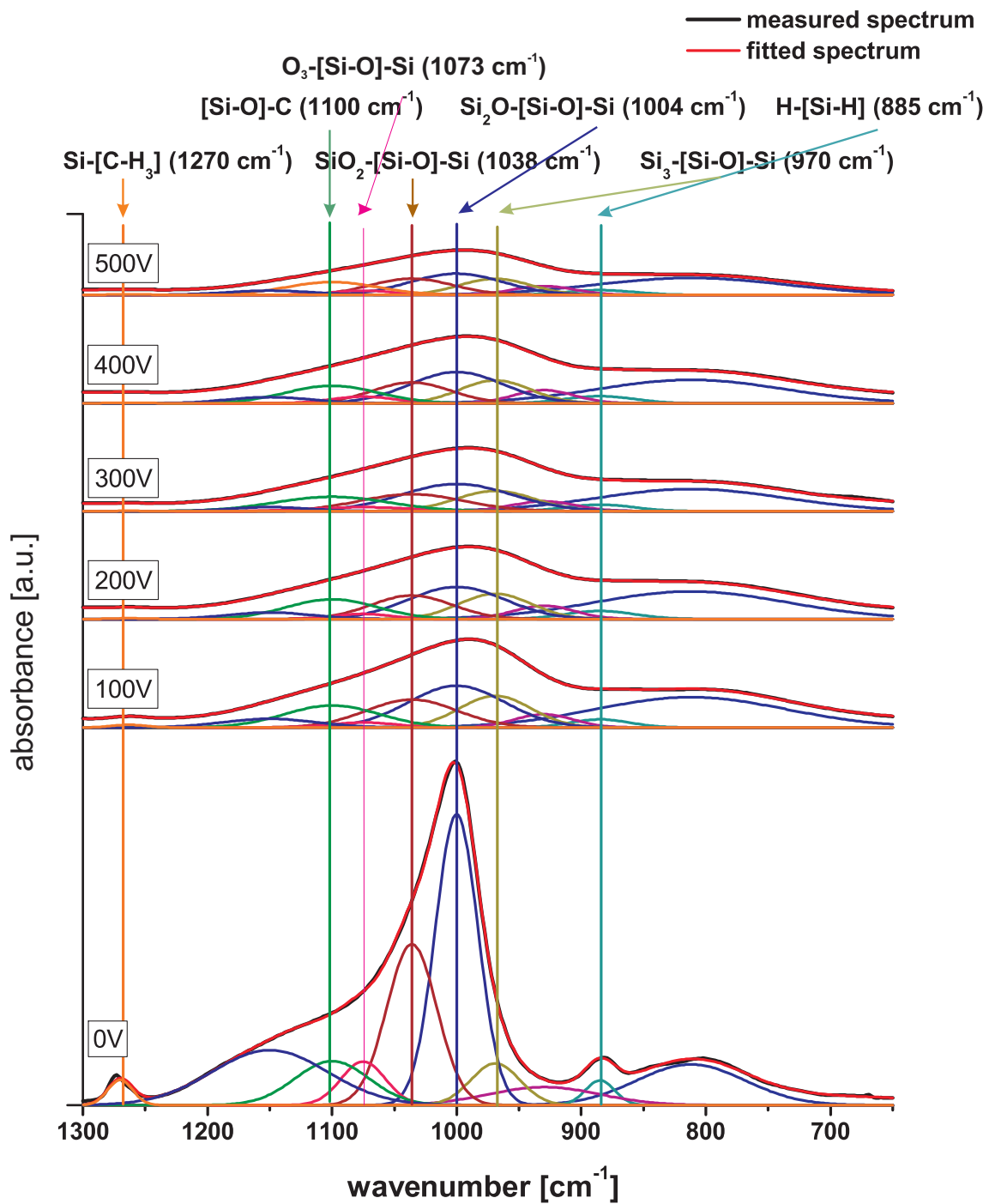


**Fig. 6.3:** Comparison of the fitted and measured spectra of the SiO<sub>x</sub> coatings deposited with HMDSO : O<sub>2</sub> = 1 : 1. The individual Gaussian peaks, which are used for the fit, are plotted, too.

integrated band intensities of the [Si-O]-Si peaks, normalized to the sum of their intensities for both analyzed gas-mixture ratios.

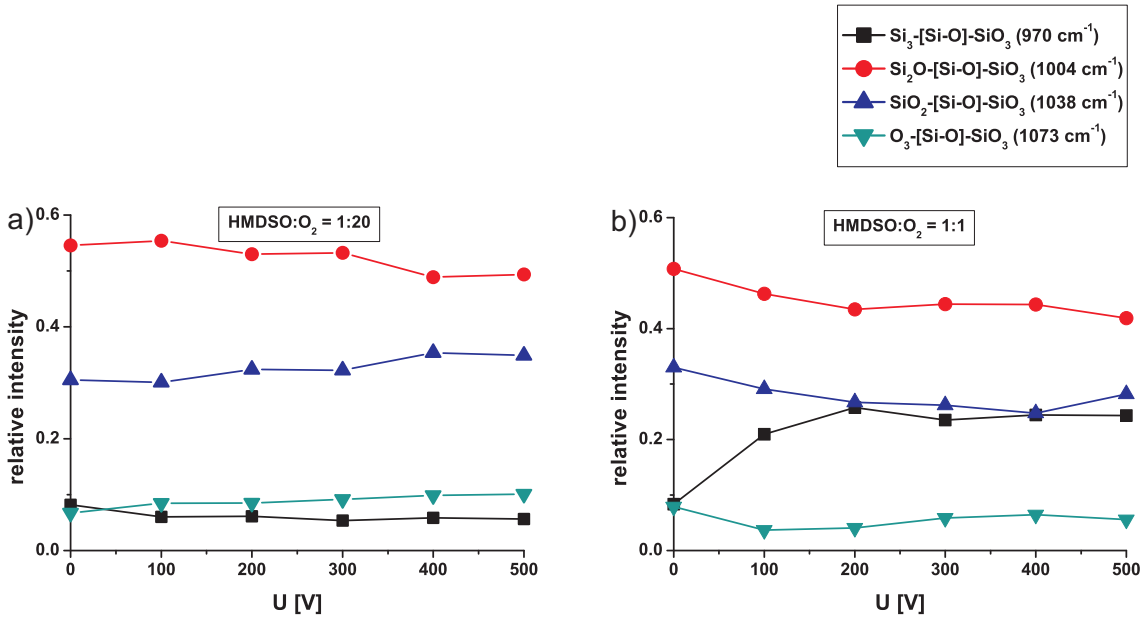


**Fig. 6.4:** Relative integrated band intensities of the peaks corresponding to the [Si-O] stretching vibration, defining the different neighbors of the silicon atom, in dependence of the bias voltage. Their intensities are normalized to the total intensity of the four Gaussian peaks.

Regarding the situation for HMDSO : O<sub>2</sub> = 1 : 20 in Fig. 6.4a, the intensities of the Si<sub>3</sub>-[Si-O]-Si and Si<sub>2</sub>O-[Si-O]-Si peaks decrease slightly with increasing bias voltage. The ones of the SiO<sub>2</sub>-[Si-O]-SiO and SiO<sub>3</sub>-[Si-O]-Si band increase. This is equivalent to a decrease of SiO<sub>0.5</sub> and SiO structures and an increase of SiO<sub>1.5</sub> and SiO<sub>2</sub> structures, which leads to a shift of the resultant [Si-O]-Si peak to higher wavenumbers. The augmented inclusion of oxygen in the film is caused by the energetic oxygen ions, which penetrate the film surface and can be embedded into the coating.

In contrast to the characteristics of the [Si-O]-Si intensities of the higher mixture ratio, the ones of HMDSO : O<sub>2</sub> = 1 : 1 show different properties in Fig. 6.4b. The strong increase of SiO<sub>0.5</sub> components and the slight decrease of the other three ones is accompanied by a shift to lower wavenumbers and, therefore, a reduced incorporation of oxygen. This leads to a possible explanation of the strong intensity decrease of the [Si-O] peak, which was pointed out on the basis of Fig. 6.1b: Due to the reduction of the oxygen content, the probability of pure [Si-Si] bonds increases. But these bonds are IR inactive. Hence, they cannot be detected in the analyzed spectra. The hypothesis could be verified by Raman spectroscopy, because this bond is Raman active. But this analysis technique was not available during this work.

To explain the decrease of the oxygen content, the characteristics of the organic

compounds with increasing bias have to be taken into account. As can be seen in Fig. 6.3, the  $[\text{C-H}_x]$  oscillations vanish almost completely with increasing voltage and similarly, the  $[\text{Si-O}]\text{-H}$  vibration. A possible explanation is the breaking of the  $[\text{C-H}]$  bonds by the impinging  $\text{O}^+$  ions: OH groups can leave the film and the carbon remains in the molecular network, which is dissolved by the high-energetic ions, too, leading to a loss of CO groups as well. This is confirmed by the decrease of the intensity of the  $[\text{Si-O}]\text{-C}$  vibration in Fig. 6.3. Because of the low amount of oxygen compared to silicon at this composition, only few oxygen atoms are left to be embedded in the film. The result is an opposite shift of the  $[\text{Si-O}]$  peak compared to the higher gas-mixture ratio.

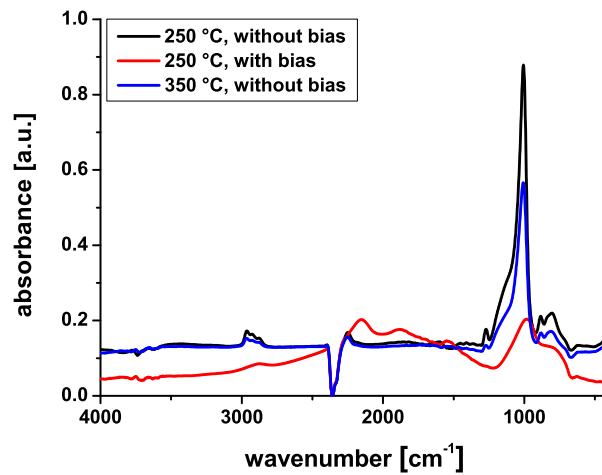


**Fig. 6.5:** Influence of the substrate temperature on the molecular composition of  $\text{SiO}_x$  coatings exemplarily shown for  $\text{HMDSO} : \text{O}_2 = 1 : 1$ . The modification of the IR spectra with the substrate bias applied is not a temperature effect.

The strong ion bombardment at high bias voltages also changes the substrate temperature (see section 3.2.1). To rule out an influence of the increasing temperature on the modification of the IR spectra, those of a film deposited with  $\text{HMDSO} : \text{O}_2 = 1 : 1$  at  $250\text{ °C}$  without bias,  $350\text{ °C}$  without bias and  $250\text{ °C}$  with bias are compared in Fig. 6.5. Both unbiased coatings show comparable results, but the biased one differs strongly. In conclusion, the modifications of the IR spectra described above are the result of the ion bombardment, not of the increase of the substrate temperature.

### 6.1.2 Silicon nitride

In a way analog to the  $\text{SiO}_x$  coatings, the influence of the ion bombardment on the molecular structure of the  $\text{SiN}_y$  films is analyzed for the case of two different gas-mixture ratios of  $\text{SiH}_4$  and  $\text{NH}_3$ . The comparison of the IR spectra of the films



deposited with varying bias voltages is depicted in Fig. 6.6. For  $U = 100$  V, the films flaked off and could not be analyzed.

All spectra show the typical band structure of silicon nitride. The main peak at  $800\text{ cm}^{-1}$  is accompanied by a very low one at approximately  $495\text{ cm}^{-1}$ , both related to [Si-N] oscillations. The main peak shows a broad shoulder towards higher wavenumbers. This is due to a [N-H] vibration at  $1190\text{ cm}^{-1}$ , which is related to the second [N-H] oscillation band at  $3340\text{ cm}^{-1}$ . The weak peak at  $1550\text{ cm}^{-1}$  corresponds to a H-[N-H] vibration. Additionally, the [Si-H] band at about  $2200\text{ cm}^{-1}$  is observed. Like in the spectra of the  $\text{SiO}_x$  films, the  $\text{CO}_2$  double peak occurs. The underlying broad band again is due to an interference.

For both gas-mixture ratios, a shift of the main peak to higher wavenumbers with applied substrate bias is noticeable, but the shift does not change further with increasing bias voltage. This shift indicates an increased incorporation of hydrogen and/or nitrogen into the film [63, 114]. However, the expected shift of the SiH peak at  $2200\text{ cm}^{-1}$  to higher wavenumbers, which comes along with an increased incorporation of nitrogen [117, 119], is not observed. As for  $\text{SiO}_x$  coatings, the shift of the band spectrum is related to changes of the intensities of the single peaks: The SiN band at  $800\text{ cm}^{-1}$  was determined to be a superposition of four Gaussian peaks, each characterizing the [Si-N] asymmetric stretching mode, but with different neighbors, and two Gaussian peaks resulting from a [Si-H] ( $690\text{ cm}^{-1}$ ) and a [N-H] bending mode ( $1190\text{ cm}^{-1}$ ) [116]. The SiH peak at approximately  $2200\text{ cm}^{-1}$  results from a superposition of four Gaussian peaks, which all correspond to the [Si-H] stretching mode, but with different neighbors [117, 118]. The properties of this peak was analyzed in detail in Ref. [63]. All oscillations, which describe the spectra of Fig. 6.6, are listed in Tab. 6.2.

The shifted SiN peak is analyzed in more detail by the decomposition into its components. The different possibilities of neighbors to the [Si-N] bond, which are taken into account for fitting the spectra, are illustrated in Fig. 6.7. The oscillation in a stoichiometric silicon nitride ( $\text{Si}_3\text{N}_4$ ) is depicted in Fig. 6.7a. whereas all neighbors are silicon atoms. The oscillation frequency corresponds to  $780\text{ cm}^{-1}$ . By substituting one direct neighbor by a hydrogen atom, which offers a higher electronegativity compared to silicon (Si: 1.9 eV, H: 2.2 eV [109]), it results in a smaller bonding length and, therefore, in a higher wavenumber ( $\bar{\nu} = 820\text{ cm}^{-1}$ , Fig. 6.7b). By replacing the silicon atom by nitrogen with an electronegativity of 3 eV instead of hydrogen, the oscillation frequency and, therefore, the wavenumber increases further to  $\bar{\nu} = 866\text{ cm}^{-1}$  (Fig. 6.7c). In the case of Fig. 6.7d with a hydrogen and a nitrogen atom as neighbors of the [Si-N] bond, the consequence is the highest wavenumber of  $\bar{\nu} = 1000\text{ cm}^{-1}$ .

The fitted spectra of the  $\text{SiN}_y$  coatings deposited with  $\text{SiH}_4 : \text{NH}_3 = 1 : 3$  and the considered Gaussian peaks are depicted in Fig. 6.8 in the wavenumber range from  $450$  to  $1350\text{ cm}^{-1}$ . A clear decrease in the intensity of the stoichiometric [Si-N] peak ( $\text{Si}_3$ -[Si-N]- $\text{Si}_2$ ) with increasing bias voltage is observed in contrast to the increase of the [N-Si]-SiNH oscillation. In addition, a decrease of the  $\text{Si}_3$ -[Si-H] peak at  $690\text{ cm}^{-1}$

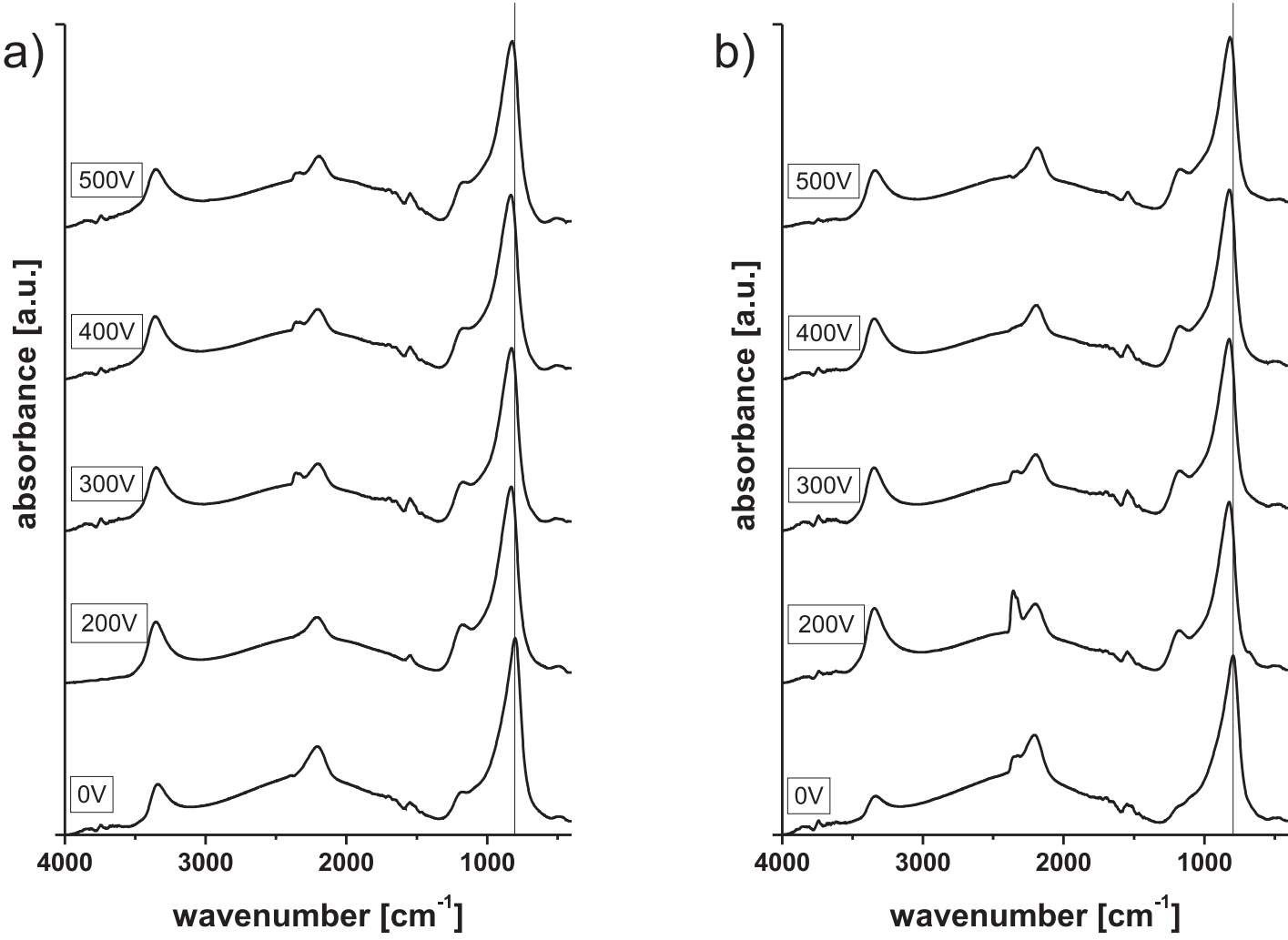


**Fig. 6.6:** Overview of FTIR spectra of SiN<sub>y</sub> coatings deposited with a gas-mixture ratio of a) SiH<sub>4</sub> : H<sub>3</sub> = 3 : 22, b) SiH<sub>4</sub> : NH<sub>3</sub> = 1 : 3 with variable bias voltages in the range of 0 to 500 V in 100 V steps. The bias voltage influences the H and N content of the films.

wavenumber [cm <sup>-1</sup> ]	corresponding molecular oscillation		reference
495	[Si-N]-Si <sub>2</sub>	breathing mode	[113, 114, 115, 116]
690	Si <sub>3</sub> -[Si-H]	bending mode	[114, 116]
780	Si <sub>3</sub> -[Si-N]-Si <sub>2</sub>	asymmetric stretching mode	[114, 117]
820	[N-Si]-Si <sub>2</sub> H	asymmetric stretching mode	[117, 116]
866	Si <sub>3</sub> -[Si-N]-SiN	asymmetric stretching mode	[116]
1000	[N-Si]-NHSi	asymmetric stretching vibration	[116]
1104	[Si-O]-Si	stretching mode, in-phase oxygen motion	[104]
1190	Si <sub>2</sub> -[N-H]	bending mode	[116]
1550	H-[N-H]	bending mode	[116, 114, 118]
2010	Si <sub>3</sub> -[Si-H]	stretching mode	[118, 117]
2115	Si <sub>3</sub> N <sub>4</sub> -[Si-H]	stretching mode	[118, 117]
2180	[H-Si]-Si <sub>2</sub> N	stretching mode	[118, 117]
2250	[H-Si]-N <sub>3</sub>	stretching mode in voids	[118, 117]
3340	Si <sub>2</sub> -[N-H]	stretching mode	[118]

**Tab. 6.2:** Classification of the vibration modes observed in silicon-nitride films (Fig. 6.6).

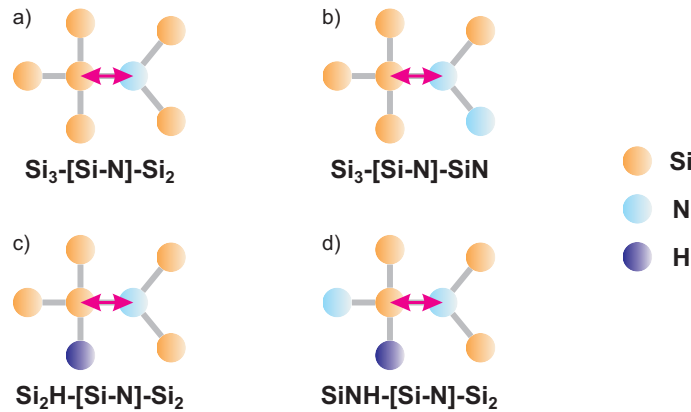


**Fig. 6.7:** Overview of four possibilities of the molecular structure and its influence on the [Si-N] asymmetric stretching mode: a) stoichiometric silicon nitride  $\text{Si}_3\text{N}_4$ ,  $\bar{\nu} = 780 \text{ cm}^{-1}$ , b) one silicon atom is substituted by a hydrogen atom,  $\bar{\nu} = 820 \text{ cm}^{-1}$ , c) one silicon atom is substituted by a nitrogen atom,  $\bar{\nu} = 866 \text{ cm}^{-1}$  and d) two silicon atoms are substituted by a hydrogen and a nitrogen atom,  $\bar{\nu} = 1000 \text{ cm}^{-1}$

occurs as well as a decrease of the [Si-O]-Si peak at  $1104 \text{ cm}^{-1}$ , which results from a diminished incorporation of oxygen into the film with increasing bias voltage.

Because of the dependence of the integrated band intensity of the particular peaks on the absolute intensity detected by the spectrometer, the intensities have to be normalized like for the  $\text{SiO}_x$  films to obtain reliable intensity characteristics of the particular Gaussian peaks. Their characteristics in dependence of the bias voltage is depicted in Fig. 6.9 for the layer deposited with  $\text{SiH}_4 : \text{NH}_3 = 1 : 3$  as well as with  $\text{SiH}_4 : \text{NH}_3 = 3 : 22$ .

The trends of the intensities for both gas-mixture ratios are similar. The intensities of the oscillations at  $780$ ,  $820$  and  $866 \text{ cm}^{-1}$  decrease, and only the intensity of the [N-Si]-NHSi vibrations increases with increasing bias voltage. This is due to an increased incorporation of hydrogen and nitrogen atoms in the film through the bombardment by hydrogen and nitrogen ions: Thus, the probability of stoichiometric SiN structures becomes lower and the [Si-N] bonds have mainly one nitrogen or hydrogen as neighbor. The occurrence of a nitrogen and a hydrogen atom in the neighborhood of one [Si-N] bond increases. The higher probability of [N-Si]-NHSi and the lower one of [N-Si]- $\text{Si}_2\text{H}$  oscillations indicates a higher incorporation of N and H in the case of  $\text{SiH}_4 : \text{NH}_3 = 3 : 22$ . Generally, the number of [Si-N] vibrations in the stoichiometric vicinity is the lowest, followed by the one with one bonded hydrogen atom instead of silicon. The probabilities of the  $\text{Si}_3\text{-[Si-N]-SiN}$  and [N-Si]-NHSi structures cross in the range of 200 to 300 V. Hence, the compound occurring most in the biased case is [N-Si]-NHSi.

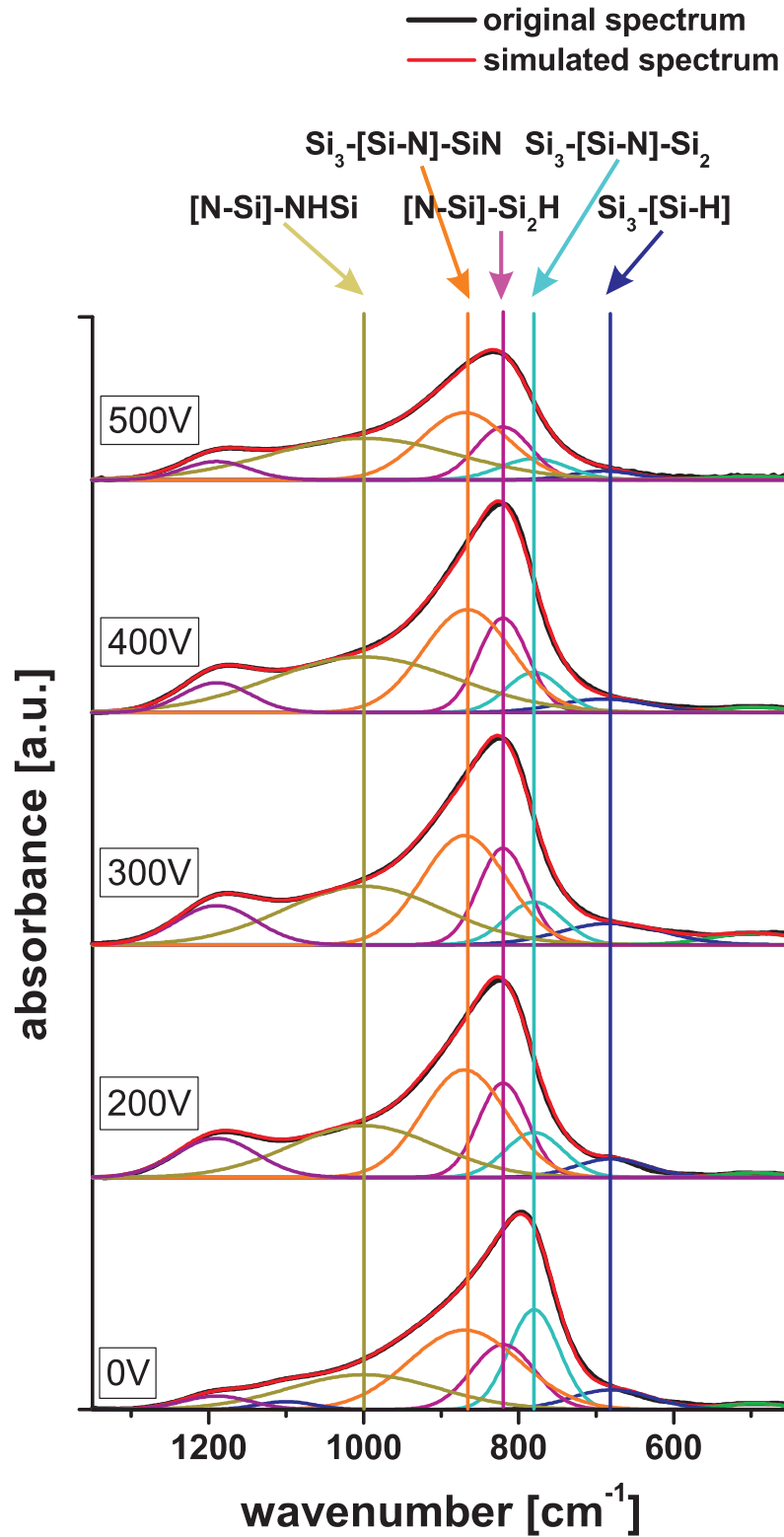


**Fig. 6.8:** Comparison of the fitted and measured spectra of the  $\text{SiN}_y$  coatings deposited with  $\text{SiH}_4 : \text{NH}_3 = 1 : 3$  (same representation as in Fig. 6.3).

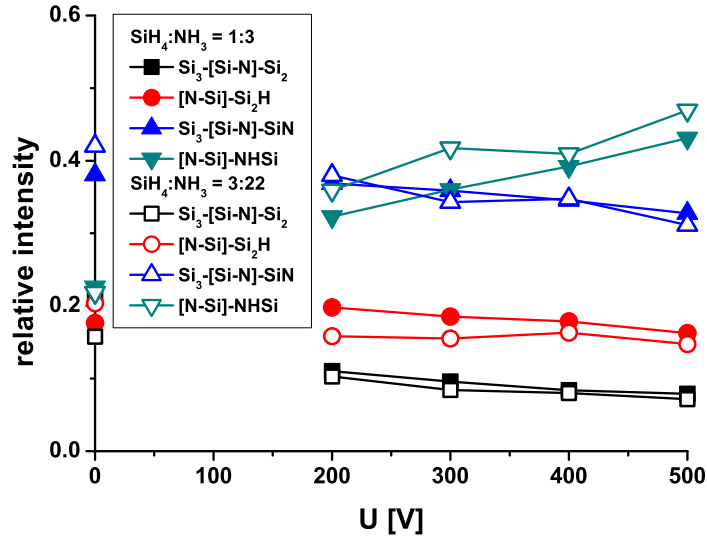


**Fig. 6.9:** Relative integrated band intensity of the particular peaks corresponding to the [Si-N] asymmetric stretching vibration, defining the different neighbors of the silicon atom. Their intensities are normalized to the total intensity of the four Gaussian peaks.

## 6.2 Refractive index

A modification of the molecular composition of a coating should be reflected in a variation of the refractive index. Therefore, the refractive index was analyzed in dependence of the bias voltage. This was done separately for the silicon-oxide and silicone-nitride coatings for three different gas-mixture ratios. The refractive index was determined by the method described in section 3.3.2 for the wavelength of 589 nm.

The results for the SiO<sub>x</sub> coatings are depicted in Fig. 6.10 for the gas-mixture ratios of HMDSO : O<sub>2</sub> = 1 : 1, 1 : 5 and 1 : 20. For  $U = 0$  V, a slight decrease from  $N = 1.50$  to 1.41 is observed with increasing gas-mixture ratio, which is due to the increasing content of oxygen in the deposited film. It is well-known that the refractive index increases with decreasing oxygen content. The refractive index of stoichiometric silicon dioxide, deposited with HMDSO : O<sub>2</sub> = 1 : 20 agrees well with the literature value of  $N = 1.46$  [101].

With increasing bias voltage, a clear increase of the refractive index is observed for all three gas-mixture ratios. For HMDSO : O<sub>2</sub> = 1 : 1, this increase is most pronounced. At  $U = 500$  V, it is  $N = 1.93$ . The different slope at the particular mixture ratios can be explained by the different chemical reactions occurring, which were described in section 6.1.1: At HMDSO : O<sub>2</sub> = 1 : 1, these reactions lead to a reduction of the oxygen in the deposited layer in the biased case. At the same time, the amount of organic components is reduced as well. Moreover, an increase of the

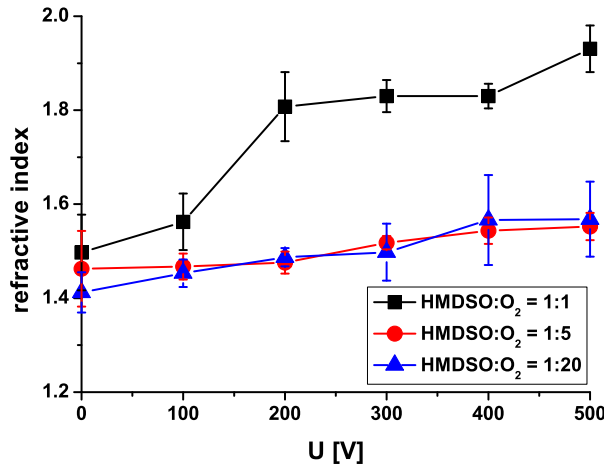


**Fig. 6.10:** Refractive index of SiO<sub>x</sub> coatings as function of the bias voltage for three different gas-mixture ratios: HMDSO : O<sub>2</sub> = 1 : 1, 1 : 5 and 1 : 20.

refractive index indicates a denser film. Hence, the molecular network is tied more strongly and/or the bonding lengths are decreased. The molecular structure features long chains without any faults like Si-H or C-H groups since hydrogen, which cannot assume a second bond, is missing. The higher the number of bonds per atom the denser the film.

In the case of the other two gas-mixture ratios, the refractive index only shows a slight increase up to  $N = 1.57$ . They basically agree within the error bars. This agreement indicates the higher incorporation of oxygen in the film, which is described in section 6.1.1 and seems to be saturated in both cases. Ab initio, the layers deposited with HMDSO : O<sub>2</sub> = 1 : 20 contain very few CH<sub>x</sub> groups. Thus, a further reduction of these compounds is not noticeable. For HMDSO : O<sub>2</sub> = 1 : 5, the amount of the organic compounds is reduced during biasing (section 6.1.1) such that the molecular structure becomes similar to that of HMDSO : O<sub>2</sub> = 1 : 20. The increasing difference of the refractive indices of these two gas-mixture ratios and that of HMDSO : O<sub>2</sub> = 1 : 1 is attributed to the higher incorporation of oxygen in the first and its reduced incorporation in the latter case.

The same analyses were done for silicon-nitride films deposited in gas-mixture ratios of SiH<sub>4</sub> : NH<sub>3</sub> = 1 : 1, 1 : 3 and 3 : 22. This is illustrated in Fig. 6.11. In the unbiased case, the refractive index decreases from  $N = 2.57$  to 1.99 with increasing gas-mixture ratio. The value of stoichiometric silicon nitride found in literature is  $N = 1.9$  [120]. The similarity of the refractive index of the layers deposited with SiH<sub>4</sub> : NH<sub>3</sub> = 3 : 22 and the reference value from literature confirms the deposition of nearly stoichiometric silicon nitride.

The refractive index of the film deposited with SiH<sub>4</sub> : NH<sub>3</sub> = 1 : 1 can be regarded as independent of the bias voltage. This can be explained by the very low



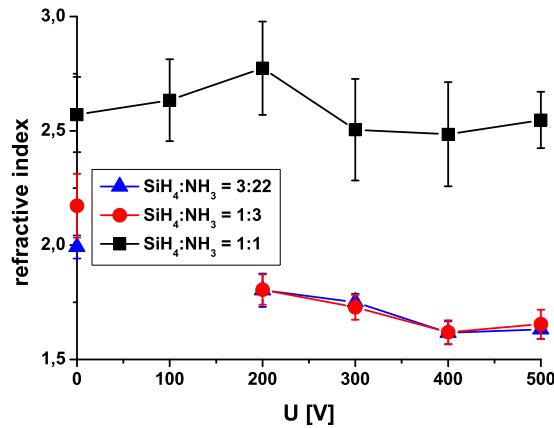


**Fig. 6.11:** Characteristics of the refractive index of  $\text{SiN}_y$  coatings in dependence of the bias voltage for three different gas-mixture ratios:  $\text{SiH}_4 : \text{NH}_3 = 1 : 1$ ,  $1 : 3$  and  $3 : 22$ .

ratio of nitrogen compared to silicon. Thus, the effect of impinging nitrogen ions on the molecular structure is mostly insignificant. The strong scatter of the values is attributed to the very low total thickness of these layers at the chosen optical thickness, which makes the measurements prone to unevenness. This is reflected in the large error bars.

For  $\text{SiH}_4 : \text{NH}_3 = 1 : 3$  and  $3 : 22$ , the refraction indices are comparable. They decrease to  $N = 1.64$  with increasing bias voltage, which indicates a looser layer structure. The augmented integration of nitrogen and hydrogen leads to fewer bonds between the single atoms and, therefore, to a more porous structure, which results in a lower refractive index. These films have a hyperstoichiometric structure. These results are consistent with the results obtained in section 6.1.2.

## 6.3 Conclusion

The influence of the ion bombardment on the molecular composition of  $\text{SiO}_x$  and  $\text{SiN}_y$  films was analyzed on the basis of their IR spectra. In case of  $\text{SiO}_x$  films, less organic compounds like  $\text{CH}_x$  and accompanying SiH groups are incorporated, which leads to a more strongly connected network structure of the film when the bias is applied. Moreover, the oxygen content increases, most notably in films deposited with a low ratio of HMDSO to  $\text{O}_2$ . Hence, due to the more strongly connected network structure, the biased films offer less porosity, which should be reflected in better diffusion-preventing and insulating properties. This is consistent with the results of section 4.4.1, where the resistance of the biased films was clearly higher than the one of the unbiased films. As a consequence, coatings with a comparable molecular structure can be deposited with a lower gas-mixture ratio, which offers a higher deposition rate, thus the process becomes more effective, by applying a

substrate bias. Vice versa, the substrate bias does not have a significant influence on the molecular structure of the  $\text{SiO}_x$  coatings deposited with  $\text{HMDSO} : \text{O}_2 = 1 : 20$ , which is the most important mixture ratio for producing barrier layers.

For  $\text{SiN}_y$  films, the bias leads to an increased content of nitrogen and hydrogen and a more porous molecular structure. Therefore, the insulating and especially the diffusion-preventing properties of these coatings should become worse. However, the insulating properties could not be confirmed by resistance measurements because of the bad adhesion of the biased layers. A suitable balance between melting of the layer surface and incorporation of additional nitrogen and hydrogen may be found to obtain satisfying barrier properties.

The characteristics of the refraction indices with the bias voltage is consistent with the results for the IR spectra: The stronger bonds in the network structure and, therefore, the higher density of the  $\text{SiO}_x$  films is reflected in the increase of the refractive index with increasing voltage. The augmented incorporation of nitrogen and hydrogen and, consequently, the smaller density of the  $\text{SiN}_y$  layer leads to the decrease of the refractive index of these films. These film properties are of main interest for optical applications.

# Chapter 7

## Summary and conclusions

The topic of this thesis was the optimization of barrier layers, which are qualified for fabricating CIGS solar cells on flexible steel substrates with a rough surface. Parts of the presented results were obtained in the context of the publicly funded BMBF project "FlexNet". To produce barrier coatings, silicon oxide ( $\text{SiO}_x$ ) and silicon nitride ( $\text{SiN}_y$ ) were deposited in a microwave-PECVD process in the Plasmodul setup. The optimization was done on the basis of bombarding the growing layer with energetic ions created by a modulated substrate bias. The bias leads to a capacitive discharge, which superimposes the microwave plasma. This way, the particle flux and the energy of the ions impinging on the substrate could be controlled independently. For the specific manipulation of the barrier-layer properties, a detailed analysis of the layer-growth mechanisms was carried out.

For good barrier properties, the development of pinholes in the coating has to be avoided. These defects mainly appear at positions of notches on the substrate surface. Hence, the layer growth at such positions had to be analyzed to explain the formation of pinholes and find solutions for avoiding them. This was done on the basis of model substrates with a well-defined trench surface structure in the  $\mu\text{m}$  range. Their breaking edge was investigated in a scanning electron microscope. Hence, the profile of the deposited layer could be analyzed. The homogeneity of the coating was evaluated by geometrical characteristics and the influence of the particular bias parameters – voltage amplitude  $U$ , frequency  $f$  and ratio of positive to negative pulse  $p_w$  – on the layer profile was determined. An increase of the homogeneity with an increase in the bias voltage and frequency was observed. An influence of the pulse width was not detected. Within the limit of the used setup, the optimum bias parameters were  $U = 500 \text{ V}$ ,  $f = 250 \text{ kHz}$  and  $p_w = 35 \%$  and, hence, chosen for further analyses.

The differences in biased and unbiased coatings were analyzed in more detail and it turned out that without bias, the layer tends to close above the cavities from both sides, but cracks remain at the closure positions. By biasing the substrate, however, a smoothing of the layer edges above the cavities occurred. Thus, the cavities remained open for a longer time, and as a consequence, a more homogeneous coating

of the notches is obtained. This effect can be explained by the enhanced surface mobility of the layer-forming particles caused by the bombardment of energetic ions as well as by a sputter process induced by the impinge of these ions. Due to the increased energy input, the coating finally merges completely over voids without remaining cracks, which indicates improved barrier properties of the deposited films. In similar analyses, this merging was also verified on steel substrates, which are industrially relevant for solar cell production.

The layer growth was examined separately for  $\text{SiO}_x$  and  $\text{SiN}_y$  coatings, which were deposited with specific gas-mixture ratios of HMDSO to oxygen and monosilane to ammonia, respectively. Thereby, the substrate bias led to a more pronounced change in the layer profile of  $\text{SiO}_x$  films. This can be attributed to the higher amount of ions than of layer-forming radicals in the case of  $\text{SiO}_x$  layers compared to  $\text{SiN}_y$  films.

Improved insulation properties of the barrier layers were proved by resistance and breakdown-voltage measurements of the coatings. Here, the biased layers – especially after the CIGS process – offered a clearly higher resistance than the unbiased ones. These analyses were mainly done on the basis of the  $\text{SiO}_x$  layers, because the  $\text{SiN}_y$  films showed very bad adhesion after the CIGS process. Without bias and before the CIGS process, the  $\text{SiN}_y$  coatings offered better insulating properties than the  $\text{SiO}_x$  layers. The layer-forming particles generated by monosilane have a naturally higher surface mobility than those created by HMDSO. With bias, however, the insulation properties of  $\text{SiO}_x$  and  $\text{SiN}_y$  films become comparable.

The processes, which lead to different profiles of the biased and unbiased layers at positions of indentations on the substrate surface, were determined by detailed analyses of the local layer-forming mechanisms like the loss of particles, sputtering and redeposition at the film surface. These analyses were carried out by means of numerical simulations using the Monte-Carlo Code SDTrimSP-2D. Compared to former simulation codes, this one offers the possibility of including the impacting high-energetic ions in the process on the substrate surface and, therewith, indirectly the effect of the substrate bias.

To adapt the code as close as possible to the realistic conditions in the experiments, the input parameters like the layer density, hydrogen content, growing rate, ion energy and particle flux on the substrate had to be determined, and the plasma was characterized by means of Langmuir double-probe measurements. As essential parameters, the electron density and temperature were determined in the region between the microwave plasma source and the substrate holder in the Plasmodul for different bias voltages in a nitrogen reference discharge. Density and temperature profiles were found to decay from  $n_e = 3 \cdot 10^{17} \text{ m}^{-3}$  and  $T_e = 3.6 \text{ eV}$ , in front of the microwave plasma source to  $n_e = 6 \cdot 10^{15} \text{ m}^{-3}$  and  $T_e = 0.6 \text{ eV}$  in front of the substrate holder, respectively. Biasing leads to a slight increase of the density and decrease of the temperature in the whole plasma. Since chemical reactions are not implemented in the SDTrimSP-2D code, simulations of a-Si:H (hydrogenated amorphous silicon) layer depositions were carried out in a pure monosilane plasma

---

acting as model system, in which chemical reactions can be neglected. The trench structure of the model substrates from the experiment served as "model cavities".

For both, biased and unbiased depositions, simulation and experimental results on the profiles of the coatings were found to be in very good agreement. Hence, the simulation gives reliable information on the layer-growth mechanisms. Furthermore, it could be shown that the particular local growth processes, namely the loss, the sputtering and the redeposition on the film surface, are not affected by the deposited radicals, which only determines the total deposition rate, but by the impinging energetic ions. The radicals strike the substrate only with thermal energy and, hence, they do not contribute to the increased mobility. Their deposition profile is explained by the geometry of the substrate and the angular distribution of the incoming particles. Thus, the impacting ions could be identified to play the key role in the layer-forming process in biased depositions.

The ion impact takes the strongest effect at the upper edge of the flanks where the particle loss is highest. A part of the lost particles are redeposited further inside the trench. Therefore, the position of the layer closure above the cavity is drawn deeper inside the trench. The observed increase of the layer thickness inside the notches is mainly caused by redeposition of particles extracted from the top edges of the trench. Thus, the resulting profile form can be traced back to the detailed sputter and redeposition processes. The mechanisms, which lead to the mergence of cracks, are not covered by the code and might rather be due to chemical processes.

The molecular composition and structure, which determine the adhesion, flexibility and diffusion properties of the deposited barrier layers, were analyzed by means of FTIR spectroscopy. As well, this was done separately for the  $\text{SiO}_x$  and the  $\text{SiN}_y$  layers. In the case of the  $\text{SiO}_x$  coatings, a reduced incorporation of organic compounds like  $\text{CH}_x$  and  $\text{SiH}$  groups in the Si-O-Si network structure was detected with increasing bias voltage. Additionally, a slight increase of the oxygen content in the layers was found, which is most notable for films deposited in a high gas-mixture ratio of HMDSO and oxygen. Due to the decrease of the organic compounds, the resultant network structure is more strongly connected. The film is less porous, which leads to a denser and harder layer compared to the unbiased one. This result is verified by measurements of the refractive index, which increased with the bias voltage. The  $\text{SiN}_y$  films showed an increased content of hydrogen and nitrogen with increasing bias. This leads to a more porous structure as reflected in a decrease of the refraction index. The results from FTIR spectroscopy and refractive-index measurements indicate that biased  $\text{SiO}_x$  coatings gain and  $\text{SiN}_y$  coatings rather lose diffusion-preventing properties.

In conclusion, the impact of energetic ions on the growing layer is understood in terms of sputter and redeposition processes. A clear improvement of the barrier properties of silicon-oxide coatings is achieved in biased depositions. The improvement was sufficient to produce CIGS solar cells on flexible steel foil. The record efficiency achieved was 11.5%. For comparison, the CIGS solar moduls available on glass substrates offer an efficiency of 10 – 12%. Better results may be obtained under cleanroom conditions.

# Bibliography

- [1] F. Kessler, D. Herrmann, and M. Powalla, *Approaches to flexible CIGS thin-film solar cells*, Thin Solid Films **480–481**, 491 (2004).
- [2] W. Diehl, V. Sittinger, and B. Szyszka, *Thin film solar cell technology in Germany*, Surf. Coat. Technol. **193**, 329 (2005).
- [3] P. Jackson *et al.*, *New world record efficiency for Cu(In,Ga)Se<sub>2</sub> thin-film solar cells beyond 20%*, Prog. Photovolt. Res. Appl. (2011).
- [4] GermanPatent, *DE 197 39894.4-33*, .
- [5] M. Niinomi, H. Kobayashi, A. Bell, and M. Shen, *The Effects of Substrate Surface Roughness on the Morphology of Plasma-Polymerized Ethylene*, J. Appl. Phys. **44**, 4317 (1973).
- [6] M. Niinomi, H. Kobayashi, A. Bell, and M. Shen, *The Effects of Substrate Surface Roughness on the Morphology of Plasma-Polymerized Ethylene*, Journal of Applied Polymer Science **18**, 2199 (1974).
- [7] W. Michaeli, I. Fontainer, T. Jüntgen, and E. Jansen, *Investigations on the layer growth of plasma polymerized HMDSO coatings on micro-structured polycarbonate (PC) samples*, Macromol. Mater. Eng. **280–281**, 26 (2000).
- [8] C. Chang, T. Abe, and M. Esashi, *Trench filling characteristics of low stress TEOS/ozone oxide deposited by PECVD and SACVD*, Microsystem Technologies **10**, 97 (2004).
- [9] A. Mutzke and R. Schneider, *SDTrimSP-2D: Simulation of Particles Bombarding on a Two Dimensional Target, Version 1.0*, IPP-Report **12/4**, (2009).
- [10] I. Brodie, *Calculation of Deposition Uniformity in rf Sputtering*, J. Vac. Sci. Technol. **6**, 795 (1969).
- [11] I. Blech, *EVAPORATED FILM PROFILES OVER STEPS IN SUBSTRATES*, Thin Solid Films **6**, 113 (1970).



- 
- [12] C. Wasik and J. Gniewek, *Calculation of Evaporated Film Thickness Distribution on Nonplanar Surfaces for Variable Angle Vapor Incidence*, J. Vac. Sci. Technol. **8**, 441 (1971).
- [13] U. Stroth, *Plasmaphysik: von den Grundlagen bis zur Fusion* (Vorlesungsskript, Stuttgart, 2009).
- [14] G. Franz, *Kalte Plasmen - Grundlagen, Erscheinungen, Anwendungen* (Springer-Verlag, Berlin, Heidelberg, New York, 1990).
- [15] M. Lieberman and A. Lichtenberg, *Principles of Plasma Discharges and Materials Processing* (John Wiley & Sons, Inc., New Jersey, 2005).
- [16] I. Langmuir, *OSCILLATIONS IN IONIZED GASES*, Proc. Nat. Acad. Sci. **14**, 627 (1928).
- [17] K. Riemann, *Analytical approximations for the sheath potential profile*, Plasma Sources Sci. Technol. **18**, 1 (2008).
- [18] L. Tonks and I. Langmuir, *A General Theory of the Plasma of an Arc*, Phys. Rev. **34**, 876 (1929).
- [19] D. Bohm, *The Characteristics of Electrical Discharges in Magnetic Fields* (McGraw-Hill, New York, 1949).
- [20] D. Bohm and E. Gross, *Theory of Plasma Oscillation*, Phys. Rev. **75**, 1851 (1949).
- [21] K. Riemann, *The Bohm criterion and sheath formation*, J. Phys. D: Appl. Phys. **24**, 493 (1991).
- [22] A. Metze, D. Ernie, and H. Oskam, *Application of the physics of plasma sheaths to the modeling of rf plasma reactors*, J. Appl. Phys. **60**, 3081 (1986).
- [23] R. Deutsch and E. Räuchle, *Hysteresis Effects in the Plasma-Electrode Boundary Sheath for Frequencies of the Order of the Ion Plasma Frequency*, Plasma Chemistry and Plasma Processing **11**, 501 (1991).
- [24] T. Mussenbrock and R. Brinkmann, *Nonlinear electron resonance heating in capacitive radio frequency discharges*, Appl. Phys. Lett. **88**, 151503 (2006).
- [25] O. Popov and V. Godyak, *Power dissipated in low-pressure radio-frequency discharge plasmas*, J. Appl. Phys. **57**, 53 (1985).
- [26] M. Lieberman, *Analytical Solution for Capacitive RF Sheath*, IEEE Trans. Plasma Sci. **16**, 638 (1988).

- [27] U. Czarnetzki, T. Mussenbrock, and R. Brinkmann, *Self-excitation of the plasma series resonance in radio-frequency discharges: An analytical description*, Physics of Plasma **13**, 123503 (2006).
- [28] M. Lieberman *et al.*, *The effects of nonlinear series resonance on Ohmic and stochastic heating in capacitive discharges*, Physics of Plasmas **15**, 063505 (2008).
- [29] M. Jin and K. Kao, *The effects of substrate bias on microwave plasma etching*, J. Vac. Sci. Technol. B **10**, 601 (1992).
- [30] Y. Raizer, M. Shneider, and N. Yatsenko, *Radio-Frequency Capacitive Discharges* (CRC Press, Boca Raton, London, New York, Washington D.C., 1995).
- [31] E. Häberle, *Skalierung turbulenter Strukturen im Torsatron TJ-K*, Diplomarbeit (Universität Stuttgart, Stuttgart, 2007).
- [32] H. Kim, J. Lee, and J. Shon, *Analytic model for a dual frequency capacitive discharge*, Physics of Plasma **10**, 4545 (2003).
- [33] J. Robiche, P. Boyle, M. Turner, and A. Ellingboe, *Analytical model of a dual frequency capacitive sheath*, J. Phys. D: Appl. Phys. **36**, 1810 (2003).
- [34] R. Seeböck, R. Deutsch, and E. Räuchle, *Electric current oscillations in a parallel-plate plasma reactor*, J. Vac. Sci. Technol. A **11**, 682 (1993).
- [35] K. Suzuki, K. Ninomiya, S. Nishimatsu, and S. Okudaira, *Radio-frequency biased microwave plasma etching technique: A method to increase SiO<sub>2</sub> etch rate*, J. Vac. Sci. Technol. B **3**, 1025 (1985).
- [36] A. Pointu, *A model of radio frequency planar discharges*, J. Appl. Phys. **60**, 4113 (1986).
- [37] F. F. Chen, *Introduction to Plasma Physics* (Plenum Press, New York, 1974).
- [38] R. Deutsch and J. Schwarz, *Dependence of the Self-bias on the Plasma Parameters and on the Electrode Areas in RF Plasma Reactors*, Plasma Chemistry and Plasma Processing **16**, 499 (1996).
- [39] M. Moisan and J. Pelletier, *Plasma Technology 4: Microwave Excited Plasmas* (Elsevier, Amsterdam, London, New York, Tokyo, 1992).
- [40] W. Petasch, E. Räuchle, H. Muegge, and K. Muegge, *Duo-Plasmaline - a linearly extended homogeneous low pressure plasma source*, Surf. Coat. Technol. **93**, 112 (1997).
- [41] C. Pai, *High quality voids free oxide deposition*, Mat. Chem. Phys. **44**, 1 (1996).

- [42] J. Schneider *et al.*, *Development of Plasma Polymerised SiO<sub>x</sub> Barriers on Polymer Films for Food Packaging Applications*, Plasma Process. Polym. **4**, S155 (2007).
- [43] M. Leins, *Erzeugung und Untersuchung plasmapolymersierter Barrierschichten*, Diplomarbeit (Universität Stuttgart, Stuttgart, 2005).
- [44] S. Plog, *Erzeugung und Untersuchung plasmapolymersierter Barrierschichten auf Polyethylenterephthalat*, Diplomarbeit (Universität Stuttgart, Stuttgart, 2010).
- [45] C. Bayer, E. Bapin, and R. von Rohr, *Overall kinetics of SiO<sub>x</sub> remote-PECVD using different organosilicon monomers*, Surf. Coat. Technol. **116-119**, 874 (1999).
- [46] A. Bieder, A. Gruniger, and R. Rudolf, von Rohr, *Deposition of SiO<sub>x</sub> diffusion barriers on flexible packaging materials by PECVD*, Surf. Coat. Technol. **200**, 928 (2005).
- [47] D. Huo, M. Yan, C. Chang, and P. Foo, *Planarization of SiO<sub>2</sub> films using reactive ion beam in plasma enhanced chemical vapor deposition*, J. Appl. Phys. **69**, 6637 (1991).
- [48] N. Selamoglu, A. Mucha, D. Ibbotson, and D. Flamm, *Silicon oxide deposition from tetraethoxysilane in a radio frequency downstream reactor: Mechanisms and step coverage*, J. Vac. Sci. Technol. B **7**, 1345 (1989).
- [49] C. Pai, J. Miner, and P. Foo, *Electron Cyclotron Resonance Microwave Discharge for Oxide Deposition Using Tetraethoxysilane*, J. Electrochem. Soc. **139**, 850 (1992).
- [50] A. Schulz, *Plasmapolymersierte Barrierschichten aus einer skalierbaren Mikrowellen-Plasmaquelle für flexible Solarzellenmodule*, Doktorarbeit (Universität Stuttgart, Stuttgart, 2005).
- [51] J. Kopecki, *Untersuchung zur plasmagestützten Abscheidung von Barrierschichten für flexible Dünnschichtsolarzellen*, Diplomarbeit (Universität Stuttgart, Stuttgart, 2008).
- [52] M. Walker *et al.*, *Investigations of plasma polymerized barrier films on polymeric materials*, Surf. Coat. Technol. **200**, 947 (2005).
- [53] E. Betran *et al.*, *Optical and electrical properties of a-Si<sub>x</sub>N<sub>y</sub>:H films prepared by rf plasma using N<sub>2</sub> + SiH<sub>4</sub> gas mixtures*, J. Non-Crystall. Sol. **137-138**, 895 (1991).

- [54] P. Bagnoli *et al.*, *Silicon nitride/semiconductor interface state density as a function of the insulator stoichiometry*, Appl. Surf. Sci. **56-58**, 881 (1992).
- [55] A. Schulz *et al.*, *Parameter Study by Infrared and Morphological Investigations of Plasma-Polymerised Thin Silicon Nitride Films Deposited with the Plasmodul*, Plasma Process. Polym. **4**, S826 (2007).
- [56] B. Rech *et al.*, *Amorphous and microcrystalline silicon solar cells prepared at high deposition rates using RF (13.56MHz) plasma excitation frequencies*, Solar Energy Materials and Solar Cells **66**, 267 (2001).
- [57] A. Matsuda, *Thin-Film Silicon - Growth Process and Solar Cell Application*, Japanese Journal of Applied Physics **43**, 7909 (2004).
- [58] G. Ganguly and A. Matsuda, *Defect formation during growth of hydrogenated amorphous silicon*, Phys. Rev. B **47**, 3661 (1993).
- [59] A. von Keudell and J. Abelson, *Direct insertion of SiH<sub>3</sub> radicals into strained Si-Si surface bonds during plasma deposition of hydrogenated amorphous silicon films*, Phys. Rev. B **59**, 5791 (1999).
- [60] J. Abelson, *Plasma Deposition of Hydrogenated Amorphous Silicon: Studies of the Growth Surface*, Appl. Phys. A **56**, 493 (1993).
- [61] J. Perrin and T. Broekhuizen, *Surface reaction and recombination of the SiH<sub>3</sub> radical on hydrogenated amorphous silicon*, Appl. Phys. Lett. **50**, 433 (1987).
- [62] MKS Instruments Inc., Reactive Plasma Generator, RPG-50, Product Manual .
- [63] L. Steiner, *Untersuchungen zur Abscheidung von Siliziumnitridschichten aus einem gepulsten mikrowellenerzeugten Plasma*, Diplomarbeit (Universität Stuttgart, Stuttgart, 2006).
- [64] E. Johnson and L. Malter, *Double-probe Method for Determination of Electron Temperatures in Steady and Time-Varying Gas Discharges*, Phys. Rev. **76**, 1411 (1949).
- [65] F. F. Chen, in *Plasma Diagnostic Techniques*, edited by R. H. Huddlestone and S. L. Leonard (Academic Press, New York, 1965), pp. 113-200.
- [66] *Datenblatt RPG-Stahl, Abnahmeprüfzeugnis 3.1*, Corus Hille Müller GmbH (2006).
- [67] R. Würz *et al.*, *Diffusions- und Isolationsbarrieren für flexible Cu(In,Ga)Se<sub>2</sub>-Dünnschichtsolarzellen auf unlegiertem Stahlsubstrat*, Conference Paper, Thüringer Grenz- und Oberflächentage (2008).

- [68] C. Pai and C.-P. Chang, *Downstream microwave plasma-enhanced chemical vapor deposition of oxide using tetraethoxysilane*, J. Appl. Phys. **68**, 793 (1990).
- [69] S. Brader and S. Quinlan, *PECVD Oxide Step-Coverage Considerations for Use as an Interlayer Dielectric in CMOS DLM Processing*, J. Electrochem. Sci. Technol. **135**, 2291 (1988).
- [70] J. Mercier, H. Naguib, V. Ho, and H. Nentwich, *Dry Etch-Back of Overthick PSG Films for Step-Coverage Improvement*, J. Electrochem. Soc. **132**, 1219 (1985).
- [71] J. Bierner and M. Jacob, *Characterization of step coverage change in ultraviolet-transparent plasma enhanced chemical vapor deposition silicon nitride films*, J. Vac. Sci. Technol. A **18**, 2843 (2000).
- [72] T. Kennedy, *Sputtered insulator film contouring over substrate topography*, J. Vac. Sci. Technol. **13**, 1135 (1976).
- [73] S. Ray, C. Maiti, S. Lahiri, and N. Chakrabarti, *TEOS-based PECVD of Silicon Dioxide for VLSI Applications*, Advanced Materials for Optics and Electronics **6**, 73 (1996).
- [74] K. Suzuki, K. Ninomiya, and S. Nishimatsu, *Microwave plasma etching*, Vacuum **34**, 953 (1984).
- [75] R. M. Levin and K. Evans-Lutterodt, *The step coverage of undoped and phosphorus-doped SiO<sub>2</sub> glass films*, J. Vac. Sci. Technol. B **1**, 54 (1983).
- [76] G. Schwartz and P. Johns, *Gap-Fill with PECVD SiO<sub>2</sub> Using Deposition/Sputter Etch Cycles*, J. Electrochem. Soc. **139**, 927 (1992).
- [77] S. Kühnemann, *private communications*, StEM - Stuttgart Center for Electron Microscopy, Max Planck Institute for Material Science .
- [78] E. Häberle *et al.*, *Control of layer growth by substrate bias*, Proc. of the 37th Europ. Conf. of Plasma Physics (2010).
- [79] E. Häberle, *Funktionsschichten für flexible, kostengünstige CIGS-Dünnschichtsolarzellen (Akronym: FlexNet)*, Öffentlicher Teil des Schlussberichts des Verbundvorhabens (2010).
- [80] T. Tisone and J. Bindell, *Step coverage in the vacuum deposition of thin metal films*, J. Vac. Sci. Technol. **11**, 72 (1974).
- [81] T. Tisone and J. Bindell, *Low-voltage triode sputtering with a confined plasma: Part I - geometric aspects of deposition*, J. Vac. Sci. Technol. **11**, 519 (1974).

- [82] J. Bindell and T. Tisone, *STEP COVERAGE FROM AN EXTENDED SPUTTERING SOURCE*, Thin Solid Films **23**, 31 (1974).
- [83] R. Ross and J. Vossen, *Plasma-deposited thin-film step coverage calculated by computer simulation*, Appl. Phys. Lett. **45**, 239 (1984).
- [84] J. Shaw and C. Tsai, *Monte Carlo simulations of plasma-deposited amorphous silicon*, J. Appl. Phys. **64**, 699 (1988).
- [85] W. Eckstein, *Computer Simulation of Ion-Solid Interactions* (Springer Verlag, Berlin, 1991).
- [86] W. Eckstein, R. Dohmen, A. Mutzke, and R. Scheinder, *SDTrimSP: A Monte-Carlo Code for Calculating Collision Phenomena in Randomized Targets*, IPP-Report **12/3**, (2007).
- [87] A. Mutzke, R. Schneider, and I. Bizyukov, *SDTrimSP-2D studies of the influence of mutual flux arrangement on erosion and deposition*, J. Nucl. Mat. **115**, 390 (2009).
- [88] J. Biersack and L. Haggmark, *A MONTE CARLO COMPUTER PROGRAM FOR THE TRANSPORT OF ENERGETIC IONS IN AMORPHOUS TARGETS*, Nucl. Instr. Meth. **174**, 257 (1980).
- [89] W. Möller and W. Eckstein, *TRIDYN - A TRIM SIMULATION CODE INCLUDING DYNAMIC COMPOSITION CHANGES*, Nucl. Instr. Meth. Phys. Res. B **2**, 814 (1984).
- [90] I. Bizyukov *et al.*, *Morphology and changes of elemental surface composition of tungsten bombarded with carbon ions*, Nuclear Instruments and Methods in Physics Research B **266**, 1979 (2008).
- [91] T. Shimoda *et al.*, *Solution-processed silicon films and transistors*, Nature **440**, 783 (2006).
- [92] S. Gates, C. Greenlief, and D. Beach, *Decomposition mechanisms of SiH<sub>4</sub> species on Si(100)-(2×1) for x=2,3, and 4*, J. Chem. Phys. **93**, 7493 (1990).
- [93] J. Zhou, Y. Chen, X. Liu, and S. Zou, *COMPUTER SIMULATION OF ION BEAM ENHANCED DEPOSITION OF SILICON NITRIDE FILMS*, Nucl. Instr. Meth. Phys. Res. B **39**, 182 (1989).
- [94] U. Fantz, *Spektroskopische Untersuchung und Modellierung von mikrowellenangeregten Silanplasmen*, Doktorarbeit (Universität Stuttgart, Stuttgart, 1995).



- [95] A. Matsuda and K. Tanaka, *Investigation of the growth kinetics of glow-discharge hydrogenated amorphous silicon using a radical separation technique*, J. Appl. Phys. **60**, 2351 (1986).
- [96] A. Matsuda *et al.*, *Temperature Dependence of the Sticking and Loss Probabilities of Silyl Radicals on Hydrogenated Amorphous Silicon*, Surface Science **227**, 50 (1990).
- [97] W. Bayer, *Diffusion and evolution of hydrogen in hydrogenated amorphous and microcrystalline silicon*, Solar Energy Materials & Solar Cells **78**, 235 (2003).
- [98] I. Bizyukov, A. Mutzke, R. Schneider, and J. Davis, *Evolution of the 2D surface structure of a silicon pitch grating under argon ion bombardment: Experiment and modeling*, Nuclear Instruments and Methods in Physics Research B **268**, 2631 (2010).
- [99] F. Rica Mendez, *Optische Eigenschaften von Siliziumnitridschichten*, Studienarbeit (Universität Stuttgart, Stuttgart, 2011).
- [100] E. Häberle *et al.*, *Deposition of Barrier Layers for Thin Film Solar Cells Assisted by Bipolar Substrate Biasing*, Plasma Processes and Polymers **6**, S282 (2009).
- [101] I. Pereyra and M. Alayo, *High quality low temperature PECVD silicon dioxide*, J. Non-Crystal. Sol. **212**, 225 (1997).
- [102] F. Meermann, *Charakterisierung von plasmapolymersierten  $\text{SiO}_x$ -Schichten aus den Arbeitsgasen Hexamethyldisiloxan und Sauerstoff*, Diplomarbeit (Universität Stuttgart, Stuttgart, 2004).
- [103] H. Siebert, *Anwendungen der Schwingungsspektroskopie in der anorganischen Chemie* (Springer Verlag, Heidelberg, 1966).
- [104] P. Pai, S. Chao, Y. Takagi, and G. Lucovsky, *Infrared spectroscopic study of  $\text{SiO}_x$  films produced by plasma enhanced chemical vapor deposition*, J. Vac. Sci. Technol. A **4**, 689 (1986).
- [105] H. Kim and J. Jang, *Infrared Spectroscopic Study of  $\text{SiO}_x$  Film Formation and Decomposition of Vinyl Silane Derivative by Heat Treatment. I. On KBr and Gold Surface*, J. Appl. Polym. Sci. **68**, 775 (1998).
- [106] P. J. Launer, *Infrared analysis of organosilicon compounds: spectra-structure correlations* (Laboratory for Materials, Inc., New York, 1987).
- [107] U. Mackens and U. Merkt, *Plasma-enhanced chemically vapour-deposited silicon dioxide for metal/oxide/semiconductor structures on InSb*, Thin Solid Films **97**, 53 (1982).



- [108] J. Theil, J. Brace, and R. Knoll, *Carbon content of silicon oxide films deposited by room temperature plasma enhanced chemical vapor deposition of hexamethyldisiloxane and oxygen*, J. Vac. Sci. Technol. A **12**, 1365 (1994).
- [109] C. Mortimer, *Chemie - Das Basiswissen der Chemie* (Thieme, Stuttgart, New York, 2001).
- [110] H. Rinnert, M. Vergnat, G. Marchal, and A. Burneau, *Strong visible photoluminescence in amorphous  $\text{SiO}_x$  and  $\text{SiO}_x\text{:H}$  thin films prepared by thermal evaporation of  $\text{SiO}$  powder*, Journal of Luminescence **80**, 445 (1999).
- [111] OPUS spectroscopy Software, Version 6, *Handbuch I, Applikations- und Messsoftware* (Bruker Optics, Ettlingen, 2006).
- [112] J. Moré, *The Levenberg-Marquardt algorithm: Implementation and theory*, Lecture Notes in Mathematics **630**, 105 (1978).
- [113] G. Lucovsky and D. Tsu, *Plasma enhanced chemical vapor deposition: Differences between direct and remote plasma excitation*, J. Vac. Sci. Technol. A **5**, 2231 (1987).
- [114] G. Lucovsky *et al.*, *Nitrogen-bonding environments in glow-discharge - deposited  $\alpha\text{-Si:H}$  films*, Phys. Rev. B **28**, 3234 (1983).
- [115] D. Tsu, G. Lucovsky, and M. Mantini, *Local atomic structure in thin films of silicon nitride and silicon diimide produced by remote plasma-enhanced chemical-vapor deposition*, Phys. Rev. B **33**, 7069 (1986).
- [116] G. Scardera, T. Puzzer, G. Conibeer, and M. Green, *Fourier transform infrared spectroscopy of annealed silicon-rich silicon nitride thin films*, J. Appl. Phys. **104**, 104310 (2008).
- [117] S. Hasegawa, L. He, Y. Amano, and T. Inokuma, *Analysis of  $\text{SiH}$  and  $\text{SiN}$  vibrational absorption in amorphous  $\text{SiN}_x\text{:H}$  films in terms of charge-transfer model*, Phys. Rev. B **48**, 5315 (1993).
- [118] B. Hanyaloglu and E. Aydil, *Low temperature plasma deposition of silicon nitride from silane and nitrogen plasmas*, J. Vac. Sci. Technol. A **16**, 2794 (1998).
- [119] M. Jurzecka *et al.*, *RF PE CVD deposition of amorphous  $\alpha\text{-Si}_x\text{N}_y\text{:H}$  layers for application in solar cells*, Vacuum **82**, 1128 (2008).
- [120] J. Schmidt and M. Kerr, *Highest-quality surface passivation of low-resistivity  $p$ -type silicon using stoichiometric PECVD silicon nitride*, Solar Energy Materials & Solar Cells **65**, 585 (2001).



# List of Figures

2.1	Plasma sheath . . . . .	10
2.2	Equivalent circuit of capacitive discharges . . . . .	14
2.3	Homogeneous and inhomogeneous model of a capacitive discharge . . . . .	15
2.4	Schematic asymmetric capacitive discharge . . . . .	20
2.5	Generation of a dc self bias . . . . .	21
2.6	Dependence of the dc self bias voltage $U_{\text{bias}}$ on the electrode-area ratio $\eta$ in the case of a symmetric rectangular driving voltage. . . . .	25
2.7	Time dependence of current and ion energy at biased electrode in the case of various bias frequencies . . . . .	29
3.1	Layer growth process in a $\text{SiH}_4$ plasma . . . . .	36
3.2	Scheme of Plasmodul . . . . .	38
3.3	Picture of Plasmodul . . . . .	39
3.4	Pathway of in-situ FTIR diagnostic . . . . .	40
3.5	Duo-Plasmaline . . . . .	41
3.6	Ideal asymmetric bipolar rectangular pulse . . . . .	42
3.7	View on substrate holder . . . . .	43
3.8	Current-voltage characteristics of the bias . . . . .	44
3.9	Schematic of FTIR measurement . . . . .	46
3.10	Determination of the refractive index . . . . .	48
3.11	Schematic double probe . . . . .	49
3.12	Attached double probe on the Plasmodul . . . . .	50
3.13	I-U characteristics of Langmuir double probe . . . . .	52
3.14	Electron-density measurements in the Plasmodul . . . . .	53
3.15	Electron-temperature measurements in the Plasmodul . . . . .	54
4.1	Layer growth on substrates with rough surfaces . . . . .	58
4.2	Model substrate . . . . .	59
4.3	Layer growth model . . . . .	60
4.4	Definition of $\Delta$ and $\Phi$ . . . . .	62

4.6	Dependence of self bias on pulse width . . . . .	62
4.5	Trench coating in dependence of the particular bias parameters . . . . .	63
4.7	Breaking edge of SiO <sub>x</sub> layers deposited on model substrates . . . . .	65
4.8	Breaking edge of SiN <sub>y</sub> layers deposited on model substrates . . . . .	67
4.9	Surface of SiO <sub>x</sub> layers deposited on steel substrates with various surface roughness . . . . .	68
4.10	Resistance of biased and unbiased SiO <sub>x</sub> coatings . . . . .	69
4.11	Breakdown voltage of biased and unbiased SiO <sub>x</sub> coatings . . . . .	70
4.12	Resistance of biased and unbiased SiN <sub>y</sub> coatings . . . . .	71
4.13	Breakdown voltage of biased and unbiased SiN <sub>y</sub> coatings . . . . .	72
5.1	One-dimensional target configuration . . . . .	75
5.2	Two-dimensional target configuration . . . . .	77
5.3	Bias voltage characteristics in SiH <sub>4</sub> plasma . . . . .	79
5.4	Simulated and experimental layer growth without substrate bias . . . . .	81
5.5	Simulated and experimental layer growth with substrate bias . . . . .	82
5.6	Illustration of depiction of local layer-forming mechanisms . . . . .	84
5.7	Comparison of ion and radical induced layer-forming mechanisms . . . . .	85
5.8	Local layer-forming mechanisms induced only by ion bombardment . . . . .	86
6.1	FTIR spectra SiO <sub>x</sub> . . . . .	91
6.2	Influence of molecular structure on Si-O-Si stretching mode . . . . .	94
6.3	Overview of simulated SiO <sub>x</sub> spectra . . . . .	95
6.4	Oxygen and hydrogen content in SiO <sub>x</sub> coatings . . . . .	96
6.5	Influence of substrate temperature on IR spectra . . . . .	97
6.6	FTIR spectra SiN <sub>y</sub> . . . . .	99
6.7	Influence of molecular structure on Si-N stretching mode . . . . .	101
6.8	Overview of simulated SiN <sub>y</sub> spectra . . . . .	102
6.9	Nitrogen and hydrogen content in SiN <sub>y</sub> coatings . . . . .	103
6.10	Refractive index SiO <sub>x</sub> . . . . .	104
6.11	Refractive index SiN <sub>y</sub> . . . . .	105

# List of Tables

3.1	Plasmodul discharge parameters . . . . .	40
3.2	Plasma parameters in Plasmodul . . . . .	41
3.3	Overview of electron densities in the Plasmodul . . . . .	52
3.4	Overview of electron temperatures in the Plasmodul . . . . .	54
5.1	Simulation input parameters . . . . .	78
6.1	Overview of vibration modes for SiO <sub>x</sub> layers . . . . .	92
6.2	Overview of vibration modes of SiN <sub>y</sub> layers . . . . .	100



# Acknowledgment

First of all, I would like to thank my supervisor Prof. Dr. Ulrich Stroth for his support during all the time I spent at the Institut für Plasmaforschung and for giving me the possibility of preparing this thesis at his institute. With his support, he played a big role for the success of this work. Besides this, I thank Prof. Dr. Tilman Pfau for taking over the cosupport of this work and Prof. Dr. Günter Wunner for chairing the examination committee.

For the admittance and the possibility of preparing this work in his working group, I thank Dr. Matthias Walker. With him and Dr. Andreas Schulz I had fruitful discussions during my time in the technology working group. At this point, I single out Dr. Martina Leins, Jochen Kopecki, Joachim Schneider and Ulrich Schweitzer from all my colleagues, which always gave valuable support. Working with them was pleasant all the time. I thank them for all conversations, which were not only restricted to technical subjects. As well, I thank Heinz Petto. I could count on his technical support all the time. In general, the atmosphere among all Ph.D. and diploma students at the institute was amicable. I thank all of them for the assistance and the fun during the past four years.

An important part of my work was the simulations done with the simulation code SDTrimSP-2D. These simulations were carried out in cooperation with the university of Greifswald and the IPP Greifswald, especially with Prof. Dr. Ralf Schneider and Dr. Andreas Mutzke. I express my great gratitude to them for the intensive and especially the delightful teamwork. For me, the work on the simulations was a very interesting aspect during the past four years.

Dr. Roland Würz and Dr. Viola Küstner provided me with useful information and discussions during my work for the BMBF project FlexNet. For the intensive and pleasant collaboration I thank them very much.

My maximum gratitude goes to my husband Dr. Mirko Ramisch, who always gave me technical as well as, above all, moral support. His understanding was a great foothold all the time. As well, I thank him for proofreading this thesis. Last but not least, my great thanks goes to my parents Elisabeth and Günter Häberle, who always give great support in all my decisions.





# Curriculum Vitae

## Personal Data

Name	Evelyn Christine Ramisch, née Häberle
Date and place of birth	18th of January, 1982 in Stuttgart
Family status	Married
Nationality	German

## School Education

1988–1992	Elementary school: Hermann-Butzer Schule, Schwieberdingen
1992–2001	Secondary school: Gymnasium Korntal-Münchingen, Korntal-Münchingen
June 2001	Final exam (Abitur) with main courses mathematics and physics

## Scientific Education

Oct 2001–Mar 2007	Study of physics at the Universität Stuttgart, Stuttgart
Mar 2006–Mar 2007	Preparation of the diploma thesis entitled “Skalierung turbulenter Strukturen im Torsatron TJ-K” in the group of Prof. Dr. U. Stroth at the Institut für Plasmaforschung, Universität Stuttgart
Mar 2007	Diploma in physics
May 2007–May 2011	Ph. D. graduation with subject “Influence of the Ion Energy on Generation and Properties of Thin Barrier Layers Deposited in a Microwave Plasma Process” in the group of Dr. M. Walker at the Institut für Plasmaforschung, Universität Stuttgart
since Jun 2011	employed at Robert Bosch GmbH as development engineer